ELECTROSPRAY MICROPROPULSION FOR SMALL SPACECRAFT: MICROMILLED POROUS EMITTER STUDIES

MICROPROPULSION DES VÉHICULES SPATIAUX DE PETITE TAILLE PAR ÉLECTROPULVÉRISATION: ÉTUDE DES ÉMETTEURS POREUX MICRO-FRAISÉ

A Thesis Submitted to the Division of Graduate Studies
of the Royal Military College of Canada
by

Griffin Jones, BEng

In Partial Fulfillment of the Requirements for the Degree of
Master of Applied Science in Aeronautical Engineering
Department of Mechanical and Aerospace Engineering

November 10, 2023

This page intentionally left blank.

Electrospray Micropropulsion for Small Spacecraft: Micromilled Porous Emitter Studies

Micropropulsion des véhicules spatiaux de petite taille
par électropulvérisation: étude des émetteurs poreux micro-fraisé

Candidate / Candidat

Griffin Jones
Royal Military College of Canada
Mechanical and Aerospace Engineering

MASc Candidate in Aeronautical Engineering/
Candidat à la maîtrise en génie aéronautique

Examination Committee / Comité examinateur

Dr. Pat Heffernan *Royal Military College of Canada*	Chair / Président
Dr. Glenn Harvel *Ontario Tech University* *Engineering and Applied Science*	External / Externe
Dr. Francis Okou *Royal Military College of Canada* *Electrical and Computer Engineering*	Internal-External / Interne-Externe
Dr. Viet-Hung Vu *Royal Military College of Canada* *Mechanical and Aerospace Engineering*	Internal / Interne
Dr. Manish Jugroot *Royal Military College of Canada* *Mechanical and Aerospace Engineering*	Supervisor / Superviseur

Abstract

Electrospray propulsion (ESP) is emerging as a promising variant of electric spacecraft micropropulsion noted for its high thrust precision, excellent efficiency, inherent scalability and ample opportunity for system simplification. Moreover, the porous emitter subgroup within ESP leverages passive capillary flow to not only enhance efficiency but further simplify and scale down the overall system. In the current stage of research, ESP faces challenges related to complex development, short operational lifespans, and low throttleability. Conventional machining of porous emitters have demonstrated potential in enabling rapid prototyping and increased access to research, though micro-machining strategies to produce samples optimized for ESP experimentation are often omitted.

This thesis seeks to explore thrust range limitations, as well as to contribute to literature concerning the micromilling of porous glass emitters intended for use in ESP. A crescent wedge emitter design is proposed enabling two distinct operational thrust modes at separate high voltage set points. The crescent emitter is micro-milled out of porous glass, and the machining strategies used to fabricate samples with ideal qualities are detailed. To validate the micromilling process and assess variable thrust operation, a simplified linear wedge design establishes a baseline throttle range for comparison. The design process for each was aided by electrostatic and charged particle tracing modelling to minimize required operational voltages and predict thruster performance. Both emitter designs undergo testing in high vacuum with a specific focus on characterizing the emitted current with applied voltage. Ultimately, the crescent wedge design displayed a stepped emission behaviour not observed in the linear wedge that can be attributed to a primary, low-thrust mode of operation at low voltage that transitions into a secondary, higher thrust range at higher voltages.

Résumé

La propulsion par électropulverisation (ESP) apparaît comme une variante prometteuse du micro-engin spatial électrique. Propulsion connue pour sa grande précision de poussée, son efficacité et son évolutivité inhérente. De plus, le sous-groupe d'émetteurs poreux au sein de l'ESP exploite le flux de propulseur liquide capillaire passif, non seulement pour améliorer l'efficacité, mais potentiellement permettrait de réduire l'ensemble du système. Au stade actuel de la recherche, l'ESP est confronté à des défis liés à un développement complexe, à des durées de vie opérationnelles courtes et à une faible accélération. L'usinage conventionnel d'émetteurs poreux a démontré son potentiel en permettant un prototypage rapide et un accès accru à la recherche.

Cette thèse cherche à explorer les limites de la plage de poussée, ainsi qu'à contribuer au pont de connaissances concernant le microfraisage des émetteurs en verre poreux. Une conception d'émetteur en forme de croissant est proposé d'activer deux modes de poussée opérationnels distincts à des points de consigne haute tension distincts. Pour valider le processus de microfraisage et évaluer le fonctionnement à poussée variable, une conception de coin linéaire simplifiée aux des fins de comparaison. Le processus de conception de chacun a été facilité par une modélisation de particules électrostatiques et chargées afin de minimiser les tensions de fonctionnement requises et de prédire les performances du propulseur. Les deux modèles d'émetteur sont soumis à des tests sous vide avec un accent particulier sur la caractérisation du courant émis avec la tension appliquée. La conception en croissant a demontré un comportement d'émission échelonné non observé dans le coin linéaire qui peut être attribué à un mode de fonctionnement primaire (à faible poussée à basse tension) qui passe ensuite à une plage de poussée secondaire (plus élevée à des tensions plus élevées).

Acknowledgements

I would like to thank my supervisor, Dr. Manish Jugroot, for giving an environmental engineer the chance to leap to a new discipline and follow their passion. Your advice on navigating academia and noticing the utility in every idea has been extremely helpful.

There are a number of people who have provided excellent technical assistance and advice for which the following research has been enriched ten times over as a result. The mechanical engineering technicians, specifically Charles and Brendan, provided necessary assistance in the early thruster fabrication and their advice on all things machining related was greatly appreciated. The electrical engineering technicians, specifically Tristan, Germain and Dave, for their patience and advice to a first-time electronics student, who was thrilled to have the chance to develop their own hardware. In addition, I would like to thank the Queen's Space Engineering Team, specifically Jacob and Sean, for allowing me to be a part of the battery board design subteam and further develop the electronics prototyping confidence I needed to apply to my own research. Thank you to Dr. Snelgrove for allowing the use of the scanning electron microscope for this research. Thank you to the examiners, for taking their time to vet this thesis, and allow me to prove myself.

The support of the Natural Sciences and Engineering Research Council of Canada, the Director General Air and Space Force Development, and the Department of Mechanical and Aerospace Engineering Post-Graduate scholarship are gratefully acknowledged.

I would like to thank the friends and colleagues I have met during my time at RMC. Insightful discussions about respective research at school were always a good distraction and sometimes even fruitful when given a chance to view the problem from an outside perspective. More importantly, our discussions about things other than research over live music & drinks, golf, and hockey helped keep me sane.

Thank you to my family, for forcing me to get out of Kingston on the holidays and live in the present with them. Finally, thank you to my partner Lorena, for pushing me to try out something different in the first place. I have expanded the horizons of what I can learn and accomplish beyond anything that I would have initially thought possible, and am eternally grateful for your support throughout this degree.

Contents

List of Tables

List of Figures

Nomenclature

β	Field enhancement factor
ΔP	Pressure gradient
Δv	Change in velocity
ϵ_0	Vacuum permittivity constant
ϵ_r	Relative permittivity
η	Propulsion efficiency
η_{tr}	Transmission efficiency
γ	Surface tension
$\mathbf{v}$	Velocity
μ	Fluid viscosity
ϕ_p	Porosity
ρ	Mass density
ρ_s	Space charge density
τ_μ	Viscous stress
τ_g	Inertial stress
τ_L	Surface tension stress
τ_n	Normal electric stress
τ_t	Tangential electric stress
θ_w	Wedge angle
$\vec{u}$	Fluid velocity
a	Acceleration
A_n	Nozzle area
Bo_e	Electric bond number
C_E	Electric field shape factor
D_{eff}	Effective pore diameter
e	Elementary charge
E_0	Electric field strength at emission onset
E_n	Normal electric field strength
F_c	Cutting force
F_e	Electric field force
F_i	Coulomb force
f_i	Fraction of the i^{th} species
F_p	Ploughing force
g_0	Gravitational acceleration constant
h	Uncut chip thickness
h_{min}	Minimum uncut chip thickness
I_b	Beam current
I_{shunt}	Shunt emitter current
I_{sp}	Specific impulse
K	Conductivity
k	Porous permeability
L	Wedge length
m_f	Spacecraft dry mass
m_i	Mass of the i^{th} species
m_o	Spacecraft wet mass
m_p	Propellant mass
m_{sc}	Spacecraft mass
n	Charge multiplication factor
n_i	Number of ions
p_a	Atmospheric pressure
P_B	Static Laplace pressure
P_c	Capillary pressure
p_n	Nozzle pressure
Q	Flow rate
q_i	Charge of the i^{th} species
Q_{min}	Minimum flow rate
r	Particle position
R^*	Characteristic radius of curvature
R_1	Wedge height
R_2	Wedge radius of curvature

r_β	Cutting edge radius of tool
Re	Reynolds number
T	Thrust
u	Nondimensionalized applied voltage
V	Voltage
V_0	Voltage at emission onset
V_a	Plume potential
v_e	Exhaust velocity
v_i, j	Particle velocity
V_m	Mesh element volume
Z	Hydraulic impedance

Acronyms

ADCS Attitude control and determination system
AFET Air force electrospray thruster
BSG Borosilicate glass
CAM Computer aided manufacturing
CDAQ Control and data acquisition
CNC Computer numerical control
COTS Commercial-off-the-shelf
DOC Depth of cut
DRIE Deep reactive ion etching
EHD Electrohydrodynamics
EP Electric propulsion
ESP Electrospray propulsion
FEEP Field emission electric propulsion
HV High voltage
IL Ionic liquid
LEO Low earth orbit
LISA Laser Interferometer Space Antenna
MEMS Micro-electromechanical systems
PCB Printed circuit board
PEEK Polyether ether ketone
PET Porous electrospray thruster
PIR Pure ionic regime
RAPPEL Royal Military College Advanced Propulsion and Plasma Exploration Laboratory
ROC Radius of curvature
S-iEPS Scalable ion-electrospray propulsion system
SEM Scanning electron microscope
SSE Secondary species emission
TOF Time-of-flight
TVC Thrust vector control

1 Introduction on Space Missions for Small Spacecraft

The advent of the nanosatellite, falling within the weight class of 1.1 to 10 kg, and more specifically, the standardized CubeSat spacecraft platform, has significantly lowered the barrier to global space access. The compact 10 x 10 x 10 cm unit CubeSat format, facilitated by advancements in microelectronics, has substantially reduced both development and launch costs. For reference, a three-unit CubeSat is shown in Figure 1.1. This not only allows a wider range of missions to be performed by smaller academic institutions and private entities, but also by emerging nations. Investment into intellectual capital can be justified with the benefit of scientific training, as well as business and technological development, which in turn is promotes long-term economic prosperity [1]. Missions of interest for such nations include environmental and agricultural monitoring, disaster response, and telecommunications. Moreover, established organizations such as the Canadian Space Agency employ CubeSat programs as educational outreach tools to great effect in inspiring the STEM workforce of tomorrow.

Spacecraft propulsion systems seek to increase the mission design space by allowing for longer duration, higher functionality missions. However, propulsion technology development has had trouble keeping up with the same pace of innovation. This research explores a specific form of electric micro-propulsion termed electrospray propulsion (ESP), whose small form-factor and high efficiency seeks to fulfill the nanosatellite class's growing needs. In this chapter, an introduction to small satellites and their associated challenges with propulsion are provided alongside a simplified treatment of spacecraft propulsion fundamentals. Additionally, ESP and its enabling capabilities are introduced, to be covered in-depth in the following chapter.

1.1 NanoSat Revolution

The new space age is gaining momentum. In 2018, the Federal Aviation Administration estimated that the global commercial satellite industry is worth $260.5B with expected revenues of $1.1T by 2040 [2]. Historically, the launch of full-scale satellite platforms necessitated tens to hundreds of millions of dollars. Year over year, launch costs have been decreasing at a rapid pace, where the cost per kilogram to launch was as low as $1,500 in 2020 [3]. Not only are launch costs are diminishing, but small satellites are frequently securing orbital insertion as secondary payloads, replacing ballasts and adding value for launch providers, as illustrated in Figure 1.2.

Comparatively, CubeSats are a more cost-effective alternative at approximately $200k to $2M each. The total cost per kilogram, including development, integration and launch, is half as much as larger payloads [1]. As Commercial-off-the-shelf (COTS) technology is proving to be increasingly capable of replacing specialized high cost components, a development environment is fostered where satellites are easily reprogrammed and reconfigured for a diverse set of missions.

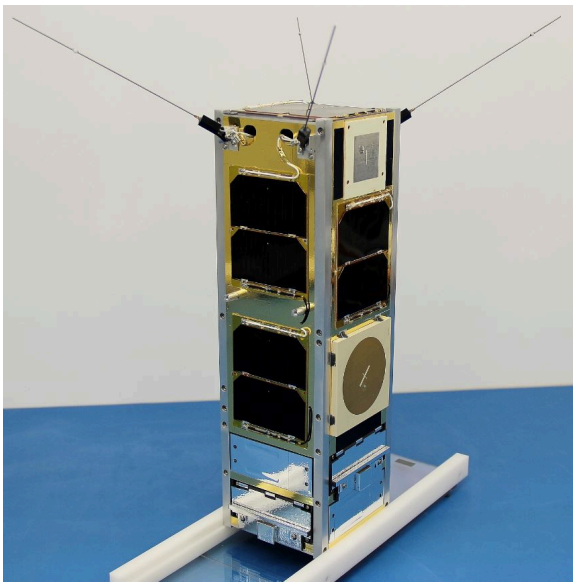

Figure 1.1: The CanX-7 CubeSat developed by Space Flight Laboratory (SFL) with collaboration from the Royal Military College of Canada. The photo, sourced from SFL [4], shows the 10 x 10 x 34 cm, 3.4 kg spacecraft.

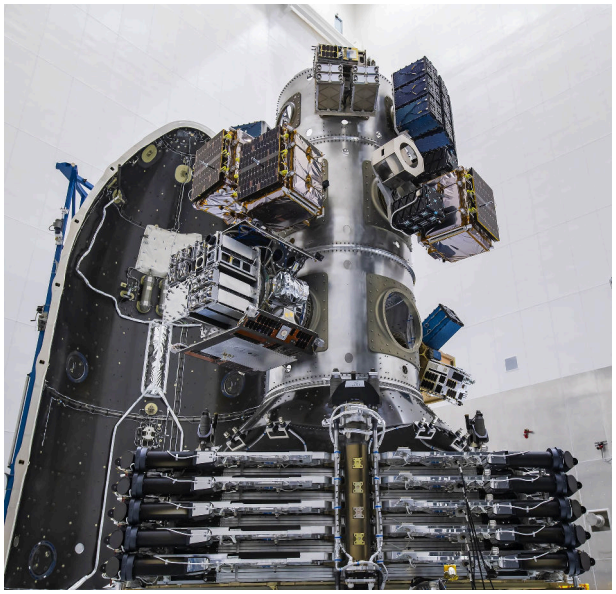

Figure 1.2: CubeSats mounted atop a Falcon 9 fairing as part of Transporter-1 in 2021, SpaceX's first dedicated SmallSat Rideshare Program mission. Starlink modules are stacked below, resulting in a record-breaking 143 spacecraft in a single launch. Photo sourced from [5].

Not only are development costs reduced, but development timelines are accelerated. Given that large satellite projects with extended development periods may launch with decade-old technology, a relatively shorter 1-3 year nanosatellite development cycle can become a crucial advantage.

According to United Launch Alliance, there were approximately 20,000 objects in orbit as of 2019 [6]. While it took seventy years to reach this milestone, this number has more than doubled in just the following two years. CubeSat launches in particular have experienced exponential growth, constituting approximately half (∼1000) of all orbital deployments occurring since 2017 [7]. Despite significant advancement in CubeSat technologies having become smaller and more efficient over the last two decades, associated propulsion systems have fallen behind. In fact, 93% of all CubeSats that have deployed to orbit do not have propulsion systems included [8] as indicated in Figure 1.3. Existing flight qualified propulsion technology requires increased size, weight, power and cost that exceed available allowances stipulated during the design phase. Additionally, in pursuit of miniaturization, many of the physical phenomena associated with different forms of propulsion do not scale down effectively and nonlinear increases in efficiencies are observed [9].

Reinforcing this trend, COTS subsystems and components have limited lifetimes, especially if not space-rated, and therefore long-term mission enabling propulsion systems may be deemed as not necessary for mission success resulting in relaxed size, weight, power, and cost constraints. Additionally, range safety must also be considered when planning to launch a nanosatellite as a secondary payload. This refers to limitations on the allowance of pressurized or energetic propellants on secondary payloads in order to protect the primary payload [10]. As a result, passive spacecraft are often confined to low, pre-selected orbits and cannot avoid collisions. It is worth noting that passive systems that aid deorbiting capabilities have been successfully demonstrated such as solar sails [11]. However, orbital altitude and thus satellite lifetime constraints must be

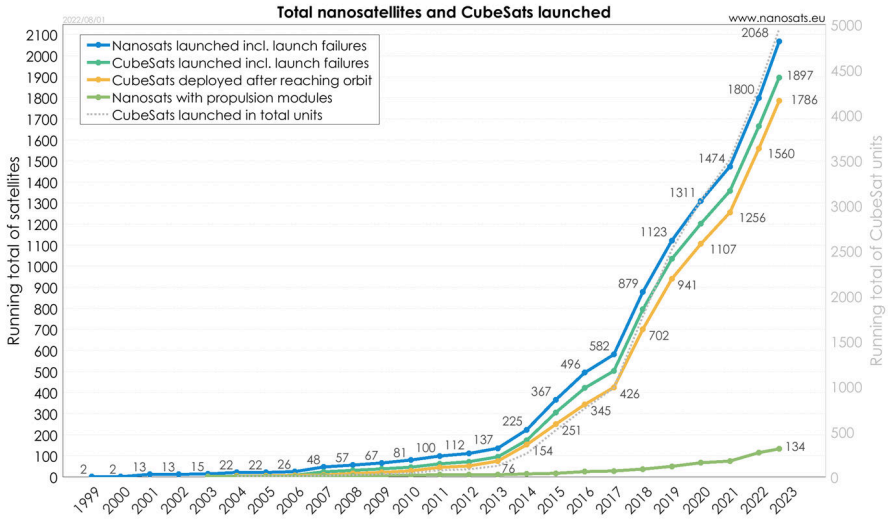

Figure 1.3: Cumulative sum of launched nanosatellites and CubeSats since their inception in 1999. Figure sourced from `nanosats.eu` [8].

more flexible in order to comply with growing governmental regulations related to the mitigation of space debris. For example, in addition to limiting satellite lifetimes to 5 years on-orbit, the Federal Communications Commission recently proposed an orbital debris mitigation strategy wherein all satellites operating above a set altitude would be required to be equipped with the ability to perform collision avoidance manoeuvres [12].

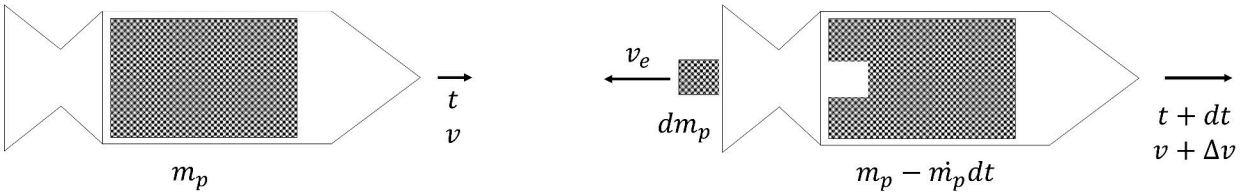

Figure 1.4: Simplified schematic of spacecraft propulsion.

1.2 Spacecraft Propulsion Fundamentals

A simple analysis of spacecraft flight dynamics begins with Newton's second law of motion. The force, measured in Newtons, is the change of velocity, $\mathbf{v}$, over time multiplied by the spacecraft mass, m_{sc}. This can be rewritten as visualized in Figure 1.4, as thrust produced through the exhaust of propellant at high speeds, v_e, in the direction opposite of intended motion:

$$T = \frac{d\mathbf{v}}{dt}(m_{sc}) = v_e \dot{m}_p \tag{1.1}$$

where $\dot{m}_p$ is the mass flow rate of the propellant. From this equation, the ideal rocket equation for spacecraft can be derived:

$$\Delta v = v_e \ln \frac{m_o}{m_f} \tag{1.2}$$

assuming exhaust velocity is constant, and m_o and m_f is the spacecraft initial and final mass respectively, where the total propellant mass, m_p, is the difference between m_o and m_f. Note that Δv is a scalar that shares units with speed, though in this context, it is a measure of the impulse per unit mass required to perform manoeuvres, not a measure of the actual change in velocity of the spacecraft itself, as will be described further in Section 1.4.

For mission planning purposes, Equation 1.2 is often presented in the form:

$$m_o = m_f \exp\left[\frac{\Delta v}{v_e}\right] \tag{1.3}$$

to determine the propellant mass required for a given Δv. This is a common first order analysis undertaken during preliminary spacecraft mission planning. Mission limitations can be determined such as maximum spacecraft weight and size which can be further analyzed through propulsion system selection tradeoffs. It is worth noting that mass ratio in itself is another important spacecraft performance parameter, given how costly it is to launch spacecraft on a per kilogram basis. For example, a geostationary satellite with a mission lifetime of 15 or more years will require large Δv on the order of 7 km/s to raise itself to its final orbital height, and perform stationkeeping manoeuvres to mitigate orbital perturbations from the moon and sun [13]. Given characteristics of previous flight qualified propulsion systems, this may result in propellant taking up to 90% of the spacecraft mass at launch.

The specific impulse of a propulsion system holds equal design significance with thrust, and are frequently discussed together by academics and commercial entities alike. Quantified in seconds, specific impulse represents the impulse delivered per unit weight of propellant. In simpler terms, it is the ratio of effective exhaust speed to gravitational acceleration:

$$I_{sp} = \frac{v_e}{g} = \frac{T}{\dot{m} g_0} \tag{1.4}$$

where g_0 is the gravitational acceleration constant. Together, thrust and specific impulse can be used to describe total required propulsive power, P:

$$P = \frac{T I_{sp} g_0}{2\eta} \tag{1.5}$$

where η is the efficiency of the given propulsion system. As will be discussed, the current state of the art spacecraft propulsion systems cover a wide range of thrust and specific impulse ranges that trade efficiency for thrust depending on mission requirements.

1.3 Micro-propulsion Methods

Mature spacecraft propulsion systems can be broadly classified into electric and chemical systems. A chemical propulsion system utilizes high pressure combustion by inducing a chemical reaction between a fuel and an oxidizer to expand the resultant gas through a nozzle and achieve acceleration. Such systems come in the form of cold gas, liquid mono- or bi-propellant, solid, or hybrid systems. They have a specific impulse ceiling of approximately 400 seconds, but are mature and offer high thrust on demand [14]. Considering Equation 1.5, chemical systems are often described as 'energy-limited' systems as the energy required to propel the spacecraft is stored within the propellant's chemical bonds. A fixed amount of energy per unit mass enforces an effective ceiling on the total achievable exhaust velocities and thus specific impulse. These velocities are typically ten times smaller than those observed in electric propulsion, thereby requiring an increased propellant mass fraction for the same Δv, as described by Equation 1.3.

Electric propulsion (EP) may be generally divided into three categories by the methods in which propellant is ionized and accelerated [15]. An electrothermal device will use heating elements to ionize and expand propellant through a nozzle much like its chemical counterparts. Thrusters such as resistojets offer relatively higher thrust at lower efficiencies compared to their other electric counterparts. An electrostatic system utilizes a set of gridded electrodes biased to a high electric potential in order to accelerate an ionized gas, also called a plasma, to extremely high exhaust speeds. Thrusters such as the gridded ion engine and hall-effect thruster are sufficiently mature and offer a decent mid-level thrust and efficiency range. Finally, an electromagnetic system takes advantage of the Lorentz force generated through the interactions of electric currents driven through the plasma body with surrounding magnetic fields. A pulsed plasma thruster offers extreme efficiency at low thrust. While higher thrust regimes are theorized for this method, they are severely limited by the supplied power.

For EP, the energy source is entirely separated from the propulsive components and thus has increased potential for efficiency. However, current miniature electric energy source technology is still at an early stage, and the rate at which power can be supplied is restricted by factors such as the system weight (e.g. heavy battery arrays) and technical complexity (e.g. nuclear-thermal propulsion). These constraints, in turn, severely limit the immediately available thrust for high impulse manoeuvres.

In summary, low efficiency, high thrust chemical systems are commonly relied upon for missions where orders of magnitude more thrust are required for time-critical manoeuvrability. High efficiency, low thrust electric systems that can generate significantly larger Δv over longer periods of time are considered for long duration missions such orbital maintenance or interplanetary travel.

1.3.1 Electrospray Propulsion

Electrospray as a form of electrostatic propulsion is a highly efficient and precise thrust system for use on small spacecraft. When an electrically conductive liquid is sufficiently electrostatically stressed, the meniscus deforms into a cone shape that further increases the local electric field strength. At this point, depending on the characteristics of the propellant under stress, ions may be released through field evaporation, or a jet may form as shown in Figure 1.5, releasing a stream of charged droplets which are subsequently accelerated in the electric field towards a biased gridded electrode. A simplified schematic of typical electrospray operation is depicted in Figure 1.5. Due to highly unpredictable electrohydrodynamic instabilities, ESP is hindered primarily by accumulating propellant overspray which leads to performance losses and shortened device lifespans. Additionally, such instabilities hinder the adjustable on-orbit thrust range, thus severely limiting mission flexibility. Consequently, a significant portion of research is dedicated to increasing thruster capability and lifetime, aiming to achieve operational characteristics suitable for multi-year missions.

ESP can generate thrust without the ignition of a plasma discharge. As the electric field strength is inversely proportional to the distance between electrodes, these systems benefit from miniaturization that would otherwise severely limit efficiency in their discharge-based counterparts. Although only achieving nN-level thrusts individually, ESP emission points can be readily configured in an arrayed format, enhancing potential thrust density while accommodating volume constraints. Scaling may also be performed at a system level, whereby sub-modules of arrayed ESP may be organized in parallel.

Ionic liquids (IL) are among the typical propellants employed, whose beneficial characteristics include high conductivity, negligible vapour pressure, low surface tension, thermal stability, and flexible cation-anion pairing [17]. A propellant composed completely of ion pairs allows for the

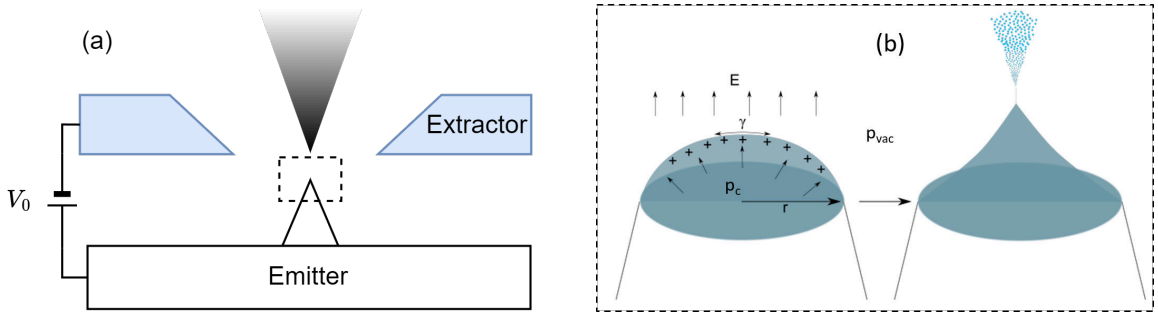

Figure 1.5: Schematic of (a) typical electrospray operation involving a conductive propellant and biased extractor and emitter electrodes, and (b) micro-metric Taylor cone evolution (sourced from [16]).

emission of separate positive and negative ion beams. Thus, a self-neutralizing bipolar operating mode may be achieved, where power-hungry and complex hollow cathode neutralizers normally present in other forms of propulsion can be eliminated. Near-zero vapour pressure benefits the porous emitter variety of ESP, where passive propellant delivery has the potential to replace traditional propellant delivery through pumps, tanks and valves, further reducing size, weight, power, and cost constraints. ESP offers specific impulses from 1000 to 4500 seconds [18], allowing for a reduced propellant to satellite mass fraction and therefore increased achievable Δv according to Equations 1.2 and 1.4.

Of note are the closely related field emission electric propulsion (FEEP) group of thrusters that operate using the same concept of electrospray, though ion extraction is accomplished primarily through field emission, as opposed to high flow, solvated droplet emission. While the title is often reserved for thrusters that use liquid metal propellant (e.g. Cesium, gallium, indium, etc.) such as Enpulsion's NANO and MICRO series of thrusters [19], the field emission phenomena has also been observed in classes of low flow electrospray which have been described as operating in the pure ionic regime (PIR). In the current state of the art, FEEP is often more stable and offers considerably improved metrics with commonly achieved specific impulses of 4000 to 10,000 seconds and generation of tens of μN of thrust for a single emitter, an order of magnitude more than what has been shown for single-emitter ESP [20]. However, FEEP requires much larger power draw due to the necessity of a neutralizer and propellant heating. Larger extraction voltages also drive power draw due to increased ionization energies required for liquid metal ion field evaporation. To that effect, specific power is generally higher for FEEP than for ESP, at ~60 W/mN and ~10 W/mN respectively [13].

1.4 Missions Enabled by Electric Propulsion

With the addition of high efficiency, low thrust technologies to nanosatellites, many beneficial manoeuvres become available to operators which effectively extend mission lifetime and capabilities. See Table 1.1 for a summary of typical missions for which propulsion would be utilized described by their respective Δv requirements. In low earth orbit (LEO), spacecraft experience orbital decay primarily caused by atmospheric drag. At higher altitudes, orbital spacecraft experience smaller but non-negligible perturbations caused by factors such as sun and moon to earth gravity gradients and solar radiation pressure that push the spacecraft out of its intended operational orbit. Spacecraft station-keeping mitigates these concerns through multiple small thruster burns, the duration of which are highly dependent on altitude, cross-sectional area, and mass. This aspect is crucial for

missions such as formation flight in a constellation and earth observation missions, where ensuring precise relative positioning of spacecraft and maintaining an accurate and repetitive ground-track are constant priorities. While highly variable, the Δv requirements for stationkeeping can generally be expected to fall within 10s to 100s of m/s annually [21].

Mission	Δv **[m/s]**
Orbit raising	50 - 2400
Stationkeeping:	
LEO drag negation	60 - 500
Annual orbit correction	15 - 75
Formation flying	1 - 500 [9]
Collision avoidance	0.01 - 0.05 [22]
End of life deorbit	120 - 150
Interplanetary:	
LEO to Earth escape velocity	3600 - 4000
Annual attitude control	1 - 10

Table 1.1: A non-exhaustive list of approximate Δv requirements for a selection of missions for nanosatellites equipped with a propulsion system. Adapted from [21] unless otherwise cited.

Orbital insertion manoeuvres are a typical primary use for propulsion systems which involve increasing the satellite altitude to its final mission location from its initial launch orbit. They typically reach as high as 2.4 km/s when considering insertions as high as geostationary orbit [21]. Additionally, constellation deployment missions must also consider Δv requirements ranging from one to hundreds of m/s due to repositioning of tens of hundreds of satellites from an initial insertion point [9]. Flexibility and thus appropriately sized propulsion systems are important for inevitable mission complications such as imprecise orbital insertion or collision avoidance. Given appropriate advance warning, the collision avoidance Δv estimate is kept small at 0.01 to 0.05 m/s [22]. This allows prohibitively low thrust electric thrusters to conduct a thrust period of sufficient length to avert potential collisions and ensure its safety.

End of life deorbiting is required to manoeuvre a spacecraft up to a disposal or 'graveyard' orbit or to expedite the orbital decay process and burn up in atmosphere. As previously discussed, this manoeuvre which may range from 120 - 150 m/s [21], is quickly becoming a requirement in all Δv budgets in order to conform with space debris regulations and minimize future risks.

Nanosatellite interplanetary travel stands the most to benefit from EP, where high specific impulse systems can achieve appreciable thrust over long duration missions requiring several km/s of Δv capability. Dramatic reductions in the fuel mass fraction leaves more room for hardware such as scientific instruments, power systems and computing capabilities. For example, a mission to a near-Earth asteroid starting from LEO might require at least 3 km/s [23]. While plenty of large-scale EP systems have no trouble reaching this requirement, there is still work to be done on system miniaturization so that a CubeSat may navigate deep space on its own.

1.4.1 Missions Uniquely Enabled by ESP

An ESP systems' unique ability to achieve efficient sub-μN thrust coupled with low noise impulse bits (10^{-7} Ns or lower) has launched it into the spotlight for specialized missions such as spacecraft disturbance reduction and as a high precision attitude control system alternative.

ESP was successfully demonstrated in space for the first time in 2016 aboard the LISA (Laser Interferometer Space Antenna) Pathfinder spacecraft. It functioned as part of the disturbance reduction system, employing an array of colloidal micro-Newton thrusters to counteract the subtle but significant solar radiation pressure in interplanetary space. This engineering feat aimed to validate the concept of a 'drag-free' spacecraft, laying the groundwork for a prospective full-scale LISA mission. In this context, clusters of electrospray thrusters coupled with specialized control software are one of many key systems required to allow the laser-based measurement of the movement of masses perturbed by extra-galactic gravitational waves where the sensors themselves are arranged in an equilateral triangle with side lengths of approximately 2.5 million kilometers [24]. Results provided by the LISA Pathfinder mission underscore the feasibility of high precision thrust, providing 0.1 μN thrust resolution and $\leqslant$ 0.1 μN Hz$^{-1/2}$ thrust noise [25]. This significantly reduces differential acceleration noise, enabling the spacecraft walls to track the masses within a margin of 10 nm and effectively creating the "quietest place in space", as described by the ESA in reference [26].

Large spacecraft such as the Hubble maintain outstanding pointing accuracy, but this is due in part to their large mass. Controlling smaller spacecraft proves challenging with current technologies. Decreased impulse bit control, or, the ability to turn thrusters on at shorter firing intervals with less force translates to higher attitude pointing precision. Existing attitude determination and control systems (ADCS) incorporate heavy reaction wheels and imperfect moving mechanical parts can cause disproportionately large jitter effects. In replacing traditional ADCS with ESP, size, weight, power, and cost constraints are relaxed and system simplifications are available. Additionally, the burden of instrument sensitivity may be reduced for specific payloads that had to accommodate for ADCS noise [27]. In one example, ESP theoretically enables precise pointing of narrow optical beams which could provide high link efficiency leading to exceedingly high data rates up to 5000 times faster than current LEO CubeSat communications technology [28].

1.5 Thesis Motivation and Organization

The focus of this research is to explore an electrospray emitter geometry in which an increased throttling range may be achieved, thereby improving ESP capability for potential use on small spacecraft. A secondary goal is to contribute to the knowledge gap in emitter fabrication with computer numerical control (CNC) machining processes. This acts to provide a platform for rapid prototyping of new ESP concepts, as well as facilitate access to ESP research using conventional fabrication methods.

The following chapters will explore these research contributions in more detail with the following framework: a literature review in Chapter 2 where general electrospray history, theory and applications to spacecraft propulsion is provided. The overall thruster prototype design and modelling as it was used drive design and predict operation is presented in Chapter 3. Emitter tip fabrication is discussed in Chapter 4. The experimental setup, testing and results are discussed in Chapter 5.

2 Electrospray Propulsion Overview

Electrospray propulsion (including FEEP) has been demonstrated in a number of in-space trials [25, 19] to be a leading candidate for a small form-factor propulsion system solution, capable of highly scalable precision thrust (nN - mN) [29], and excellent fuel economy (2000 - 4000+ seconds of specific impulse) [18]. Its operation, to be discussed in detail in this chapter, consists of the application of a sufficiently high electric field to a conductive propellant in order to induce a pseudoconic state, known conventionally as a Taylor cone, where charges are extracted and subsequently accelerated, thereby generating thrust.

This chapter will provide a review of the theoretical background of electrospray phenomena and the state of the art in ESP. Topics covered will include: a general overview of electrospray and its relevant parameters for propulsion performance, the benefits of IL propellant, as well as ESP architectures including their fabrication and their operating modes. The bulk of this thesis focuses on fabrication and testing using the porous emitter architecture and therefore special attention will be given to porous flow dynamics relating to ESP. Finally, research on thruster lifetime extension and multimodal operation as it relates to this thesis are discussed.

2.1 Electrospray History

The history of electrospray and the emergence of the field of electrohydrodynamics (EHD), or, the fluid motion induced by electric fields, can be traced back to Lord Rayleigh's theoretical analysis of the maximum charge that a droplet could carry before rupturing, now known as the Rayleigh limit [30]. Thirty years later, Zeleny's work on electrifying meniscii using glass capillaries provided experimental evidence of discrete electrospray operating regimes [31]. The first interest in the use electrospray for space propulsion application is as early as 1963 [32], however, the lack of development in microelectronics and prohibitively high operating voltages (10 to 20 kV) caused progress to stall for the coming decades [33].

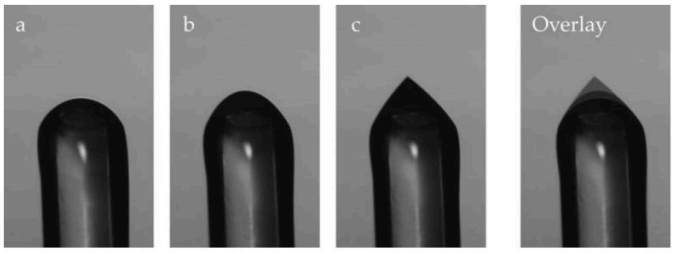

Figure 2.1: Liquid flow distorting into a Taylor cone under an applied voltage on a sharpened capillary tip (360 μm outer diameter) using ionic liquid EMI-BF_4 as a working fluid. Sourced from the experimental work of Krpoun and Shea [34].

Taylor, for whom the eponym is granted, presented an initial theoretical framework for the pseudocone phenomena in 1964 [35]. While neglecting relatively small perturbations to the conic geometry, they conclude that the cone half angle must be 49.3 degrees regardless of the working fluid properties and far-field effects. An example of the evolution of the classical Taylor cone is shown in Figure 2.1. Although more recent work has uncovered subtleties that more often reduce the cone angle below the Taylor angle [36], the Taylor cone angle works well in many cases as a first approximation.

Taylor's work would be further expanded upon with the development of the Taylor-Melcher 'leaky dielectric' model for handling EHD physics where imperfectly conducting fluids and dielectrics are studied [37, 38]. Electrospray would achieve international acclaim in 1989 when Fenn et al. demonstrated its revolutionary applications to mass spectrometry, whereby electrospray ionization facilitated the analysis of large biomolecules such as proteins [39]. Notably, they were the recipient of part of the 2002 Nobel prize in chemistry for this work.

By the 1990s, academic interest in electrospray applications had exploded. Fernandez de La Mora and Loscertales produced their foundational experimental work in which scaling laws for the cone structure and its emission current are analytically explored [40]. Cloupeau and Prunet-Foch succeed Zeleny's work wherein electrospray operating modes and the existence of a stability island are classified in great detail as a function of several key parameters [41].

Interest in electrospray applications to spacecraft propulsion grew again in the 2000s due to factors such as decreasing satellite sizes due to advances in micro-electromechanical systems (MEMS); growing demand for low-thrust precision for attitude control; and particularly for ESP, the identification of a high efficiency firing regime using ionic liquid (IL) propellants [42]. The first modern ESP devices used in a spaceflight application are those developed by Busek for the LISA Pathfinder technology demonstration mission [43].

Today, spacecraft micro-propulsion represents a small fraction of the vast field of electrospray research. Applications include but are not limited to: focused ion beams for material deposition or ablation [44, 45]; electrospinning of nanofibers [46]; and in air purification efforts [47]. The following literature review is intended to allow the reader to understand the context of the research presented in subsequent chapters. For further reading, numerous in-depth reviews on electrospray physics and its applications to propulsion, have been produced in the last three decades. These are discussed in references: [38, 36, 48, 49].

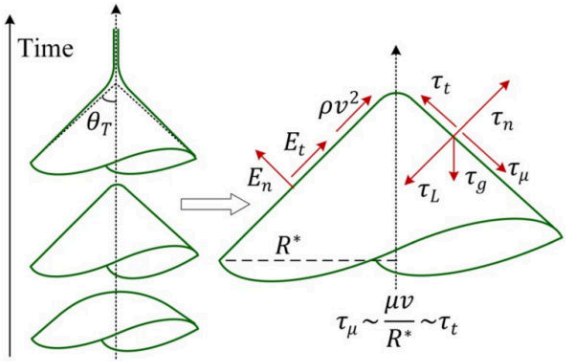

Figure 2.2: The forces influencing a meniscus leading to its deformation into the characteristic Taylor cone shape, typically with nm- to μm-scale radii (R^*). Sourced from Huang et al. [50].

2.2 Equilibrium of Forces During Electrospray Emission

The evolution of an electrified meniscus from its deformation into a Taylor cone to its subsequent breakup can be modeled through a force balance approach. As depicted in Figure 2.2, there exists the influence of stresses caused by electric (normal, τ_n, and tangential, τ_t), surface tension (τ_L, or the Laplace pressure), viscous (τ_μ), inertial and gravitational (τ_g, in regards to earthborne applications) forces [50]. These stresses on the meniscus are functions of overall emitter-extractor geometry, and propellant properties such as conductivity, relative permittivity, viscosity, and surface tension [36].

For preliminary analysis of electrospray operating mechanisms such as the determination of the critical voltage at which emission occurs, (referred to as the onset voltage, V_0), it is commonly assumed that the viscous force term equivalent to the electrostatic shear stress. This simplifies the force balance equation to one involving the Maxwell electrostatic stress, Laplace pressure, and internal fluid pressure:

$$\frac{1}{2}\epsilon_0 E_n^2 = 2\frac{\gamma}{R^*} + P_c \tag{2.1}$$

where ϵ_0 is the vacuum permittivity constant, E_n is the normal electric field strength, R^* is the characteristic radius for the meniscus, and γ and P_c is the working fluid surface tension and internal pressure respectively. The internal pressure of the fluid may be approximated as the positive or negative pressure provided by the propellant reservoir depending on the application.

Before emission onset, the meniscus sharpness is on the same order of the emitter tip used to amplify the electric field. During emission however, a positive feedback loop causes the meniscus sharpness to continually increase, reaching a point of singularity at the apex. The system sustains physicality either through charge evaporation from the meniscus or the expulsion of a nm-scale jet, releasing a spray of charged droplets and ions. Consequently, hysteresis has been experimentally observed [51] and theoretically treated [36], so that when voltage is reduced below that of initial critical onset, conic stability (subject to EHD flow effects) is maintained.

In rearranging Equation 2.1, the minimum electric field to induce emission can be expressed as:

$$E_n > \sqrt{\frac{4\gamma}{\epsilon_0 R^*}} \tag{2.2}$$

Assuming space charge effects local to the meniscus are negligible, the electric field for a given geometry and arbitrary applied voltage, V_{app} can be related through the calculation of a shape factor, C_E, with inverse length units [52]:

$$E_n = C_E V_{app} \tag{2.3}$$

This shape factor has previously been calculated by approximating an sharp equipotential tip as a hyperboloid in spherical prolate coordinates [53], but can also be calculated more effectively using finite element analysis techniques as discussed in Chapter 3. In reality, the presence of space charge would reduce the local field strength to a small extent, however its neglection for analysis has been validated in studies such as Wright and Wirz where the electric field strength contribution from the plume versus the cone was found to be 500 times weaker [54].

Finally, the theoretical onset voltage for a porous emitter can be described as:

$$V_0 = \frac{1}{C_E}\sqrt{\frac{4\gamma}{\epsilon_0 R^*}} \tag{2.4}$$

Lower onset voltages are preferred for increased power supply stability and to optimize the power-to-thrust ratio. Note that to minimize the onset voltage, one must target lower surface tension propellants, as well as increasing the electric field strength through geometric controls such as smaller radii, and smaller distances between extractor and emitter.

2.3 Operating Modes

There are a range of stable, semi-stable and unstable operating modes that affect Taylor cone shape and electrospray emission behaviour. These modes are brought on through changes in liquid physical properties (e.g. conductivity, surface tension, viscosity), flow rate, applied voltage, system geometry, and the dielectric strength of the ambient medium [41].

2.3.1 Droplet Emission Mode

The most stable and well understood operating mode is called the cone-jet or droplet mode, where a cylindrical jet extends from the Taylor cone apex and proceeds to break up into a consistent spray of droplets of low specific charge (10^2 to 10^4 C/kg). For a given range of flow rates and electric field strengths, the regime can be considered relatively stable for thrust applications and this is qualitatively shown in Figure 2.3. Notably, the jet is still inherently unstable due to unpredictable hydrodynamic instabilities. Outside of the so-called 'stability island', the jet will transition into more unstable regimes such as multi-jet or pulsating. While semi-stable and still capable of producing thrust, these operating modes are less efficient, more unpredictable, and can cause thruster damage through off-axis propellant spray.

There exists a minimum flow rate required for the steady-cone jet, which can be approximated as [40]:

$$Q_{min} \approx \frac{\gamma \epsilon_r \epsilon_0}{\rho K} \tag{2.5}$$

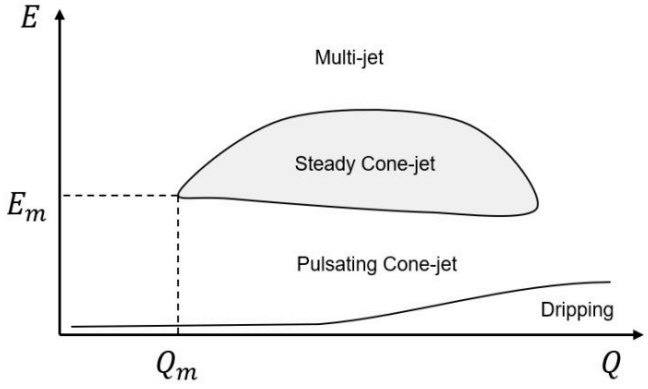

Figure 2.3: Qualitative map of high-flow (Q) electrospray operating modes under varying electric field strengths (E). The minimum critical electric field strength and flow rate for steady cone-jet emission are indicated by E_m and Q_m respectively. Figure sourced from the work of Wright et al. [55].

where ϵ_r, ρ, and K is the working fluid relative permittivity, density and conductivity respectively. Furthermore, the spray current of a steady cone-jet is independent of the electrostatic variables and may be represented by the scaling law:

$$I_b = f(\epsilon)\sqrt{\frac{\gamma Q K}{\epsilon}} \tag{2.6}$$

where $f(\epsilon)$ is an experimentally determined factor dependent on the permittivity of the working fluid [40].

Droplet operation is considered the most technologically mature version of ESP, having achieved flight proven status on the LISA pathfinder mission. In this demonstration, 7 of 8 thrusters operated successfully with some reaching over 3400 hours of lifetime [25]. Due to the relatively massive nature of the droplets, the highest thrust can be achieved for electrospray at the cost of a lower specific impulse.

2.3.2 Pure Ionic Emission Mode

As the flow rate of propellant is reduced and electric field strength is increased, ion emission begins to comprise a larger fraction of the firing regime. At low enough flow rates (often below what is predicted by Equation 2.5) and sufficiently high electric fields (10^9 V/m), the meniscus even closes completely and low-solvation ions are released solely through ion evaporation [56]. Though much less understood, emission sources that operate in the pure ionic regime (PIR) are highly sought after for spacecraft propulsion as the firing is characterized by much higher specific charges (10^5 - 10^6 C/kg) and therefore extremely efficient propellant utilization is achieved.

2.3.3 Mixed Ion-Droplet Mode

Under certain conditions, it is possible for ions to evaporate from the meniscus, neck of the jet, and from mid-flight droplets during an expected droplet mode operation. Additionally, a combination of Coulomb forces and the applied electric field can cause ion clusters and droplets to fragment mid-flight [28]. The presence of low mass, high velocity ions and high mass, low velocity droplets in the same accelerating field is a less efficient use of limited spacecraft power. Comparatively, pure droplet and pure ion mode are extremely efficient as theoretical limits can approach 100% [57].

2.4 Emitter Architectures

While it is possible for a Taylor cone to form within a conductive liquid on any surface, sharpened physical geometries that enhance the local electric field are often used to predictably stake the Taylor cone and direct fluid flow from the propellant reservoir. The most commonly studied of which are capillary, externally wetted and porous emitters as depicted in Figure 2.4. Other noteworthy emitter architectures that are not explored here involve the use of ferrofluids [58] and ultrasonic waves [59]. Emitter selection may be dependent on factors such as desired performance, ease of fabrication, and flow control mechanisms.

2.4.1 Capillary Emitters

A capillary or internally-fed emitter type uses a pressurized flow of propellant through a needle tip where MEMS-based capillaries with sub-micron inner diameters have been fabricated [60]. Their advantage lies in effective propellant management through a separate pumping system. A

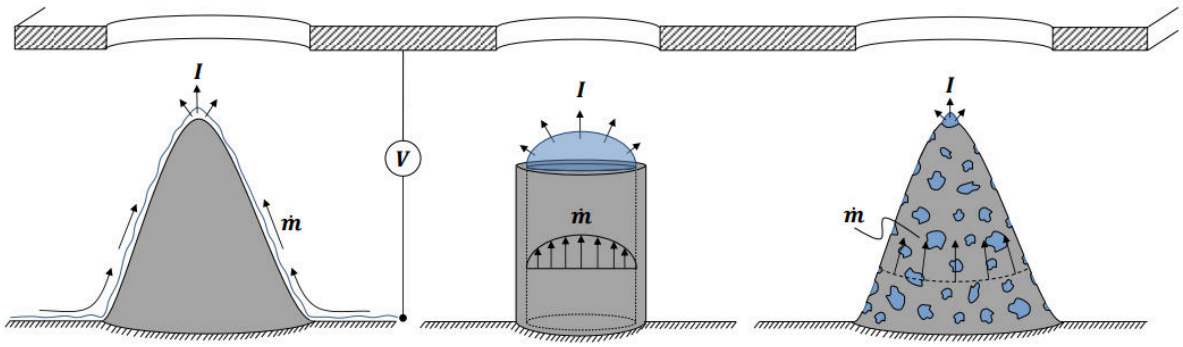

Figure 2.4: Emitter types commonly employed in ESP research showing Taylor cone formation and propellant extraction. Emitters from left to right: externally wetted, capillary, and porous. Figure sourced from the work of Coffman [44].

high degree of control over flow rate is achieved which in turn translates to easily adjusted thrust performance. However, the capillaries may be prone to clogging and the associated pumping system may add too much weight and complexity to justify for a microsatellite subsystem. These systems commonly target droplet mode operation, although the use of filling the capillaries with silica micro-beads [61] and wafer-integrated microchannels [62] to tune hydraulic impedance has been investigated to facilitate PIR operation.

2.4.2 Externally Wetted Emitters

Externally wetted or open-flow emitters, as depicted on the left-hand side of Figure 2.4, involve propellant flow over a solid, sharp protrusion. These were the focus of early high hydraulic impedance ESP efforts [63]. Operation is highly efficient in the PIR and propellant flow is passive, allowing for potential simplifications in the propellant delivery system compared to its capillary counterpart. Not only does this relieve size, weight, power and cost constraints, there is also potential to reduce system failure modes due to the reduction in mechanical components commonly required for active flow systems such as valves and pumps. However, propellant storage and transport has been highly limited for this geometry. Recent progress has been made in connecting externally wetted arrays to a reservoir with etched through-holes and utilizing the electrowetting principle in which a propellant is forced through when a sufficiently high electric potential is applied [64]. Thus, total firing time can increase from just a few minutes up to levels suitable for a space missions.

Externally wetted arrays often suffer from non-uniform wetting. Surface modifications such as the use of carbon nanotubes [65] and electrochemically etched micro-channels [66], have been implemented in previous research to enhance wicking for higher current draw. If wetted sufficiently, externally wetted tungsten emitters have shown drastically reduced beam current noise compared to other emitter architectures [66]. Externally wetted emitters are more robust to blockage from propellant decomposition products, leading to longer thruster lifetimes.

2.4.3 Porous Emitters

The porous emitter geometry involves passive capillary flow action through porous media as depicted in the right-hand side of Figure 2.4. Liquid transport capacity is increased as propellant flows throughout the porous structure. Using porous substrate with micron-sized pore diameter,

flow impedance is sufficient that operation in the PIR can still be achieved, and at higher current levels than externally wetted emitters. Additionally, porous emitters have been shown to operate at varying flow rates depending on the substrate pore size chosen, potentially allowing for operation in droplet mode or the PIR [67].

Recent porous emitters have often been paired with an upstream distal electrode with which the high voltage connection is made in order to reduce electrochemical effects that may occur at a sharp emitter apex [68]. The distal electrode seeks to spread out the buildup of a charge double layer between the high voltage connection and the propellant. As the net current is increased, the potential difference across the charge double layer increases towards a saturation limit unique to each propellant called the electrochemical window. If increased past this limit, charge transfer can occur which can damage emitter tips and decompose propellant causing clogging of flow pathways. Further, if the emitters are conductive, they can be unintentionally etched, causing tip blunting resulting in lower electric field strengths.

Further benefits of the use of a distal electrode are realized in the fact that it relaxes the requirement for conductive emitter materials and broadens the choice of materials to dielectrics such as BSG. Dielectric materials may also offer further benefits in chemical inertness and resistance to temperature [69]. The distal electrode is often used in tandem with voltage polarity alternation to further diffuse the double layer potential [70], while also taking advantage of passive spacecraft neutralization.

Porous borosilicate glass (BSG) has been chosen for experimentation due to its heritage in ESP research [71, 16, 67, 18]. As discussed, its dielectric characteristics paired with an upstream distal electrode can significantly reduce electrochemical degradation effects that accumulate over the thruster lifetime [68]. It has also been shown to be readily machined by traditional CNC manufacturing techniques which allows for rapid, cost-effective prototyping [72]. BSG is commonly categorized by its range of pore sizes which are controlled during the sintering process. Commercially, pore sizes as low as 1-1.6 μm in diameter, or 'P5' grade are available. See Table 2.1 for a short breakdown of each borosilicate grade. Other common porous emitter materials include carbon xerogel [73], tungsten [74], Nickel [52], and ceramic [75].

Grade Designation	Pore Size [μm]	Porosity [% void]
P00	250 - 500	30
P0	160 - 250	33
P1	100 - 160	34
P2	40 - 100	36
P3	16 - 40	41
P4	10 - 16	42
P5	1.0 - 1.6	48

Table 2.1: Commercial borosilicate glass grade designations (ISO 4793-80) according to their approximate porosity range.

2.4.4 Emitter Multiplexing

The thrust produced by a single emitter is usually on the order of tens of nN. In order to obtain appreciable thrust values to accomplish propulsion objectives, emitters are often fabricated in an arrayed format. An example of multiplexing emitter tips in a triangular format is depicted in Figure 2.5. Depending on the emitter architecture and fabrication technique chosen, array

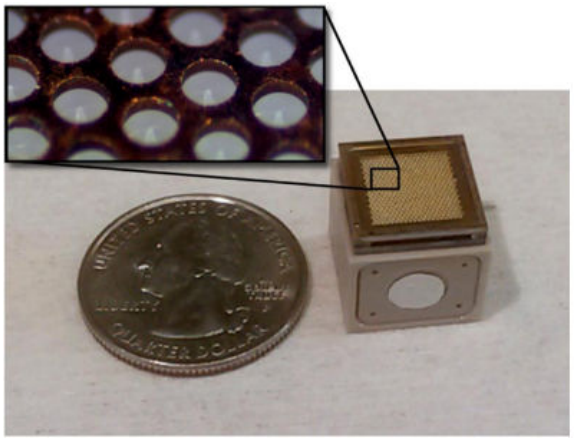

Figure 2.5: A 1 cm^3 ionic electrospray propulsion system (iEPS) module with 480 total BSG tips, some of which are visible below the extractor in the inset. Image sourced from the MIT Space Propulsion Laboratory [76].

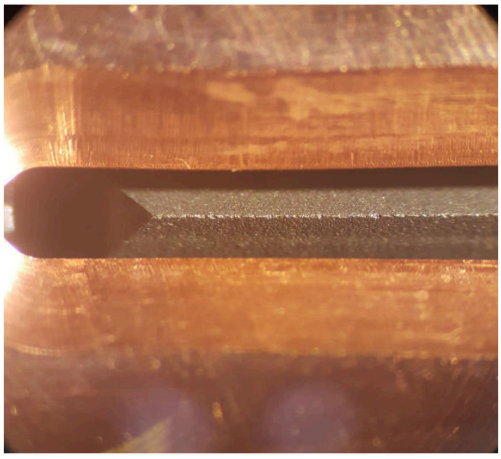

Figure 2.6: Top view of the apex section of a 17.8 mm total length porous tungsten wedge below a 1 mm width slotted copper extractor electrode. Image sourced from Wright [77].

densities of 100 - 1000 per cm^2 are typically observed but in some cases can reach as high as 4 million emitters/cm^2 while utilizing MEMS techniques [60]. Specific to porous emitter geometries, wedge shapes (ex. Figure 2.6) have been used where multiple Taylor cones can form along the tip, theoretically predicted to be spaced 50 - 300 micron apart [54]. Similarly, an annular capillary ring with multiply spaced Taylor cones operating in droplet mode has been manufactured by Busek [27].

During array fabrication, relative emitter uniformity is of foremost importance. Emitter material heterogeneity and manufacturing process repeatability quickly complicates the resulting array. No two emitters will be alike in regards to important characteristics such as onset voltage, emission site positioning, flow rate, and firing axis, thus reducing thruster overall performance and lifetime. When raising the voltage across non-uniform tips or edges, Taylor cone formation across the array is staggered. As the voltage is raised further to involve more tips, the initially emitting Taylor cones progress towards unstable firing regimes causing off-axis emission and potential thruster damage. Therefore, a poorly fabricated emitter array may have an upper firing limit that does not use its thrust area to the fullest extent.

Chen et al. provide an experimental analysis of the effects of emission site spatial distribution by varying the flow rate across a number of arrayed ceramic wedges with varying degrees on non-uniformity [75]. Site spatial distribution is characterized through optical imagery, where points of varying luminosity were assumed to be clusters of emission sites. It is unlikely that Taylor cones themselves are luminescing during the emission process, as Uchizono and Wright's studies on beam target biasing hypothesize that the illumination is caused by secondary species production, particle backstreaming and interactions within the plume [78]. Nevertheless, this is still a useful characterization for identifying areas of non-uniformity and their behaviour. Chen identified zones along emitter surface that grow in brightness from dark to intermittent, to lit, and finally to highlighted with increasing voltage. Highlight zones were prone to appear in tests with higher flow rates followed by sparking and premature thruster failure, leading to the conclusion that propellant flooding is occurring which cannot spread fast enough across the emitter tips, necessitating the need for higher flow resistance. Periodic and step current fluctuations were also observed constant voltages which increase in frequency with tip non-uniformity. This was attributed to periodic flood

relief from high flow areas to low flow areas, while step fluctuations were caused by intermittent zones turning on and off due to slightly varying flow rate.

2.5 ESP Performance

Propulsion performance measurements such as thrust and specific impulse are inherently difficult to obtain for electrospray propulsion (ESP) due to its associated low thrust and mass flow rates during operation, especially in the PIR. While direct thrust measurement methods such as the use of a torsional thrust stand balance [16, 27], magnetically-levitated thrust stands [79], or vacuum-adapted mass balances [71], may be preferred for higher confidence measurements, such diagnostics quickly increase in complexity and cost in order to meet the required instrument sensitivities.

Alternatively, there are indirect methods available to calculate expected performance based on plume properties such as current density, mass flux, plume potential, specific charge distribution, beam angle, and mass flux [80]. Current measurements may simply be obtained from the measurement of plume impingement on a downstream beam dump. Time-of-flight (TOF) mass spectrometry methods [81, 82], are used to infer specific charge and mass flow rate through the measurement of the flight time of particles across a known distance:

$$\frac{q_i}{m_i} = \frac{v_e^2}{2V_a} = \frac{I_b}{\dot{m}} \tag{2.7}$$

where q_i and m_i are the charge and mass of the i^{th} species, V_a is accelerating potential of the plume. Given the emitted current, I_b, the expected mass flow rate can also be inferred using TOF.

Due to system energy losses such as in the upstream power and control circuit, within the Taylor cone itself, or from ion fragmentation within the plume, the the potential of the plume will be lower than the emitter potential [71, 83]. Therefore, TOF measurement may be complemented with a plume potential measurement obtained by retarding potential analysis for a further reduction in performance assumptions. In this proof of concept research, average specific charge is approximated assuming emission is occurring similar to that of data found in the literature:

$$\left\langle \frac{q_i}{m_i} \right\rangle = \frac{q_i}{\sum_i f_i m_i} \tag{2.8}$$

where f_i is the species fraction found within the plume. Ideally, the specific charge distribution should be as monoenergetic as possible. A wide distribution of specific charges such as those observed while operating in the mixed ion-droplet regime, will waste energy by accelerating particles of different masses under the same potential field [57]. Termed the polydispersive efficiency, this metric is often measured to be approximately 90%. One of many metrics used to calculate the total thruster efficiency which is predicted to be as high as 90%. Other efficiency metrics include:

- Transmission - based upon the fraction of particles that impinge upon the extraction grid. The intercepted current fraction is typically low, resulting in efficiencies up to 90% or more.
- Angular - represents the reduction in thrust by ions emitted at non-zero angles relative to the axis of thrust. Significant efficiency losses have been observed resulting in metrics up to 70% [57].
- Energy - calculated as the energy required to solvate ions from liquid propellant, or the difference between the emitter and beam voltage. This is measured to be as high as 95% [71].
- Mass Utilization - represents the actual propellant mass converted to usable thrust. Due to difficulties in measuring porous mass flow rate, this is often assumed to be 100% but

has been observed to be as low as 40% when comparing TOF results to mass balance measurements [57]. Anomalous mass loss is hypothesized to be due to the backstreaming of high-energy particles towards the emitter tips, causing propellant decomposition [84].

Given the beam potential, emitted current, and the average mass to charge ratio, expected thrust can be calculated as:

$$T = I_b \sqrt{2V_a \left\langle \frac{m_i}{q_i} \right\rangle} \tag{2.9}$$

Using Equation 1.4 and 2.7, the expected specific impulse can be calculated as:

$$I_{sp} = \frac{1}{g_0} \sqrt{2V_a \left\langle \frac{q_i}{m_i} \right\rangle} \tag{2.10}$$

Finally, thruster power can be calculated using measurements from the shunt and voltage divider resistor network located on the data acquisition and control board upstream:

$$P = I_{shunt} V \tag{2.11}$$

The discussed performance parameters provide quantitative estimates of how to behaviour of an electrospray thruster in orbit. To enhance efficiency, thrust, and impulse bit resolution, it is essential to maintain emission stability (i.e. individual Taylor cone stability) within a range that does not favour off-axis spray and excessive thrust noise.

2.5.1 Emitter Stability Ranges

Increasing the limits of the stability island as depicted in Figure 2.3 is of interest for increasing electrospray capabilities. For example, Naderi et al. observed that the stability island could be increased by up to 50% when a curved counter electrode is used [85]. Additionally, larger gap distances and capillary diameters were found to expand the region at the cost of higher onset voltages.

In another study, the ranges just above steady cone-jet for a capillary architecture were explored at higher flow rates and voltages [86]. Results suggest that the steady cone-jet transfers spraying modes into an oscillating emission cone-jet with a frequency of several kHz alongside individual or simultaneous increases in flow rate and voltage. Compared to other unstable modes, the oscillating cone-jet mode still demonstrates stable, low-noise output with acceptable levels of grid impingement, thereby making it another possible suitable operational mode for thrusters in addition to the steady cone-jet mode.

Due to the difficulties involved in measurement and control of flow rate in porous emitters, the stability island concept has not yet been applied as extensively. Although emission may be measured as soon as the characteristic V_0 is surpassed, it cannot yet be considered stable. Due to an imbalance in flow rate caused by substrate inhomogeneities and hydrodynamic effects, emission can be intermittent, wherein the propellant is ionized and ejected faster than it is replenished. Huang et al. classify the stable and unstable current modes for a single conic porous nickel emitter across it's characteristic operating voltage range [87]. As the voltage is increased, the current undergoes intermittent shot and square pulsation, continuous and finally, unstable emission. They also observe evidence of composited current modes in time and space, where an emission site may be alternating between the two modes or demonstrating them at the same time, indicating at least

two emission sites on the same tip. The transitions between these modes can be described using the electric bond number, Bo_e:

$$Bo_e = \frac{\epsilon_0 E^2 R^*}{4\gamma} \tag{2.12}$$

which is a dimensionless quantity used to analyze the importance of electrostatic stress to surface tension forces. If E_0 is the electric field intensity corresponding to the characteristic onset voltage of an emitter, then the following relation can be drawn:

$$Bo_e = \left(\frac{E}{E_0}\right)^2 = \left(\frac{V}{V_0}\right)^2 \tag{2.13}$$

Huang et al. determined stable, single-site emission to occur within a critical average bond number range of 1.4 - 1.6 for porous nickel emitter tips using EMI-BF_4 propellant [87]. The existence of a predicted stability range for porous ESP has important implications in using Equation 2.13 to assist in the emitter prototype design and make operational predictions about thruster stability.

2.5.2 Electric Field Shielding and Edge Effects

In general, electric field edge effects are characterized by sharp declines in the potential field gradient, particularly around curvatures that are much sharper in comparison to the electrified bulk material. This is a common issue for the ends of wedge emitter geometry that must be considered during the design phase. A non-uniform electric field that spikes at emitter edges will cause early Taylor cone formation and further, early destabilization when the applied voltage is increased to that of the uniform emitting region. To mitigate these effects in their BET-MAX and 300-P design, Busek Inc. has integrated enlarged circular cutouts in their slotted extractor aperture edges to reduce the local electric field strength [88]. Demmons et al. explore an annular porous wedge geometry which would mitigate edge effects normally characterized by sharper electric fields at linear wedge ends [27].

In densely packed emitter arrays with similar aspect ratios, an electrostatic shielding phenomenon can occur, leading to a reduction in the local electric field. A useful parameter for analysis, the field enhancement factor, β, is the ratio of the local electric field to the background field. Harris et al. developed a model for field emission applications in order to study the effect of emitter aspect ratio (emitter height over tip radius) and pitch on the field enhancement factor [89]. Their findings revealed that independent of field enhancing tip sharpnesses, shielding must be considered when emitter pitch is comparable to their heights. Shielding was considered to be negligible when emitter spacing is greater than 2.5 times the emitter height. As the pitch decreases, β also decreases sharply up to a certain point, after which it increases again as the equipotential surface approximates that of a single emitter with a larger tip radius. Similar conclusions were observed in Ma's electrostatic finite element modelling of porous electrospray emitter geometries [90]. Additionally, for single emitters, Ma observed that when the ratio of emitter base to height increased to greater than 1.5, electric field strength becomes nearly independent.

2.6 Porous Flow Dynamics for ESP

The modelling and experimental work in the subsequent chapters builds upon the use of the porous wedge geometry that has been increasingly investigated as an effective Taylor cone multiplexing strategy [71, 75, 54, 91, 92]. Therefore, a brief introduction to porous flow as it relates to general

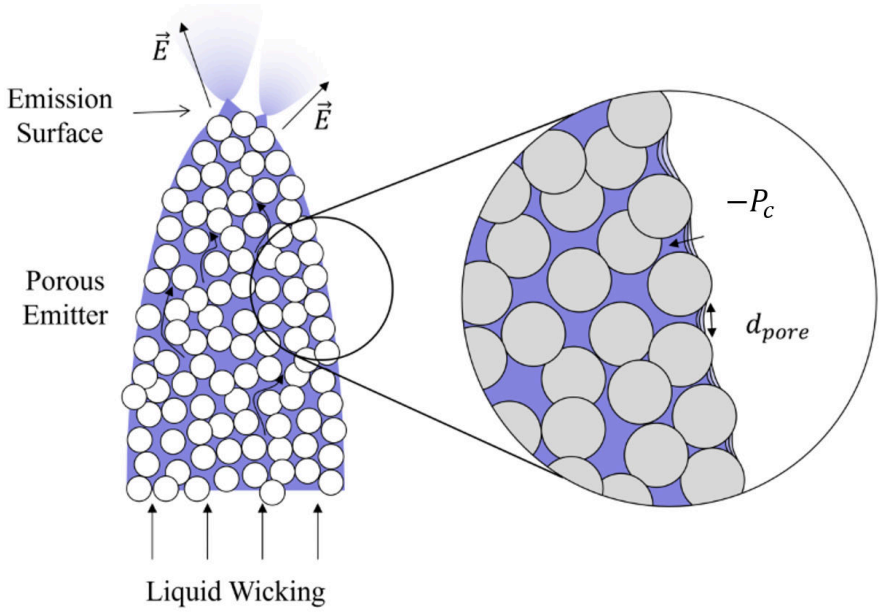

Figure 2.7: Simplified schematic of flow and subsequent emission through a porous emitter. Negative pressure reduces further according to factors such as flow rate and impedance, propellant surface tension, and pore size (Eq. 2.15). Sourced from the work of Wright [77].

porous electrospray emission is warranted. The onset voltage and current emission estimates described in this section will play a crucial role in modelling the onset voltage of parameterized wedge emitter geometries and conducting subsequent particle tracing studies in Chapter 3.

General laminar porous flow at low Reynolds numbers ($Re < 1$) is governed by Darcy's law:

$$\vec{u} = -\frac{k}{\mu}\nabla P \tag{2.14}$$

where $\vec{u}$ is the fluid velocity, k is the porous permeability, ∇P is the pressure gradient, and μ is the fluid viscosity. In this flow regime, viscous forces dominate and inertial effects can be neglected.

Emitter internal pressure, P_c, is can vary widely depending on the emitter architecture. For actively fed capillaries, the pressure is positive, while for porous media, it will be negative as a result of the upstream back pressure caused by small pore sizes. A simplified schematic of this phenomena is provided in Figure 2.7. To increase the flow impedance and encourage operation in the PIR, porous emitters are often coupled with porous reservoirs of varying porosity grade and thus, varying back pressure according to an additional static Laplace pressure, P_B, so that the internal pressure in Equation 2.1 is increased:

$$P_c = P_B - QZ = -\frac{2\gamma}{R_{p,res}} - QZ \tag{2.15}$$

where $R_{p,res}$ is the reservoir porosity, and Z is the hydraulic impedance provided by the substrate. Experiments in varying reservoir porosity have been shown to directly influence the thruster operating mode, where larger reservoir pore sizes with the same emitter tip result in an increased fraction of droplet mode emission and a decrease in the characteristic onset voltage [93]. The addition of a reservoir modifies the characteristic R^* in Equation 2.4 to involve the upstream Laplace pressure provided by a meniscus of a fully-wetted pore in the reservoir [54]:

$$V_0 = \frac{1}{C_E}\sqrt{\frac{4\gamma}{\epsilon_0 R_{p,res}}} \tag{2.16}$$

Larger reservoir pore sizes would help to decrease onset voltage, but this also has the effect of increasing the flow rate, which may or may not be desired depending on the intended thruster operating regime.

An understanding of transient flow response is especially important in a bipolar emission context, when rapid cyclic shifts in electric field strength are occurring during alternating polarity electrospray operation. To study this response in porous emitters, Wright and Wirz developed a pressure diffusion equation which considers the reduction in porous propellant storage due to local pressure fluctuations, and the characteristic pressure gradient of the emitter geometry [94]. This model enables the prediciton of flow settling times on the order of 3 ms for P5-grade BSG using properties from literature and 80 ms for porous tungsten using ex-situ measured properties. A comparison between the model and experimental data was validated, showing initial current spikes, approximately 30% higher than steady-state, after an abrupt voltage-on event. These spikes were then followed by a distinct settling time to steady emission on the same order of time as the predictive model. Additionally, unipolar tests over timescales longer than 100 seconds showed further flow development not predicted by the model.

For the first time in ESP literature, the capillary action of a porous conic emitter was observed by Chamieh et al. using X-ray imaging of the initial wetting process with a potassium iodide solution [95]. By tracking the movement of the liquid front over time, the researchers were able to make precise measurements of flow velocity, a parameter that has previously only been estimated in porous ESP research. The calculated flow velocity of their specific emitter geometry was approximately 500 μm/s. Further application of this new diagnostic method can inform propellant transport models such as Wright and Wirz's transient model, as well as assist in reservoir-emitter design through wetting optimization studies.

Wright and Wirz also introduced a useful analytical model for predicting emitted current and emission site spacing along a porous wedge [54]. Assuming that emission site spacing may be small compared to the wedge base, a solution for was developed for uniform upstream porous flow dividing into flow cells along the wedge tip. These flow cells, coupled with a Taylor cones local electric field, cause a pressure minimum at each emission site resulting in oscillating pressure saddle points. Consequently, general site spacing can be estimated to be between 50 to 300 μm as a function of applied electric field and reservoir pressure as depicted in Figure 2.8. Furthermore, for a given geometry and propellant, the total current emission from a porous wedge can be estimated independently of any perturbations local to each emission site:

$$I_b \approx \frac{\rho k \theta_w L}{\mu \ln\left(\frac{R_2}{R_1}\right)} \frac{q}{m}\left(\frac{2\gamma}{R_{p,res}} - \frac{1}{2}\epsilon_0 E^2\right) \tag{2.17}$$

where θ_w is the porous wedge angle, L is the wedge length, R_1 is the wedge height, and R_2 is the radius of curvature. This equation will be relied upon for particle tracing analyses in Chapter 3. It is important to consider, that in the case this model, the Taylor cone's radius of curvature is presumed to be at the length scale of the emitter radius of curvature. Earlier analyses suggest that a single Taylor cone cannot span multiple pores [52]. However, experimental evidence and comparisons with other models suggest that propellant pooling on the surface of the emitter may lead to the formation of Taylor cones that cover multiple pore radii sizes [96, 75].

In their work, Wright and Wirz benchmarked their multiplexed emission model against Courtney and Shea's experimental results [93]. They propose a possible description as to how specific

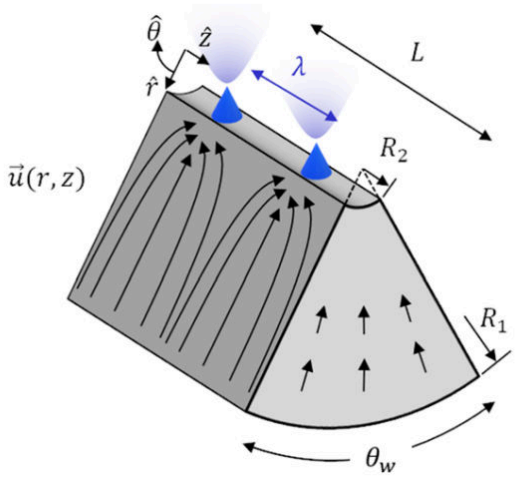

Figure 2.8: Schematic developed by Wright and Wirz to support their model of multiplexed electrospray emission showing two emission points from a porous wedge [54].

charge increases with back pressure provided by a reservoir. When the reservoir pore size is reduced, it increases the back pressure which decreases the supplied flow rate and in turn, increases the required onset voltage for the emitter. A larger required applied electric field increases the accumulation of charge inside the Taylor cone, leading to an increase of specific charge in the emitted plume.

2.7 Ionic Liquid Propellants

The propellant utilized for experimental testing in this thesis is an ionic liquid (IL) called EMI-BF_4 and has extensive research heritage for ESP. An overview of the benefits of targeting IL propellants for ESP is provided in this section.

Taylor cones can manifest under a broad spectrum of conductive fluids with distinct physical properties, ranging from liquid metals (e.g. Indium, gallium,) to solvents (e.g. Heptane, glycerol). However, for ESP research in the last two decades, the focus has largely been on room temperature molten salts termed 'ionic liquids' [56, 13]. Such fluids are completely composed of cations and anions which are bonded ionically, as opposed to the weaker Van der Waals forces found in conventional liquids. This characteristic allows for negligible vapour pressure over a wide range of temperatures, making them ideal for unpressurized containment in the vacuum of space. This attribute is particularly important for facilitating passive flow transport for porous ESP applications. Furthermore, their non-energetic and liquid phase nature, may mitigate concerns associated with the aforementioned issue of range safety, a protocol designed to protect primary payloads during launch.

Significant examples of ILs studied for ESP include 1-ethyl-3-methylimidazolium tetrafluoroborate (EMI-BF_4) and 1-ethyl-3-methylimidazolium bis(triflouromethylsulfonyl)imide (EMI-Im). Their properties of note are listed in Table 2.2. EMI-BF4 is noted for its relatively high conductivity and was the first IL to show pure ionic emission capabilities [42], while EMI-Im has demonstrated flight readiness in its use on the disturbance reduction system aboard the LISA Pathfinder mission [97].

Arguably, the most important characteristic of an IL is that while macroscopically neutral, readily separable cation-anion pairings allow for bipolar thrust operation to maintain spacecraft

Property	**Symbol**	**EMI-BF_4**	**EMI-Im**
Density [kg m^{-3}]	ρ	1280	1519
Conductivity [S m^{-1}]	K	1.36	0.92
Surface Tension [N m^{-1}]	γ	0.054	0.039
Viscosity [Pa s]	μ	0.038	0.031
Relative Permittivity	ϵ	14.5	12.0
Anion (Cation) Atomic Mass [amu]	m_i	86.8 (111.2)	280.2 (111.2)

Table 2.2: Properties at 293 K for selected ILs with significant research heritage: EMI-BF_4 and EMI-Im [98].

charge neutrality [99]. In doing so, size, weight, power, and cost constraints are reduced through the elimination of a separate spacecraft neutralizing system commonly associated with other forms of electric propulsion.

When subjected to a significantly strong electric field to encourage ion evaporation ($\sim$1 V/nm or greater), IL propellants will release a highly efficient stream of n ionic clusters that denoted as $[\text{EMI-BF}_4]_n\text{EMI}^+$ or $[\text{EMI-BF}_4]_n\text{BF}^+{}_4$, depending on the polarity of the electric field. The value of n indicates the number of neutral particles attached to the ion. These clusters are categorized as monomer ($n = 0$), dimer ($n = 1$), trimer ($n = 2$), and so on, increasing in mass with each additional neutral particle pair. As discussed in Section 2.5, an ideal emitter beam should be as monoenergetic as possible to enhance polydispersive efficiency. Moreover, large clusters of ions may undergo fragmentation into smaller clusters or even become neutrally charged under the accelerating field downstream of the Taylor cone. This reduces the thrusters performance through a loss of energy or mass to be accelerated respectively. Various ILs have demonstrated emission of distinct population distributions of clusters that can be assessed through time of flight diagnostics.

Low surface tension and room temperature melting points in ILs offer further benefits for ESP. In contrast, liquid metal propellants with higher surface tension coefficients necessitate increased operating voltages to offset the force balance outlined in Equation 2.1, resulting in increased power demands. Additionally, significant heating is required to maintain a liquid state for metal propellants, while ILs require relatively little heating, if any at all, as they are thermally stable over a wide range of temperatures and remain a liquid at temperatures as low as -50 °C [100].

Finally, the inherent flexibility in cation-anion pairing shows potential to finely tune an ILs characteristics for exactly what is required for propulsion. IL chemistry is a relatively new field, with hundreds of unique compounds under study and the potential for many thousands more to be generated for applications in drug delivery methods, solvents for chemical synthesis, batteries, super capacitors, etchants, nuclear, and nanomaterials [101]. ILs with key properties that affect EHD physics such as viscosity, surface tension, and conductivity are beginning to be investigated and optimized for ESP [50].

A leading example in propellant tailoring is in the development of hypergolic IL propellants, where multimodal propulsive capabilities may be achieved with a propellant that can operate either as a high efficiency electrospray thruster and a high thrust chemical monopropellant rocket when required [102]. More specifically, ILs paired with hydroxylammonium nitrate oxidizer have shown performance comparable to that of a traditional monopropellant such as hydrazine [103]. Additionally, the mixture is much less toxic and is therefore a strong contender in the growing field of 'green' monopropellants where focus on environmental impact and handling safety is of foremost concern [104].

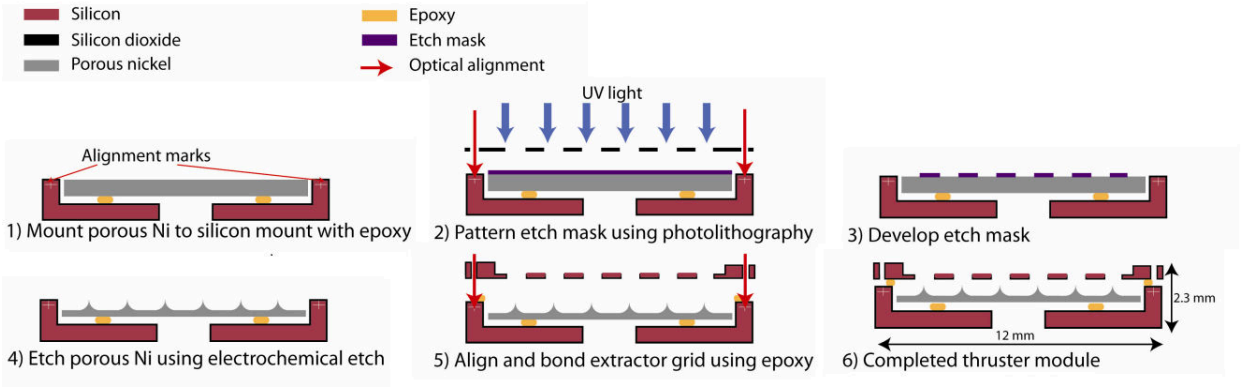

Figure 2.9: The microfabrication process developed by Courtney for etching and assembling a porous nickel array thruster package. Sourced from [107].

2.8 Emitter Fabrication Techniques

Tradeoffs in cost and complexity arise in various manufacturing methods for producing robust porous emitter arrays that exhibit uniform emission. Fabrication precision and repeatability are often contrasted with prototyping speed, while the eventuality of batch processing for production at scale must also be considered [105]. Typical issues that vary in severity depending on the manufacturing process include array tip non-uniformity, propellant flooding, and extractor-emitter alignment. For this section, the computer numerically controlled (CNC) micromilling of porous emitters is briefly covered but will be explored in detail in Chapter 4. For contrast, the advantages and disadvantages of manufacturing processes such as etching, laser ablation, and additive manufacturing are discussed.

2.8.1 Electrochemical and Ion Etching

Electrochemical etching has been used to generate metallic porous emitters with tip curvatures below 10 μm [106]. Generally, porous material is patterned with one or more layers of photoresist masking and immersed in an electrolytic solution such as sodium hydroxide. A small potential is applied in a constant or pulsed mode and as the excess material is etched away, the emitter geometry is revealed. While this process creates sharp tips, the emitter substrate is limited only to conductive material. If not properly mitigated with distal electrode use and polarity alternation, the buildup of charges at the emitter tip can cause electrochemical reactions that etch and cause blunting over long periods of time [68].

Courtney developed a fabrication process depicted in Figure 2.9 capable of producing 480-tip porous nickel arrays with targeted tip curvatures of 15 μm [52]. While etching variability led to tip non-uniformity, the resultant rounded tip array firing with EMI-IM propellant yielded high currents from approximately 0.85 to 1.6 kV with peak currents of 450 μA. One advantage of their etching process is that the tips were bonded to a silicon frame with which micro-electromechanical (MEMS) techniques could be utilized during assembly to align the extractor grid with a high degree of accuracy.

In order to mitigate issues of wettability and fabrication consistency, Xue et al. combined electrochemical etching techniques with low-speed wire cutting to manufacture externally wetted and porous tungsten tips [66]. The use of a sub-mm diameter heated brass wire cuts the rough shape which is followed by an oxide cleansing pickling process. Traditional electrochemical etching is

then applied to produce emitter tip curvatures on the order of one micron with etched microchannels on the externally wetted tip specifically to assist in robust propellant supply. The effects of varying etching voltage and time, and electrolyte concentration were investigated and emission tests confirmed lower noise, and better repeatability for the externally wetted tips.

MEMS-based deep reactive ion etching (DRIE) has been used to develop highly integrated silicon-based ESP systems that can achieve advanced alignment and are adaptable to various emitter architectures [108, 109]. For example, Dandavino et al. developed a novel capillary array electrospray module with integrated extractor and accelerator electrodes [110]. Incredibly small features afforded by the DRIE process such as 5 μm inner diameter capillaries and 50 μm emitter-extractor distances resulted in extraction voltages as low as 750 V. Additionally, the accelerator electrode could be used to grant new abilities to the system such as throttling and thrust vector control.

MEMS foundries, while highly accurate, can be costly, and require professional skills and equipment [111]. For pure DRIE applications, material choice is restricted to silicon. However, many researchers opt to bond emitters fabricated using separate techniques to a silicon frame, to capitalize on the advantages of both [29]. Owing to their compact dimensions, MEMS-based thrusters have experienced unique technical challenges related to short circuiting due to liquid flooding and high voltage insulation difficulties [108].

2.8.2 Laser ablation

Laser ablation uses a high-energy pulsed laser to vaporize surface material to mill a desired geometry with remarkable precision. For instance, systems such as a diode-pumped solid-state laser are capable of pico to femtosecond range pulses with micron-scale beam widths, allowing for high precision cutting while minimizing thermal effects [16, 112]. Given that the vaporization process is not dependent on material conductivity, the milling of dielectric substrates may be explored such as BSG and ceramics. The successful use of this process has been especially apparent in the continued development of the MIT Space Propulsion Laboratory's Scalable ion Electrospray Propulsion System (S-iEPS) over a decade in the making [113, 29, 114]. In their work, a BSG array featuring 480 tips arranged in a triangular pattern within a 1 x 1 cm footprint is manufactured using laser ablation techniques. The average emitter tip height is was measured to be 175 μm with average tip radii of 15 μm. Using MEMS techniques, the chip is bonded to a silicon frame for optimal alignment within 25 μm with individual 300 μm diameter extractor apertures. A S-iEPS submodule is completed upon integration with a $\sim$1 mL propellant tank for passive propellant delivery through a pyrolyzed carbon aerogel distal electrode placed in contact with the bottom of the BSG frit. Performance measurements for a particular testing campaign included 760 s specific impulse with 12 μN of thrust at emission currents of 150 μA over 90 hours without decay [76]. A fully integrated unit combines eight iEPS submodules, operating at less than 1.5 W, while positioned within 0.3U of a CubeSat.

It has been noted that due to formation of shell-like crusts during material melting, some materials such as BSG and quartz-based Varapor100 benefit from a hydrofluoric acid post-treatment to improve tip sharpness and emission performance [115]. However, other studies have observed BSG emitters to perform well with minimal post-processing. For example, Mallalieu and Jugroot used an Oxford Series A picosecond laser to mill linear emitter wedges out of both BSG (P3-grade) and carbon xerogel [116]. Using varied power settings (beam width), mill rates, and number of passes, the sharp emitter wedges were fabricated while preserving the integrity of the porous substructure.

Despite offering incredibly high accuracy, laser ablation is currently constrained by its high cost and time investment. For one laser, only one tip can be gradually milled at a time. Though these

disadvantages may be ameliorated with continued technological development, at present, they are currently not ideal for batch processing intended for rapid prototyping or mass production.

2.8.3 Additive Manufacturing

Additive manufacturing has been leveraged to provide the researcher with more control over the emitter substrate characteristics during fabrication. Methods such as powder injection molding, have successfully been used in field emission electric propulsion (FEEP), where porous tungsten microparticles are sintered together at high temperatures and pressures [117]. In this process, a mixture of substrate powder and organic binder are injected into a precise mold of the intended geometry under pressure. The binder is removed through thermal, solvent, or catalytic processes depending on the intended application, and the resultant substrate is then sintered at high temperatures to provide the inter-particle bonding required for the final product [118]. Additional electrochemical postprocessing is often necessary to further sharpen emitter tips and open pores.

Powder injection molding offers distinct advantages in its ability to precisely control porosity and substrate homogeneity, as a result of an intensive powder selection process. Furthermore, it allows for the creation of complicated and precise geometries using customized molds. The accuracy of the finished product is highly dependent on the mold quality which is often produced through complex die cast processes with significant capital costs, thereby restricting the overall rate of geometric prototyping. However, with the emergence of precise 3D printing processes such as two-photon polymerization have been successfully used to produce conical molds with nano and micro-scale features. In their work, Chamieh et al. utilized a Nanoscribe GT2 to print a mold for producing single-tip ceramic emitters that performed well under atmospheric electrospray conditions [95]. Conical emitters were cast with a commercially obtained ceramic slurry achieving 500 μm height and 20 μm tip curvatures.

Quraishi et al. compare multiple additive manufacturing processes and investigate the resulting quality (i.e. porosity, resolution, etc.) of ceramic emitters with substrate powders of varying particle sizes from several nanometers up to 30 μm [119]. Their focus was on relatively large mm-sized emitters, based on Porous Electrospray Thruster prototypes developed at the University of Southampton [90]. Among the different processes evaluated, it was determined that stereolithography tended to produce the highest quality finished products and were chosen for further emitter characterization. Experimental testing of the resultant emitters showed stable emission, operating up to a maximum of $\pm$3500 V with currents as high as 35 μA per emitter. Notably, the outsized results produced here are likely due to their choice of larger overall emitter design compared to other emitters in literature.

2.8.4 Computer Numerical Control Machining

Conventional CNC machining has been used in ESP research for cost-effective, rapid prototyping of emitters. Given the relative ubiquity of CNC machines, novel ideas can be explored by at lower cost by a wider range of researchers. For micromilling in particular, sub-mm diameter tooling are subjected to spindle speeds greater than 50 kRPM and have been used to produce sharp emitter tips that have comparable performance to designs found throughout the literature using MEMS and laser ablation fabrication techniques [72].

Courtney et al. were the first to investigate CNC machining of nine linear wedge emitters using P5-grade BSG [71]. A Step-Four Basic 540 tabletop CNC router was equipped with 2 mm and 0.5 mm diameter AlTiN coated endmills to machine emitter wedges approximately 300 μm in height, with tens of micron radius of curvature. A completed emitter frit contained nine emitter

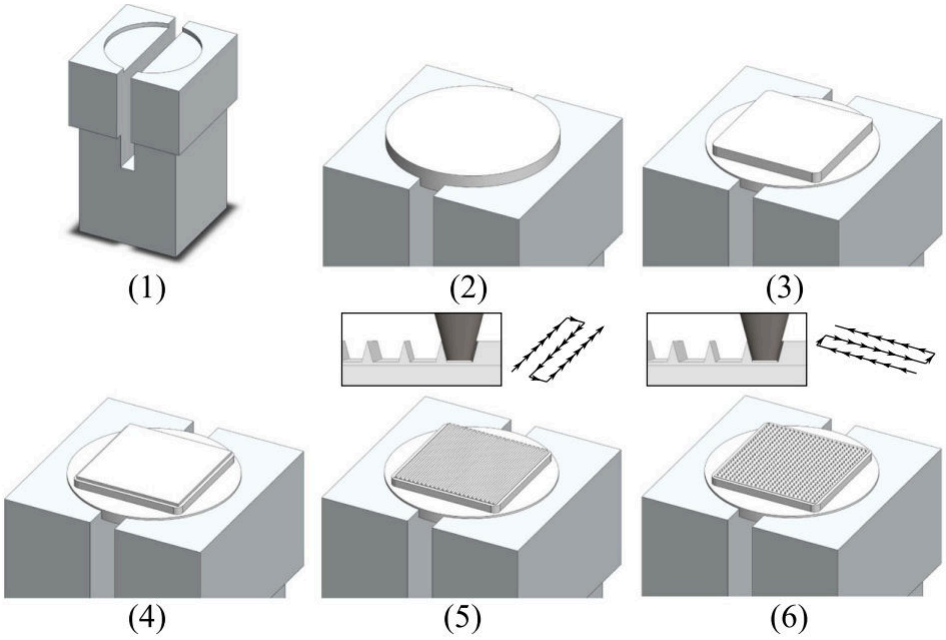

Figure 2.10: AFET emitter fabrication process outline using conventional CNC machining, developed by Natisin et al. [72]. The frit is mounted in (2), followed by a rough machining of the square base for the distal electrode and emitters in (3) and (4). The pyramid emitters are machined in both directions in (5) and (6), obtaining their square-base shape.

wedges with lengths of 7 mm and a pitch of 0.8 mm. It was noted that substrate roughness rapidly dulled tooling and a new endmill was required for each source. Despite observing asymmetric triangular profiles, and undulation along the wedge, their thruster was able to produce several hundred μA of current per cm^2, equating to controllable thrusts from 5 to 50 μN.

Natisin et al. [72] used a modified Tormach PCNC 1100 CNC and a 381 μm diameter AlTiN coated endmill to fabricate emitters and extractors for their oft-reproduced [120, 121, 122] Air Force Electrospray Thuster (AFET) series thruster. Discrete pyramidal tips were fabricated out of P5-grade BSG in arrays of 576 (emitter density 335 cm^{-2}) with average radii of curvature of 10-20 μm. Their emitter fabrication process is illustrated in Figure 2.10. They note that spindle speeds as low as 5 kRPM could be used to manufacture emitter tips, but higher speeds tended to consistently produce sharper tips. In all, their AFET-2 was able to produce highly ionic currents of up to $\pm$700 μA at $\pm$1840 V, with direct thrust measurements of approximately 40 μN.

Lojewski et al. manufactured capillary electrospray nozzles intended for aerosol generation applications [123]. A Newport TS-series was modified with high resolution stepper motors and a moderate speed spindle (up to 25 kRPM) which was able to produce nozzles with 50 μm inner diameter in compact arrays of 460 sources/cm^2. Tooling used involved 50 μm diameter microdrills and 250 μm diameter end mills. The resulting device was shown to emit exemplary primary droplet size uniformity and flow rate control, with further discussion on how their in-house built CNC could be improved further to be competitive with other electrospray manufacturing methods in areas such as machining time and cost. For example, the addition of high-speed, high accuracy piezo linear stages can be implemented on each axis for improved part accuracy and machining speed.

Ma et al. machined considerably larger 2 mm height tips in arrays of 25 to 100 for their Porous Electrospray Thruster series of thrusters [90]. In their work, P4 and P5-grade BSG was often the

emitter substrate of choice. Targeting larger emitter tips was found to make the machining process easier, consistently producing tips of high uniformity. While the CNC machine model was never discussed, 3 mm diameter cutters were used to manufacture pyramid emitters with tip curvatures ranging from 50 to 100 μm. Some of their tests also involved the use of coolant which when absorbed, was assumed to make the porous glass less brittle and thus more machinable [18]. Their thrusters were able to produce extremely high density currents, with peak values of up to $\pm$100 μA per tip observed at operating potentials exceeding $\pm$3500 V. This is likely due to tip bluntness and high potentials used would create increased emission area, resulting in multiple emission sites per tip.

In summary, while MEMS techniques can be offer high precision, they are also costly and time consuming. Alternatively, conventional CNC emitter fabrication provides broader access to ESP development, featuring a rapid fabrication process that facilitates increased prototyping of novel emitter geometries and arrays. However, inconsistencies in fabrication are much more prevalent compared to other manufacturing methods. Defects such as asymmetric profiles, apex undulation along wedge geometries, and broken or blunted tips are common. Reducing the intensity and frequency of such defects is nontrivial, given that there are a sizable number of parameters that can affect the machining process, including the workpiece material, machine, tooling and coded toolpaths. In particular, there is a noted gap in the literature regarding machining strategies for BSG for application in ESP research. The work presented in Chapter 4 aims to address this through an investigation of the aforementioned parameters to produce optimal wedges of differing geometries.

2.9 Efforts to Increase ESP Capability

In its current state, ESP system performance is constrained by limited thruster lifetimes due to propellant overspray. As a result, stringent operating parameters on flow rate or applied voltage are required to ensure electrospray stability. To enhance the viability of ESP as a preferred choice in mission design, it is imperative to conduct research aimed at extending device lifetimes, expanding the available ranges of thrust and specific impulse, and integrating new capabilities such as thrust vector control (TVC).

2.9.1 ESP System Lifetime

Improving thruster lifetime is as a key area in ESP development [124, 125, 126]. Propellant overspray as a result of sub-optimal geometric configurations and unstable off-axis emission leads to impingement and accumulation on the extraction grid over time. A schematic of the overspray process is displayed in Figure 2.11 for the colloidal micro-Newton thruster to be used on the future LISA mission [127]. For a thruster with reduced angular efficiency, the higher angles of an emitted beam are often too wide to pass through the extractor aperture. As the propellant accumulates on the extractor grid over time, further impingement can cause backspray to the emitter and surrounding thruster components. As shown in Figure 2.12, if the decomposed IL is allowed to accumulate over significant periods of time, a bridge short circuit connection can be created between the emitter and the extractor causing fatal failure of the thruster or its power processing unit.

A common diagnostic issue present in ground-based testing of ESP is secondary species emission (SSE). SSE encompasses the generation of secondary electrons, ion clusters, and droplets resulting from the impact of high-energy primary propellant particles on surfaces such as the extractor, accelerator, or collector plate [127]. These charged species can backstream towards an oppositely

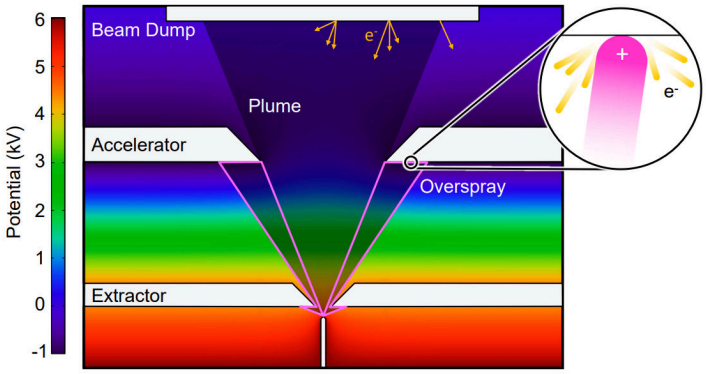

Figure 2.11: Schematic of capillary electrospray to be employed on LISA mission demonstrating overspray. A mechanism for generation of secondary electrons is through impingement of high-energy droplets and ions on electrode and collector plate surfaces. Sourced from [127].

biased emitter tip, introducing noise in thruster performance measurements and inducing undesired electrochemical reactions in the propellant. The decomposed propellant can then obstruct flow paths, leading to reductions in overall thruster performance. Furthermore, the departure of secondary electrons from the collector plate can yield an increased positive current reading that is not representative of thruster emission, often causing an asymmetric current-voltage response during bipolar thruster testing. Therefore, it is common in ESP experimentation to employ a biased SSE suppression grid downstream of the thruster, positioned in front of the beam collector plate, which emulates the behaviour of a Faraday cup. The bias is selected depending on the polarity of the incoming species and has demonstrated a sizeable reduction in backstreaming secondary species [84], as well as reducing pseudo-emission current measurement caused by secondary

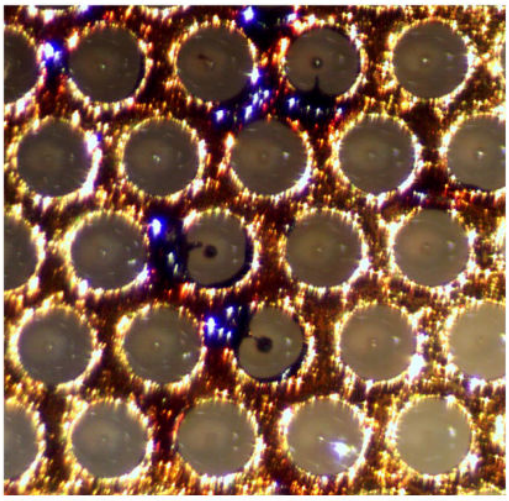

Figure 2.12: Decomposed IL that has accumulated on a S-iEPS module extractor electrode after a long duration test. Seen here, bridges to the emitter can occur in which fatal short circuits can occur. Sourced from [76].

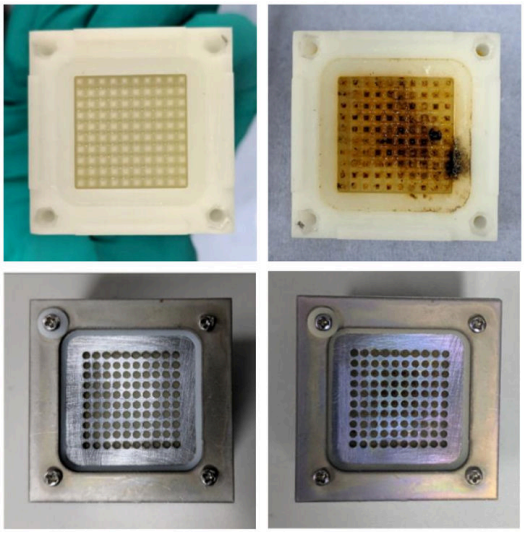

Figure 2.13: Pre- (LHS) and post-test (RHS) images of the PET-100 series emitter array (top row) and extractor (bottom row). Propellant decomposition is evident after a test duration of 18 hours. Sourced from [128].

electron emission.

In addition to misalignment, droplet and ion fragmentation caused by Coulombic fission and particle collisions lead to further beam expansion, both upstream and downstream of the extraction grid [124]. As momentum is exchanged, there is an increase in radial velocity, which not only increases impingement, but also decreases overall thrust efficiency, siphoning energy from useful axial thrust. An interesting optimization problem arises in the fact that while angular efficiency can be improved by increasing emitter-extractor distance or by reducing extractor aperture size, this also increases the likelihood of propellant impingement, therefore reducing thruster lifetime [57].

It is important to extend thruster lifetimes in order to contend with future multi-year missions such as the LISA mission, which will require operation on the order of 40,000 hours. However, current state of the art ESP system lifetimes rarely exceed 1000 hours. The most notable case is the colloidal micro-Newton thrusters aboard the LISA Pathfinder spacecraft, in which seven of eight in-space thrusters operated for over 2,400 hours [129]. Thuppul et al. investigate improvements such the use of porous grids to absorb impinging propellant, and thruster assembly optimization such as modifying grid aperture radius and grid spacing [124]. Their findings suggest that by modifying grid aperture radius and grid spacing by as little as 3-7% can improve thruster lifetime by 200-400%. Another approach was introduced by Whittaker et al., who presented an extractor concept involving the use of a thin silver film deposited on a thick dielectric frame to provide stability and resiliency to electrical shorting [121]. The frame facilitates alignment and improves extractor rigidity, while the metallic film serves as protection for the power processing unit. In the case of localized propellant accumulation around an extractor aperture that leads to a short circuit, the film can ablate, thereby clearing the short and allowing for the rest of the thruster to continue to operate safely, albeit at a slightly reduced performance. Finally, inherent lifetime limitations of ESP can be bypassed while also providing redundancy through the use of an innovative staged-system design by Jia-Richards et al. [23]. To accomplish this, fuse wire staging mechanisms are used to dispose of stages of damaged arrayed electrospray modules, revealing a fresh array for use underneath. High Δv missions of up to 1 km/s are therefore within reach for a 3U CubeSat employing just three stages, while a hypothetical mission to a near-Earth asteroid could be accomplished with eight ($\Delta v = 3$ km/s).

2.9.2 Multimodal ESP Operation

The foremost example of expanding ESP capability is through the development of multimode propulsion systems. This design seeks to capitalize on mass-savings and increased mission capability and in-situ adaptability through the use of a shared single propellant supply that may be used in two or more propulsive modes which vary in thrust and efficiency [102].

Systems in which an electrospray assembly shares a hypergolic propellant (as mentioned in Section 2.7) with a high thrust chemical counterpart can provide wide ranging mission capabilities through vast differences in thrust and efficiency between two operating modes. For example, the Monoprop-Electrospray Propulsion System currently under development uses a variation of the IL-hydroxylammonium nitrate (59% wt. HAN, 41% wt. [Emim][EtSO4]) propellant blend to achieve high thrust (1N, 180 s) catalytic decombustion and high specific impulse (0.5 mN, 1000 s) capillary [130] and porous glass electrospray operation [120].

A demonstration of multimode propulsion is accomplished through variable specific impulse ESP systems which share the same thruster. While the difference in achievable thrust between the two modes may not be as large as a chemical-electric system, the advantage lies in a smaller form factor. For example, Wright et al. developed a hybrid electrospray emitter which combines aspects of capillary and externally wetted operation to allow for varied specific impulse modes [131].

Using a coaxial needle nested inside a capillary, the emitter operates stably in high thrust to power modes at high flow rates. When the flow rate is reduced, there is a transition to a high specific impulse mode in which field emission occurs, emitting unsolvated ions as opposed to relatively low specific charge droplets. The hybrid emitter was observed to produce 360 to 430 nA of current in capillary mode with specific charges on the estimated to be 100 C/kg, while externally wetted mode produced approximately 2 nA of current suggesting a much higher emitted species specific charge.

Another way to achieve varied specific impulse operation is through the addition of an accelerator electrode downstream from the extractor. Varying the potential of a second grid can boost performance through modulation of the accelerating electric field without affecting Taylor cone stability. This effectively decouples specific impulse and emission current while increasing overall propulsive efficiency [132]. In particular, the thruster energy efficiency is improved by increasing the beam potential and offsetting the losses associated with ionic or droplet extraction as well as ohmic losses experienced in the propellant. The angular efficiency is improved as the acceleration field between the extractor and accelerator imposes a focusing effect and reduces the beam angle. Dandavino et al. exemplify the benefits of a dual-grid ESP system in their MEMS-based capillary electrospray which seamlessly integrates an acceleration electrode during the fabrication process [110]. Using 2000 V acceleration potential, the thruster beam angle was reduced by half from 60° to 30° and thrust and specific impulse was estimated to more than double at the cost of a quadrupled power draw.

2.9.3 Thrust Vector Control

A propulsion system with TVC capabilities can accomplish unique manoeuvres such as precision pointing, reaction wheel desaturation, detumbling, and compensation for a shifting spacecraft center of gravity occurring over long periods of time. These systems have the potential to replace traditional ADCS components that may be too heavy and imprecise for the CubeSat format such as gimbals and reaction wheels.

ENPULSION has accomplished TVC with their FEEP NANO AR^3 thruster model through the use of a tri-segmented counter-electrode around their crown emitters [133]. In this way, differential electric potentials may be applied to each electrode which result in relative current throttling of three regions on their 28-tip crown emitter. Using operating voltages of 2 to 10 kV, beamlet inclination angles as high as 39° were measured at 70% reduced thrust levels, corresponding to one segment operating at maximum voltage while the other two operate minimally.

Savytskyy and Jugroot have developed the Vectored Electrospray Thruster (VET) system in which TVC is accomplished through varying the duty cycle of multiple porous linear wedge emitters distributed across the thrust plane [134]. Torque magnitudes sufficient for attitude actuation are generated by situating the emitter arrays away from the spacecraft's center of mass. A two-emitter porous BSG prototype was validated with a nine-step pulse width modulation configuration along one rotation axis. Using emitters with varying grades of BSG, the thrust was estimated to be 0.37 to 2.10 μN at 2115 to 3103 s specific impulse, equating to a maximum angular of acceleration of 16.2 μrad/s.

2.10 Concluding Remarks

ESP performance in both in-flight and ground-based research has demonstrated the potential to expand CubeSat mission design space, allowing for longer duration, higher functionality missions.

The preliminary evidence for this has been covered in this chapter. The fundamentals of electrospray propulsion were explored, including the physics, performance parameters, operating modes, and common emitter architectures and ionic liquid propellants investigated in research. Porous flow dynamics and emitter fabrication techniques were highlighted due to their importance to this work. Finally, studies on increasing ESP system lifetime and capabilities were briefly reviewed, expressing the requirement for both highly optimized and novel thruster configurations to overcome existing performance issues.

The following chapter will detail the thruster prototype inspired by the AFET-2 which is used as a platform for testing linear and more complex wedge emitter geometries. Electrostatic and particle tracing simulations are also presented which served to aid overall thruster design and predict experimental results.

3 Thruster Concept: Design and Modelling

Thrust throttling for basic ESP systems are limited to a small range due to EHD instabilities that occur at voltage magnitudes larger than that of the characteristic onset voltage. To investigate expanding this range, a thruster assembly adapted from the Air Force Electrospray Thruster(AFET)-2 [72] is employed. This design facilitates swapping of emitter-extractor assemblies for rapid testing and validation of proposed emitter prototypes. First, a simple linear wedge is presented serving as baseline data for the testing of a crescent wedge emitter prototype. The crescent wedge prototype aims to demonstrate an extended thrust range for an ESP system through multi-onset voltage operation as discussed in this chapter.

To aid in design, as well as predict thruster operation and assembly flexibility, finite element modelling was performed using COMSOL Multiphysics 6.1 [135]. Specifically, the electrostatic and particle tracing modules were utilized to solve for electric field distributions resulting from geometric parameterization in emitter-extractor design. This approach mitigates electric field edge effects, and optimizes thruster operating parameters. Geometries obtained as a result of predictive simulations were implemented as fabrication targets.

3.1 Multi-onset Voltage Emitter Concept

An emitter-extractor prototype is proposed to demonstrate emission from multiple wedges sharing the same emitter substrate, but possess distinct onset voltages as depicted in Figure 3.1. The primary emitter, positioned closer to the extractor grid, consistently experiences a larger electric field magnitude compared to the secondary emitter. Near initial onset, only the primary wedge emits at a low current. As the voltage magnitude is increased and the onset voltage of the secondary wedge is surpassed, a rapid ramping of emission is observed. Ideally, this should occur while staying within the Taylor cone stability limits of the primary emitting wedge. The result is predicted to be a stepped increase in thrust achieved through a small increase of applied voltage.

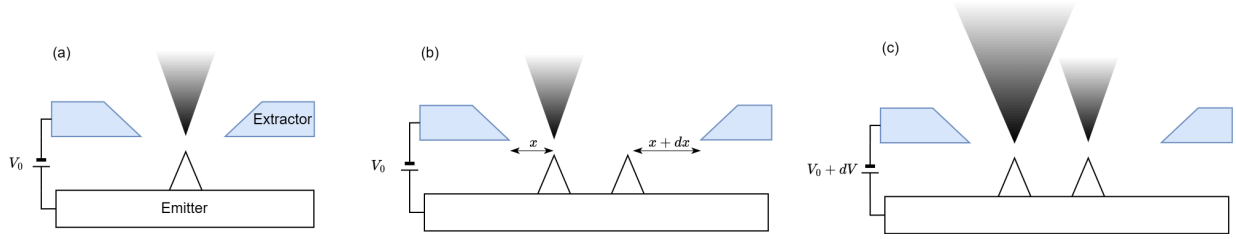

Figure 3.1: Simplified schematic of ESP operation for (a) simple wedge operation; (b) primary and (c) secondary multi-onset voltage operation.

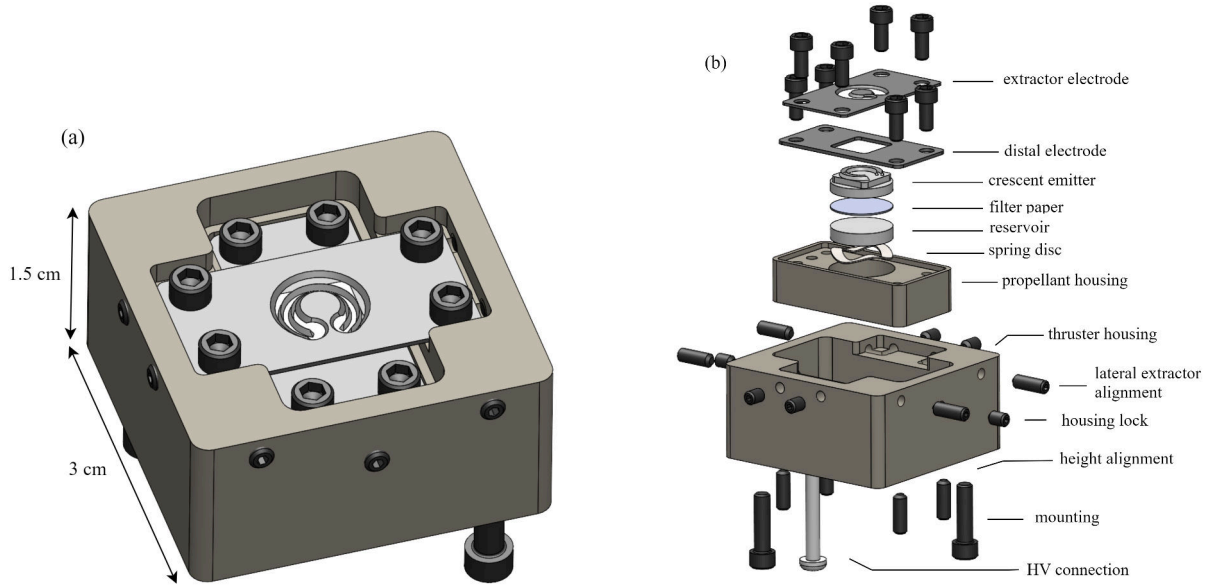

Figure 3.2: Assembled AFET-2 inspired thruster housing design with crescent wedge assembly prototype shown in (a) and in (b), the exploded view.

3.2 Thruster Housing Design

The thruster housing architecture adapted from the AFET-2 [72] consists of a propellant housing containing all of the BSG components slotted within a larger thruster housing used to mount the extractor electrode as depicted in Figure 3.2. The AFET-2 design was attractive due to its modularity and capability for fine extractor-emitter alignment obtained by multiple embedded set screws. This allows for rapid prototyping while maximizing part reuse across the design space. An exploded view of the 3 cm square by 1.5 cm thruster prototype in its crescent wedge configuration is provided in Figure 3.2b.

The propellant and thruster housing material is machined from polyether ether ketone (PEEK), an insulating material commonly used in ESP research for its low off-gassing characteristics under vacuum conditions. The propellant housing stores the BSG reservoir (P0 to P3 grade) and emitter (P4 or P5 grade) underneath a stainless steel distal electrode plate, providing coarse emitter alignment. Initially, a P0 reservoir can provide comparatively low backpressure and was used to maximize flow rate to the emitter apex, thus lowering the thruster onset voltage [93]. Subsequent tests necessitated lower flow rates to the emitter apex and so reservoirs of smaller pore size were also used. Emitter BSG porosity grades were chosen based on research heritage and perceived ease of machining.

To ensure hydraulic coupling between the reservoir and emitter, a 0.367” OD, 0.006” thick carbon steel disc spring sits beneath the reservoir and a Whatman Grade 1 filter paper is placed between the emitter and reservoir. High voltage is applied through a 1.5” #2-56 screw threaded through the bottom of the thruster and propellant housing which contacts the underside of the distal electrode.

Aluminum was chosen for the extractor material for ease of machining. Various extractors were fabricated from 0.05” (1.27 mm), 0.025” (0.63 mm), and 0.016” (0.4 mm) thickness stock for each emitter prototype. To enable alignment, twelve #2-56 set screws are threaded through

the housing on all axes. This provides adjustment of the lateral position of the extractor and vertical position of the propellant housing. With knowledge of the thread pitch of the set screw, quantitative estimates of positional shifts can be achieved through screw adjustment. For example, a quarter turn of the x+ set screw approximates a 114 μm lateral shift in the same direction.

Two mounting screws are threaded through the bottom of the thruster housing, and two additional set screws to lock the propellant housing in place after alignment adjustments are made, allowing for accommodation of alternative mounting schemes. Finally, eight #2-56, 1/8" screws were used to secure the distal electrode to the propellant housing and the extractor electrode to the thruster housing.

3.3 Linear Test Wedge Emitter

A linear wedge emitter was chosen to validate electrospray emission from a conventionally fabricated emitter. This wedge design is easily manufactured and has been demonstrated by numerous groups [54, 71, 75]. Following validation, the machining process was refined through multiple trials, adjusting machining parameters using final emitter apex quality (e.g. uniformity, sharpness) as feedback. The fabrication process for all emitters is detailed in Chapter 4.

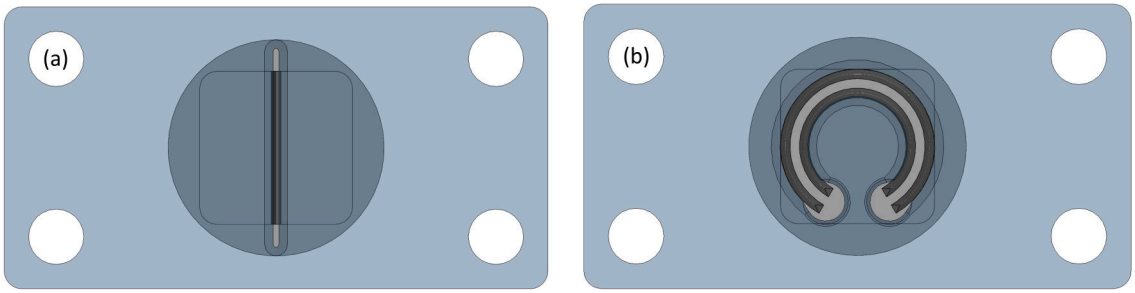

Figure 3.3: Top view of the (a) linear and (b) crescent emitter-extractor configurations.

The emitter geometry consists of a 0.6 mm height, 7 mm length triangular prism situated on a square base. Figure 3.3a provides a simplified top view of the emitter-extractor assembly, while a magnified section view of the overall assembly is shown in Figure 3.4. The square base offers coarse alignment through assembly with the distal electrode. Targeted apex sharpness was less than one μm ROC, with a side surface angle of 40°.

Initial tests used an aluminum extractor is 0.050" thickness with a 9 mm length slot extending further than the wedge length to mitigate electric field edge effects. The 250 μm width slot was chamfered at 45° to avoid impingement during plume expansion. The furthest emitter-extractor distance possible is 400 μm when the height set screws are fully retracted.

3.4 Crescent Wedge Emitter

The crescent emitter-extractor prototype achieves multi-onset voltage capability through placement of an extractor electrode of sufficient slot width over two wedges such that one wedge-extractor edge pair is closer in distance than the other pair. A simplified emitter-extractor schematic is provided in Figure 3.3b. The total slot width is 1.7 mm to make a lateral extractor electrode distance of 325 μm and 400 μm to the inner and outer wedges when the vertical distance between the two components is minimized. This results in a predicted onset voltage of 1750 V and

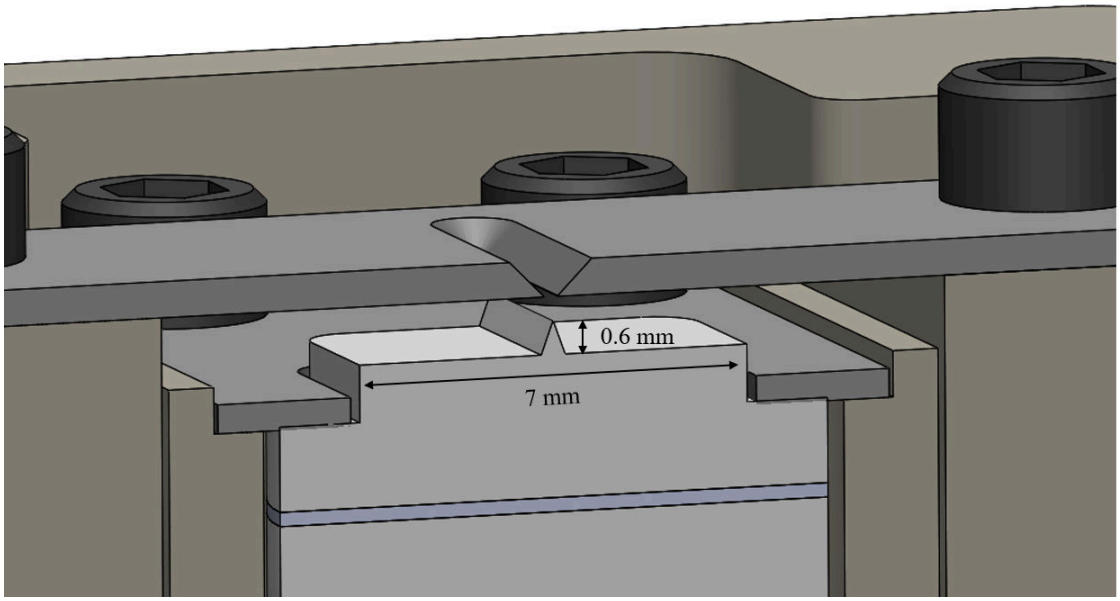

Figure 3.4: Magnified section view of the simple linear emitter wedge assembly.

2100 V for the inner and outer wedges respectively. The closeness of the physical thruster onset voltage to the intended voltage will depend on factors such as machining tolerance and assembly accuracy. The crescent geometry was chosen over a simpler linear design that might achieve the same multi-onset capability to maximize current output from 10 mm frits in the case of nonuniform apex fabrication, as well as demonstrate complex milling toolpaths. The outer wedge was chosen as the secondary emitter for ease of extractor manufacturing as reducing the inner radius of the extractor further would create a weaker bridge of aluminum material to the center of the electrode.

The emitter geometry consists of two P5-grade BSG wedges extending 300 degrees radially. The wedge geometry is the same as the linear wedge emitter. A apex-to-apex pitch of 860 micron and a wedge length of 17 and 14.5 mm is achieved for the outer and inner emitter respectively. For the extractor electrode, the slot is widened and chamfered underneath at the prism apex in order to mitigate edge effects. Additionally, the wedge end apexes are blunted to further reduce edge effects. These design decisions were informed by an electrostatic study of multiple electrode geometries intended to weaken edge effects as presented in Section 3.6.1. As with the linear extractor, the top surface of the electrode also incorporates a 45° chamfer to mitigate plume impingement.

3.5 Electrostatic Modelling Studies

Nanosatellite propulsion systems typically operate within a power draw range of only several watts, derived from a total power budget of 30 - 50 W generated by the spacecraft solar cells. For ESP in particular, an intermediary power processing unit that includes a high voltage converter is essential to achieve the required voltage gain from a varied battery supply voltage (8 - 17 V, depending on battery and power management configuration) for thruster operation in the kilovolt range [136]. While designing a power processing unit with high efficiency, reliability, and a small form factor is crucial for the nanosatellite format, equal attention should be given to electrospray geometry to reduce the load on the nanosatellite power system. For flight-ready applications, the optimal lowest onset voltage ensures minimal power consumption, smaller component footprints, and ro-

bust electrical operation. In this context, a finite element method approach is used to simulate the electric field distribution based on voltages applied to boundaries throughout the domain. Taking the reservoir pore diameter to be the characteristic pore radius and using Equation 2.4, the approximate onset voltage for the emitter can be calculated. Various geometries have been explored throughout this research: a 2D single prism emitter, an axisymmetric 2D concentric emitter, and 3D symmetric linear and crescent emitters. Additionally, multiple crescent extractor geometries are investigated to alleviate electric field edge effects.

3.5.1 Linear Wedge Assembly Parametric Geometry Sweeps

To explore preliminary design considerations aimed at reducing the thruster onset voltage for experimentation within the limits of the laboratory power supplies, the linear wedge test emitter was modeled using 2D electric field analysis studies [54]. The simulation domain consisted of three materials: vacuum, an emitter made of borosilicate glass, and an aluminum extractor slot. Charge is conserved throughout the model and symmetric boundaries of unchanging electric field ($\mathbf{n} \cdot \mathbf{E} = 0$) are applied to the overall domain boundary. The extractor boundaries are grounded and the emitter boundaries have an arbitrary applied potential of 5000 V. The surface tension of EMI-BF_4 ($\gamma = 0.045$ N/m) and the reservoir pore radius of 205 μm is used. User defined variables calculate C_E, and thus, the onset voltage. An example of the calculated normal electric field strength is shown in Figure 3.5, resulting in a shape factor of 24 mm^{-1}.

A parameter sweep was performed over thruster geometries to determine which should be given priority during the manufacturing process. During a sweep over a parameter of interest, all other geometric parameters were held constant according to nominal values listed in Table 3.1. Through normalizing the length parameters using the largest values, also listed in Table 3.1, the change in onset voltage can be compared for each parameter of interest as shown in Figure 3.6. From the results, apex sharpness is shown to have the largest effect on onset voltage followed closely by the reservoir pore diameter, slot width, and extractor height. Normalized values for extractor height decrease below zero, where the extractor height was studied below the emitter apex. Extractor thickness has a negligible effect and emitter height improves only to a certain extent. This is in line with the shielding effect dependence on emitter aspect ratio as discussed in Section 2.5.2.

In some cases, aspects of final thruster operation had to be considered that could not be included in the simplified model. For instance, while slot width showed optimal performance at

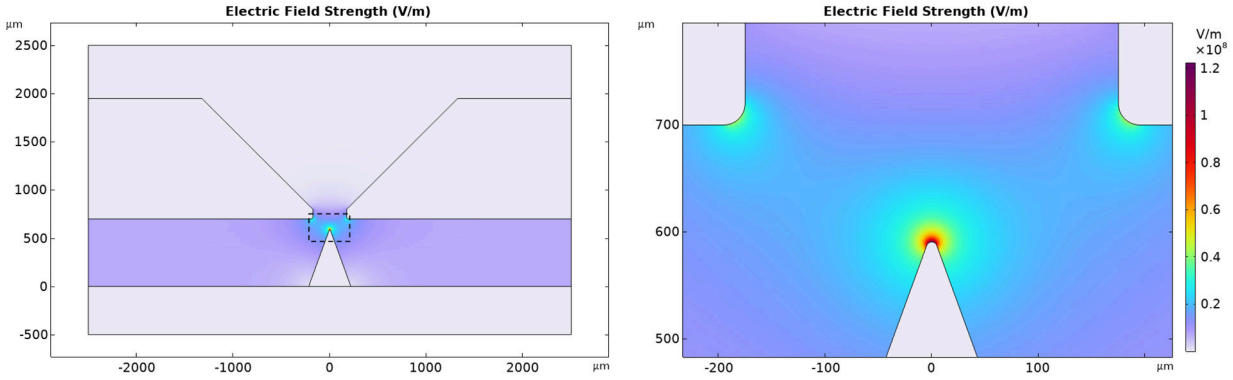

(a) Total 2D linear wedge domain.

(b) Magnified view of wedge apex.

Figure 3.5: Resulting electric field magnitude throughout the 2D μm-scale domain. Nominal geometric parameters are listed in Table 3.1.

Parameter	**Nominal** [μm]	**Largest** [μm]
Emitter-extractor distance	100	400
Radius of curvature	5	75
Slot width	350	1250
Reservoir pore diameter	205	500
Extractor thickness	1250	2000
Emitter height	350	1000

Table 3.1: Nominal and largest geometric parameters implemented in each normalized parametric sweep to determine onset voltage specific to a 2D linear wedge configuration.

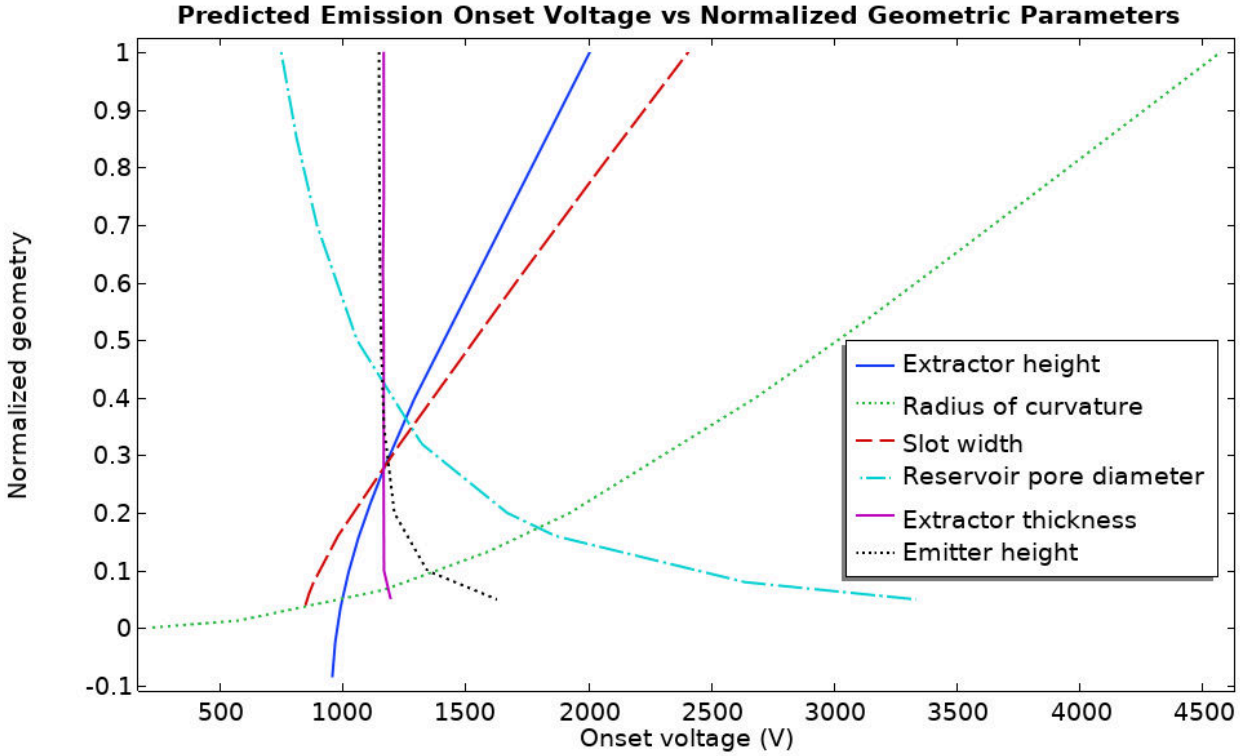

Figure 3.6: Normalized geometric parameter sweep effect on predicted onset voltage (Eq. 2.4, $V_0 = C_E(4\gamma/\epsilon_0 R^*)^{-1/2}$) for a 2D linear wedge configuration.

smaller distances, reduced slot widths would also lead to increased levels of propellant impingement as the plume expands after emission. Additionally, although larger reservoir pore diameters and thus higher flow rates may be favoured to lower onset voltage, experimental work by Courtney and Shea indicates that this diminishes the ion fraction present in the emitted plume, thereby compromising the thruster efficiency [93]. Therefore, if an electrospray design targets high-efficiency operation in the PIR, accepting an increased onset voltage as a result of larger reservoir back pressure may be necessary.

3.5.2 2D Axisymmetric Concentric Emitter Multi-Onset Voltage Study

Parametric onset voltage studies were also completed for a simplified 2D axisymmetric concentric concept emitter to examine how a variable electrode radius affects the onset voltage of two wedge emitters with a pitch of 860 μm. The inner electrode maintains a constant horizontal position

215 μm away from the inner apex, while the outer electrode distance to the outer apex is swept over a distance of 500 μm. The domain setup, materials and physics follows the same procedure as outlined for the linear emitter. Figure 3.7 plots the potential and electric field lines throughout the domain for an outer extractor distance of 650 μm to the apex. For the whole sweep, the change in onset voltage with radial extractor position is plotted in Figure 3.8. It is observed that when shifted over a distance as small as half a millimeter, the electric field strength and therefore estimated onset voltage of the outer apex decreases by almost 600 V. As expected, there is only a weak dependence of outer extractor distance to the inner emitter. These findings provide the initial targets for extractor slot width and indicate that positioning tolerance will play an important role in validating a multi-onset voltage operation.

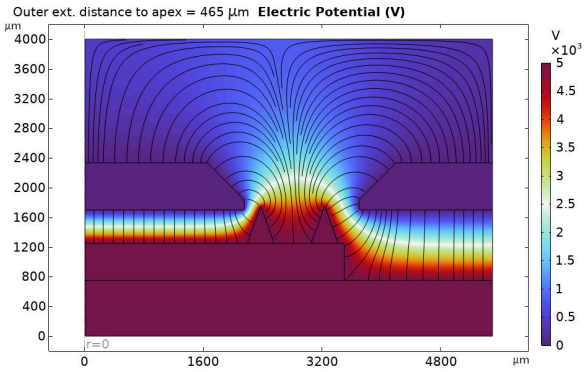

Figure 3.7: 2D axisymmetric concentric emitter concept domain with electric potential and field streamlines used to investigate differential onset voltages. The axis of symmetry is located on the left-hand side

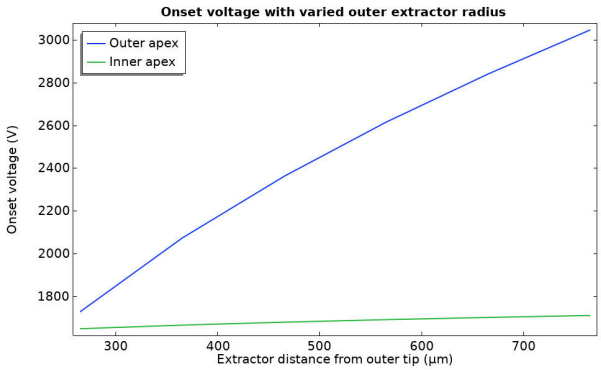

Figure 3.8: Overall change in onset voltage with varying outer extractor distance to outer apex radius.

3.6 3D Symmetric Linear and Crescent Wedge Assemblies

Three dimensional extractor-emitter assemblies were imported into COMSOL for both the linear and crescent wedge configurations. Similar to the 2D analysis, the 13 x 7.5 x 12 mm simulation domain is split into vacuum, BSG emitter, and aluminum extractor subdomains. The electric field is simulated for varying emitter potentials depending on the study of interest and a grounded extractor electrode, with symmetric electrostatic ($\mathbf{n} \cdot \mathbf{E} = 0$) outer domain boundaries. The complete simulation domains are shown in Figure 3.9.

3.6.1 Electric Field Edge Effect Mitigation Study

To explore effective strategies for mitigating electric field edge effects at the wedge end apex, several extractor and emitter geometries were simulated. These designs include a simple slot, an underside chamfer, additional clearance, and blunting the emitter apex as depicted in Figure 3.10. The underside chamfer and additional clearance aim to increase the distance between the apex point and the extractor, thereby reducing the local electric field strength. The additional clearance is 2 mm diameter cutout located at the end of the slot. In the blunted apex emitter configuration, the wedge's apex is cut at a 45 degree plane and is assembled with the underside chamfer extractor geometry.

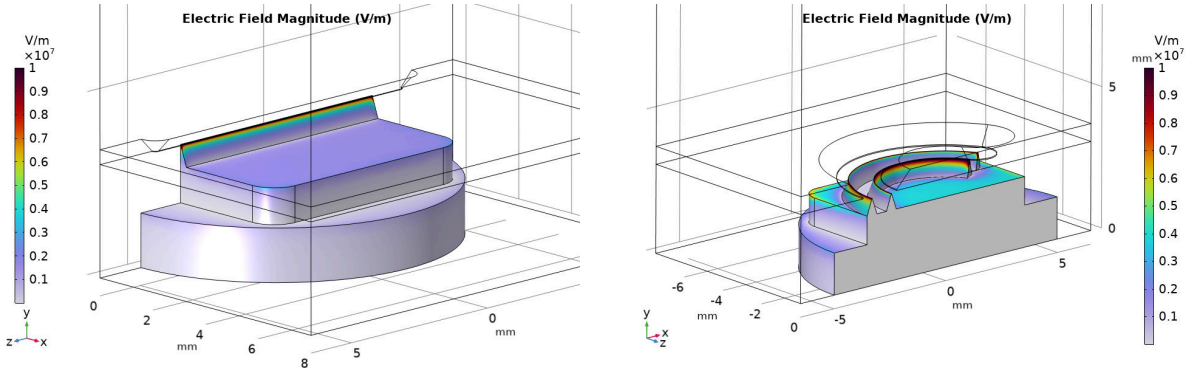

(a) Section of linear emitter domain.

(b) Section of crescent emitter domain.

Figure 3.9: Symmetric 3D linear and crescent assembly simulation domains showing electric field magnitude on the emitter surfaces given an arbitrary potential of 5000 V. Color legend maxima are limited to better visualize field distribution.

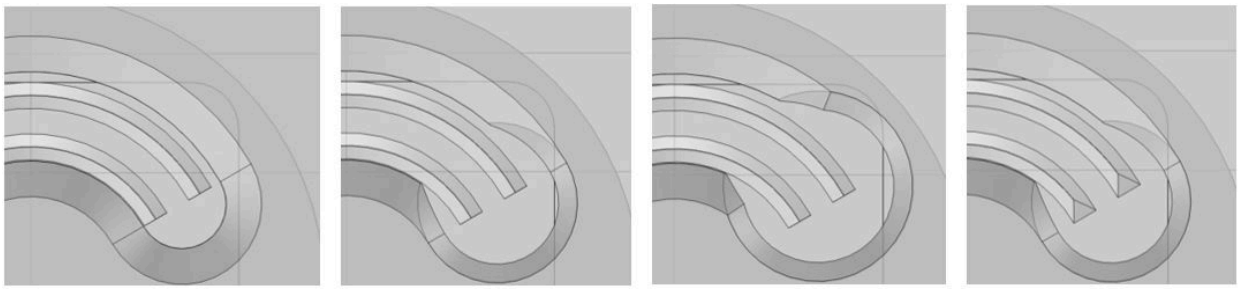

Figure 3.10: Top down views of extractor geometries used to investigate edge effect mitigation. From left to right, these include: simple slot, underside chamfer, underside chamfer with additional clearance, underside chamfer with blunted emitter apexes.

For the crescent wedge emitter, the cut line for field strength measurement follows the arc length of the wedge from the line of symmetry to prism termination. A comparison of maximum normal electric field strength on the outer and inner wedge for all extractor configurations is plotted in Figure 3.11. Noise present in the plot is likely due to finite mesh sizing and would decrease with mesh size reduction. Overall, each configuration succeeds in reducing the peak electric field strength by 1.5×10^7 V/m or more, reducing the resulting peak field strength closer to the average observed across the rest of the wedge. The combination of an underside chamfer with blunted edge apexes show the greatest reduction in edge effect field spiking, especially when considering the inner wedge where the magnitude of the peak field matches that of the inner slot. The peak field magnitude is reduced and translated further upstream of the wedge, corresponding to the sharpest point of the blunted emitter apex. When comparing the blunted configuration to that of the underside chamfer, it can be observed that the blunted apex does contribute a non-negligible amount of peak field reduction to the design. For this configuration, there is less of a field reduction effect on the outer wedge, which is evident when the same configuration is compared for both wedges as shown in Figure 3.12b. For comparison, the electric field strength across the wedge for the linear wedge geometry is plotted in Figure 3.12a.

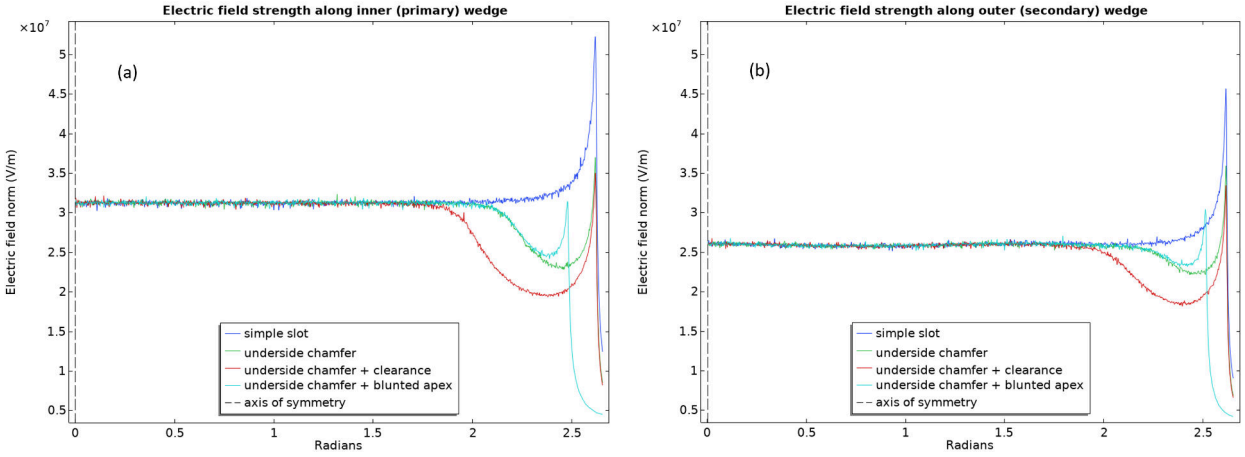

Figure 3.11: Comparison of electric field magnitude across the (a) inner and (b) outer wedges from the axis of symmetry to the wedge termination. Cut line for analysis placed 10 μm above wedge.

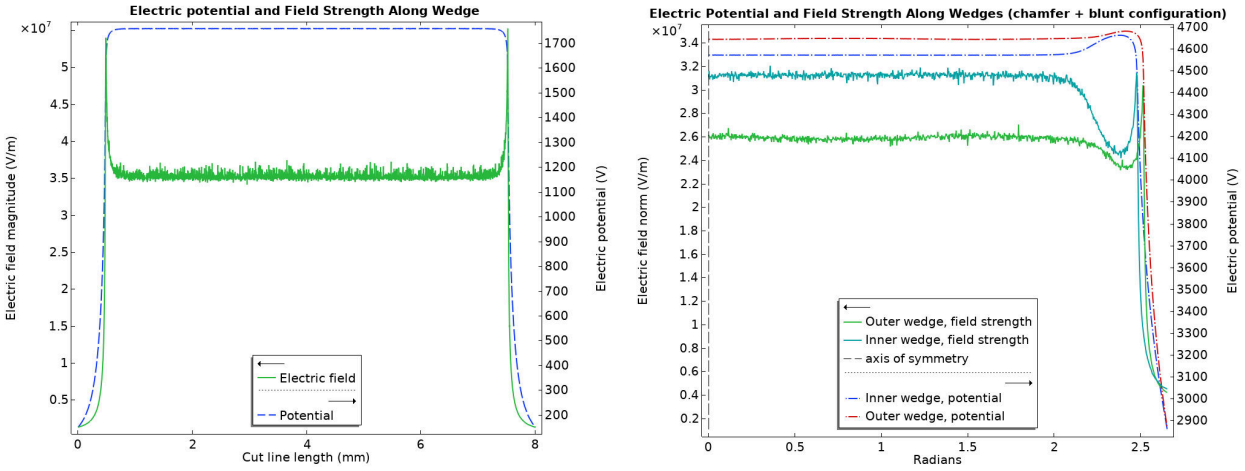

(a) Linear emitter wedge.

(b) Crescent emitter inner and outer wedges.

Figure 3.12: Comparison of electric field magnitude and potential across wedges for both emitter configurations. Cut line for analysis placed 10 μm above wedge. Note the scale difference.

3.6.2 Charged Particle Tracing Studies

The 3D symmetric assemblies were used for particle tracing studies to predict characteristics such as the plume shape and energy [90] produced by two emitting wedges with differing field strength, as well as any exaggerated plume impingement on the extractor electrode that may occur due to misalignment. The prototype design was further informed through the determination of a crescent slot geometry that would reduce particle impingement on the extractor electrode while maintaining realistic thruster operating parameters.

Particle Tracing Module Setup

Using the solution of the electric field from the emitter-extractor assemblies, the COMSOL charged particle tracing module solves a set of differential equations to obtain the motion of charged

particles. For this research, the Newtonian formulation in COMSOL is used, where, given a force, a set of second-order differential equations solve for each component of a particle's position. The electric force, F_E, is calculated using the particle charge, and the background electric field which is then used to find the acceleration of each particle in the system:

$$\mathbf{F}_E = q_i \mathbf{E} = \frac{d(m_i \mathbf{v_i})}{dt} \tag{3.1}$$

where v_i is the ion velocity of the i^{th} ion cluster under study.

The primary interaction of interest is the particle-particle Coulomb force interactions. In this context, a greater density of particles, specified based on emitted current, results in increased plume divergence due to the Coulomb forces exerted by each charged particle present in the system. For each time step, the program determines the force experienced on one charged particle, by iterating through every other particle in the system:

$$\mathbf{F}_i = \frac{e^2}{4\pi\epsilon_0} \sum_{j=1}^{N} q_i q_j \frac{\mathbf{r}_i - \mathbf{r}_j}{|\mathbf{r}_i - \mathbf{r}_j|^3} \tag{3.2}$$

where e is the elementary charge, and q_j, and $\mathbf{r}_j$ is the ion charge and position vector, of the j^{th} particle in relation to the i^{th} particle.

The contribution of space charge from ions in flight has also been demonstrated to be a driver of radial plume expansion [137]. A multiphysics interface coupling allows for a space charge computation through a control volume analysis applied on each mesh element. This is updated every time step and is adjusted depending on whether a charged particle enters or exits the domain mesh element:

$$\rho_{s,new} = \rho_s \pm \frac{eZ_i n}{V_m} \tag{3.3}$$

where n is the dimensionless charge multiplication factor representing the number of real particles for every model particle, and V_m is the volume of the mesh element. As will be discussed, the simulation will include every particle of interest and so the charge multiplication factor is set to one.

Due to scaling limitations of the particle tracing module, the assembly is assumed to be operating in the pure ionic regime. It is likely that some small fraction of the real plume contains droplets that are orders of magnitude larger in size (while still submicrometric) and lower in specific charge. Experimental results from Courtney and Shea demonstrate that, for porous thrusters with low reservoir back pressure (i.e. increased flowrates), this fraction can be as high as 50% for a P5-grade BSG emitter using in EMI-Im propellant [93]. In their hybrid axisymmetric capillary model for electrospray beams operating in the mixed ion-droplet regime, Gamero-Castano and Galobardes-Esteban demonstrate that ions experience significantly more radial expansion than high mass droplets [138]. More specifically, ions emitted from the jet experience a narrow, high angle distribution that envelops the droplet fraction, whereas ions emitted from droplets in flight are more widely distributed radially throughout the plume. Therefore, in studying the maximum extent of beam spreading and impingement, the exclusion of a small fraction droplets from the plume has been justified. A limitation however, is that ion cluster fragmentation effects known to contribute to plume expansion have not been considered in this model.

For the simulation, a cumulative distribution of positive monomers, dimers and trimers were selected to represent an emission fraction of 42%, 47% and 11% respectively. These inputs are chosen from experimental TOF measurements of EMI-BF_4 emission from a P5-grade BSG emitter

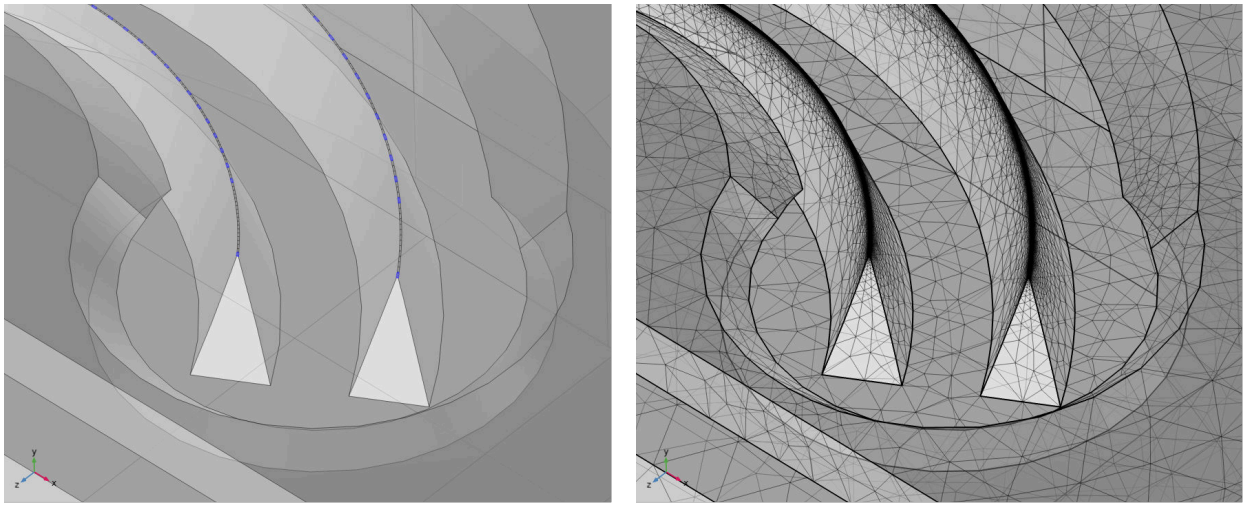

(a) 40 μm length rectangular emission surfaces. (b) Magnified view of surface mesh.

Figure 3.13: Selected emission surfaces and mesh for crescent assembly with blunted apex ends and underside chamfer configuration.

as reported by Courtney et al., neglecting the current contributions from species larger than $n = 2$ [71]. Their masses are 111, 309, 507 amu respectively. The study of negative EMI-BF_4 ion clusters were not included due to their similarities to positive cluster masses.

By applying Wright and Wirz's multiplexed emission model (Equation 2.17) and considering a total linear wedge length of 31.5 mm, the emission current from the primary and secondary crescent emitters can be approximated. A total emission current of approximately 10 μA is predicted. In actuality, this may be a slight overestimate of the current emitted from the crescent configuration, as the edge effect reducing design of the extractor will produce electric field strengths lower than what are required for Taylor cone onset just before the wedge apex as noted in Figure 3.12b, whereas Equation 2.17 assumes uniform field strength across the entire wedge length.

Thus, the total number of ions, n_i, emitted per unit time can be estimated as:

$$n_i = \frac{I_b}{e} \tag{3.4}$$

where the emission rate is 62,000 ions per nanosecond. Although current density does increase with electric field strength, the particle tracing studies were completed at 2000 V, which falls within the predicted operating range for emission from both emitter wedges as shown in Figure 3.8. Given the approximate ion distribution and emission rate calculated, a 300 ns simulation is completed, releasing 26,000 monomers, 29,000 dimers and 7,000 trimers in the first nanosecond. A single-release simulation has been chosen for ease of results analysis computationally and graphically, as a single release is enough to verify characteristics such as plume impingement, angle, and energy. Previous multi-release studies that were found to be computationally prohibitive to analyze, were observed to show similar characteristics to that of a single-release study [90].

The apex of each emitter was segmented lengthwise into 40 micron sections. In this way, emission surfaces could be selected along the edge with 120 micron spacing between each region as predicted by Wright and Wirz model, with the exception of the area where there is a dip in the normal electric field magnitude before spiking again due to edge effects. This approach enables the selection of individual emission surfaces across both emitter edges. For each emission surface designated as an 'ion inlet' boundary condition within COMSOL, the initial positions of

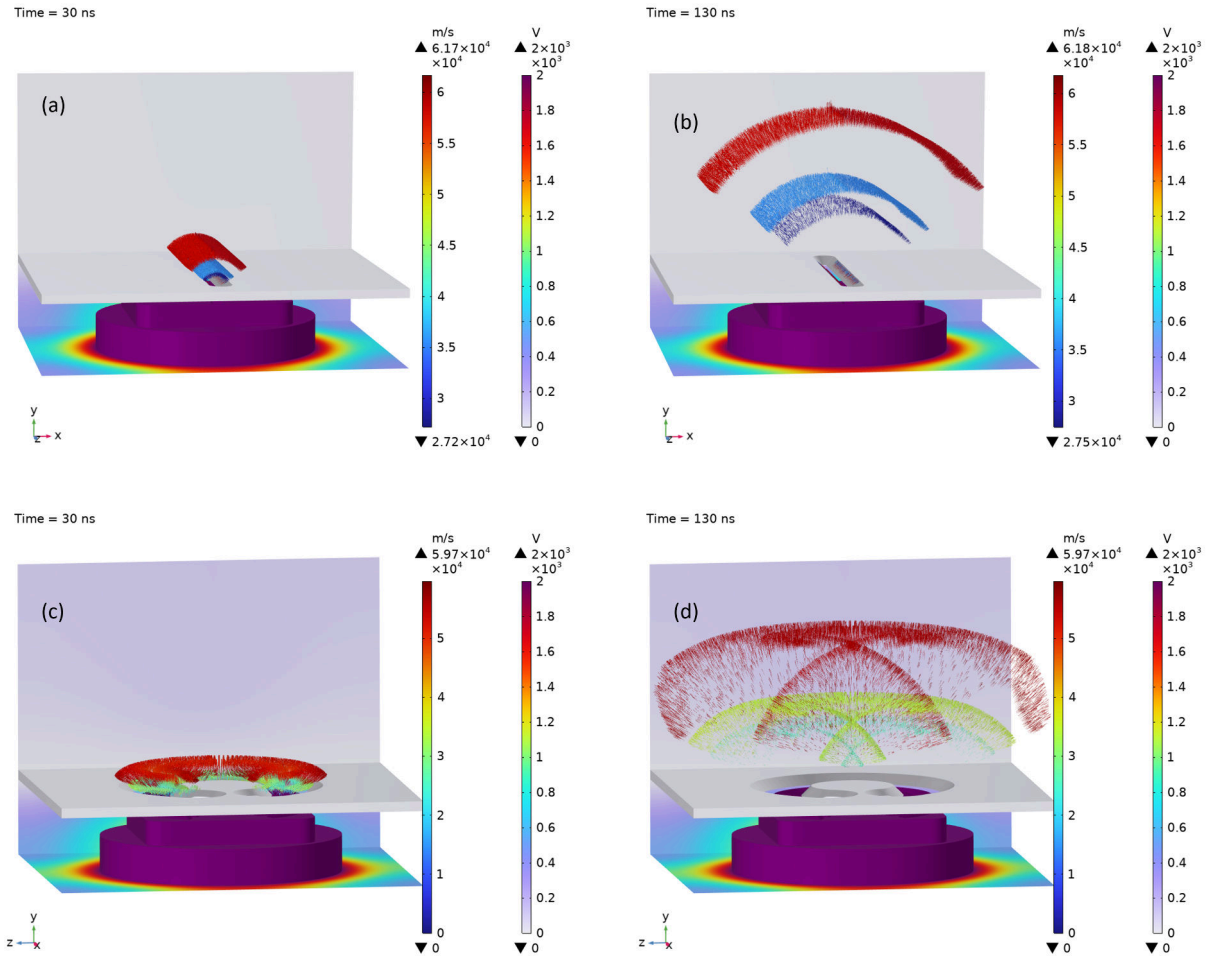

Figure 3.14: Linear and crescent emitter particle trajectories for 30 ns ((a) and (c) respectively) and 130 ns ((b) and (d) respectively) time steps. The fraction of particles rendered is 25%.

the ions were specified to be randomly distributed across the region, with zero initial velocity. The rectangular emission zones are a slight departure from real Taylor cone emission, where Taylor cone base radii have been known to be on the order of 5 micron. Breaking down the edge into boundaries smaller than 40 micron lengths was found to be computationally prohibitive when constructing the component geometry and its mesh.

Particle Trajectories for Linear and Crescent Configurations

Several particle tracing simulations were conducted while varying extractor parameters such as thickness and position. The most favourable configuration uses a 0.4 mm thick extractor electrode positioned at the same height as the emitter apex. A selection of time steps over the first 130 ns show the plume evolution for both the linear and crescent wedge configurations in Figure 3.14. In plotting the particle position and velocity magnitude, the distinctive waves of ionic clusters of differing velocity, caused by the acceleration of different masses under the same electric field are immediately apparent. For clearer visualization as well as limitations of GPU power, only 25% of the particles are rendered in figures throughout the following results.

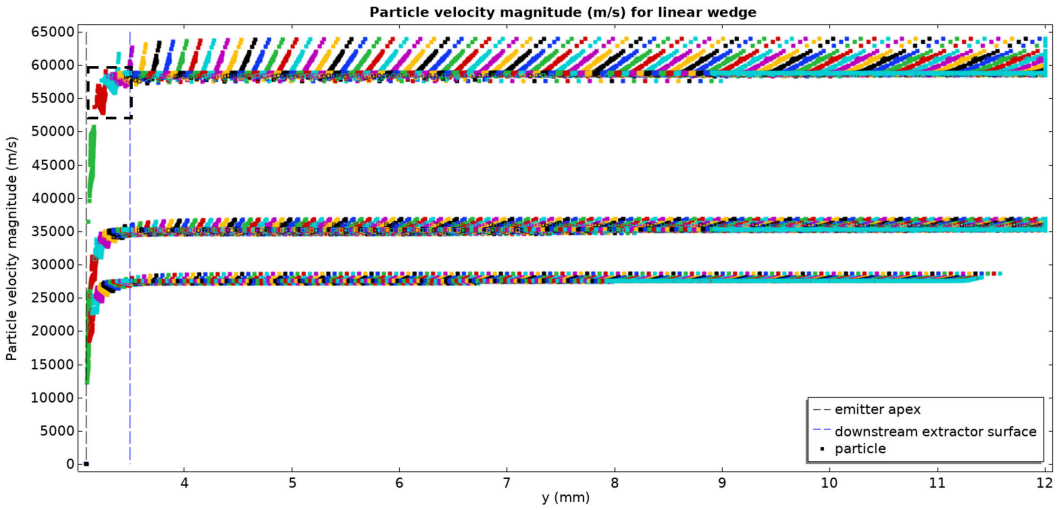

(a) Particle velocity along total thrust axis.

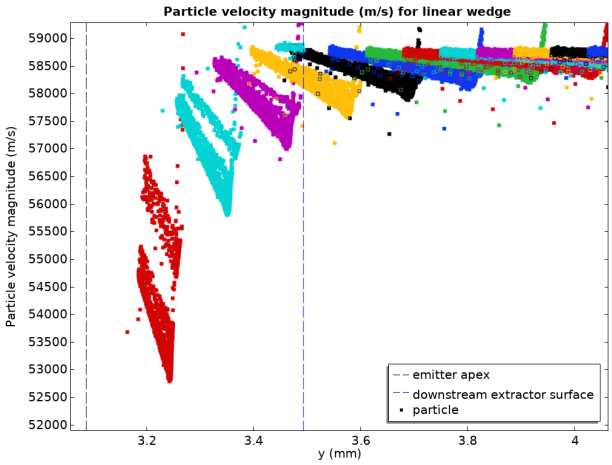

(b) Magnified view of monomer group velocities.

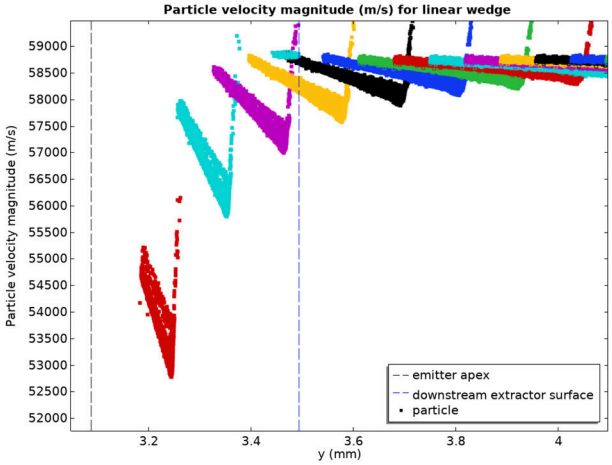

(c) Magnified view of monomer group velocities excluding emission from vertices with peak field strength.

Figure 3.15: Particle velocity magnitude along thrust axis for linear wedge configuration.

For the linear emitter, the magnitude of the particle velocities in the direction of thrust (y-axis) are plotted in Figure 3.15a. Each time step is represented as a distinct colour group of markers resulting in approximately 6000 particles per colour wave. The emitter apex and downstream extractor surface are indicated with dashed lines. It is evident that each cluster group reaches its maximum velocity shortly after leaving the extraction region situated between the emitter apex and the downstream extractor surface. These results align with what was observed by Ma in their charged particle tracing studies [90].

By magnifying Figure 3.15a to view the accelerating monomer cloud in detail, it is observed that the velocity graph shows two lines per time step - one densely populated and the other less so. The sparser line represents the faster particles that have been accelerated along the peak electric field lines previously plotted in Figure 3.15b. In a subsequent simulation, when emission surfaces at the vertex are excluded, the less populated wave is removed as shown in Figure 3.15c.

A particle is differentially accelerated depending on where the simulation randomly places it on

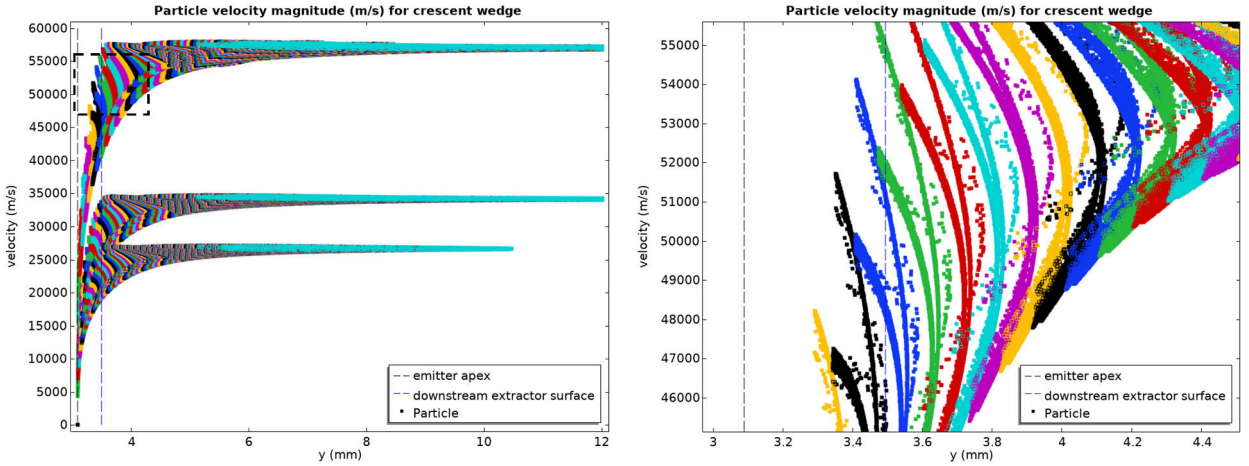

(a) Particle velocity along total thrust axis.

(b) Magnified view of monomer group velocities.

Figure 3.16: Particle velocity magnitude along thrust axis for the crescent wedge configuration.

the predefined emission surfaces. When considering that the velocity plot represents only half of the symmetric emitter, it is observed that the velocity waves are angled along the thrust axis due to the radius of curvature of the emission surface boundary on the wedge apex. This curvature extends from the bottom edge of the apex (closer to extractor) to the apex peak (adjacent to the symmetry plane). The velocity distribution is observed to narrow for each ion cluster group as they travel further along the thrust axis, converging on a velocity magnitude just below the maximum. The initially lower velocity particles reach a similar velocity over time, but are still distributed over space due to the differential acceleration experienced in the extraction region as a result of placement in the emission surface further away from the extractor.

At the right edge of each wave, a spike in velocity is observed for a small subset of particles. This outlier group is observed as a fine line of particles above each respective molecular cloud across the wedge, right on the line of symmetry. This is especially apparent at the top of the red monomer cloud in Figure 3.14b. The cause of this is likely due to meshing error and could be mitigated with a finer mesh sizing. While the monomer cloud is shown in detail in Figure 3.15b and 3.15c, the same behaviour is observed in the other molecular groups to a lesser degree.

The same exercise is performed for the crescent wedge configuration in Figure 3.16, where velocity magnitude is plotted against the thrust axis. Magnifying a selection of time steps inside the monomer portion of the plume shows two distinct velocity wave fronts and a slightly less populated wave of particles at higher velocities due to edge effects at the emitter apex termination. As expected, this is evidence of differential acceleration influenced by wedges experiencing two distinct electric field distributions across their respective apexes. Note the apparent absence of high velocity outliers at the top of each ion velocity group for the crescent wedge as compared to the linear wedge particle velocity along the total thrust axis. In the symmetric crescent wedge model, the mesh error is minimized, as no emission surface is affected by the symmetry cutoff, stopping just one 40 μm length before the axis of symmetry.

The characteristic velocity curve corresponding to each time step varies from that of the angled linear wedge velocity waves due to the fact that a fully curved apex is now included in the simulation, instead of just half in the case of the symmetric linear wedge model. Consequently, the curve becomes increasingly pronounced with each time step due to the difference in acceleration experienced by particles closest to the extractor (furthest from the apex), located at the local

Configuration			Max Plume Half-Angle [°]	Ion Cluster Impingement [%]
Case	Thickness [mm]	Offset [mm]		
(a)	0.40	0.0 height	53	0
(b)	0.40	0.3 height	51	2.4
(c)	0.40	0.6 height	47	6.9
(d)	0.63	0.0 height	54	6.6
(e)	0.40	+0.2 x-axis	53	0.3
(f)	0.40	-0.2 x-axis	52	3.4

Table 3.2: Maximum plume half-angle and impingement fraction for each crescent extractor configuration tested.

maximum electric field strength. The reduction in velocity distribution over time is much more apparent here in comparison to the linear wedge.

In taking the maximum velocities reached for each particle group, the average specific charge can be approximated to be 480,000 C/kg using Equation 2.7. Thus, the weighted average thrust and specific impulse can be approximated using Equation 2.9 and 2.10 as 100 nN and 4,550 s respectively. This value holds for both wedge configurations as each particle group is accelerating under the same potential difference, with nearly the same average exit velocity.

Crescent Extractor Configuration Sweep

Additional crescent extractor configurations tested in this study are shown in Table 3.2. These include shifting the extractor height, h, above the emitter apex to 0.3 and 0.6 mm; shifting the extractor laterally on its x axis ± 0.2 mm to simulate an out of tolerance assembly; and finally, the use of a 0.635 mm thickness, t, extractor with the upstream face at the same height as the emitter apex ($h = 0$ mm). For clarity, these configurations are also displayed in a simplified schematic in Figure 3.17. A misalignment in the $\pm$z direction was not performed as this would have affected the model symmetry.

The plume shape and impingement of these configurations are compared qualitatively at 100 ns in Figure 3.18, while their maximum plume half-angle and extractor impingement fraction are listed in Table 3.2. A 'particle-freeze' boundary condition was applied to the extractor in order to determine the number of particles impinging on it. Impingement of particles can be seen clearly

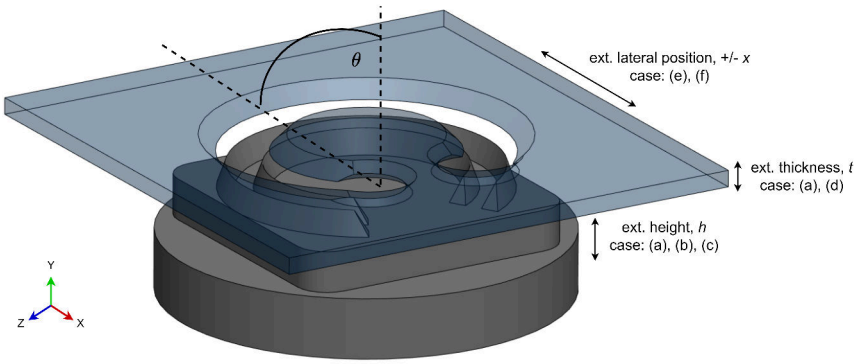

Figure 3.17: A simplified schematic demonstrating the changes made to the extractor configuration and half-angle measurement for plume expansion for each case outlined in Table 3.2. Particle tracing results for each configuration depicted in Figure 3.18

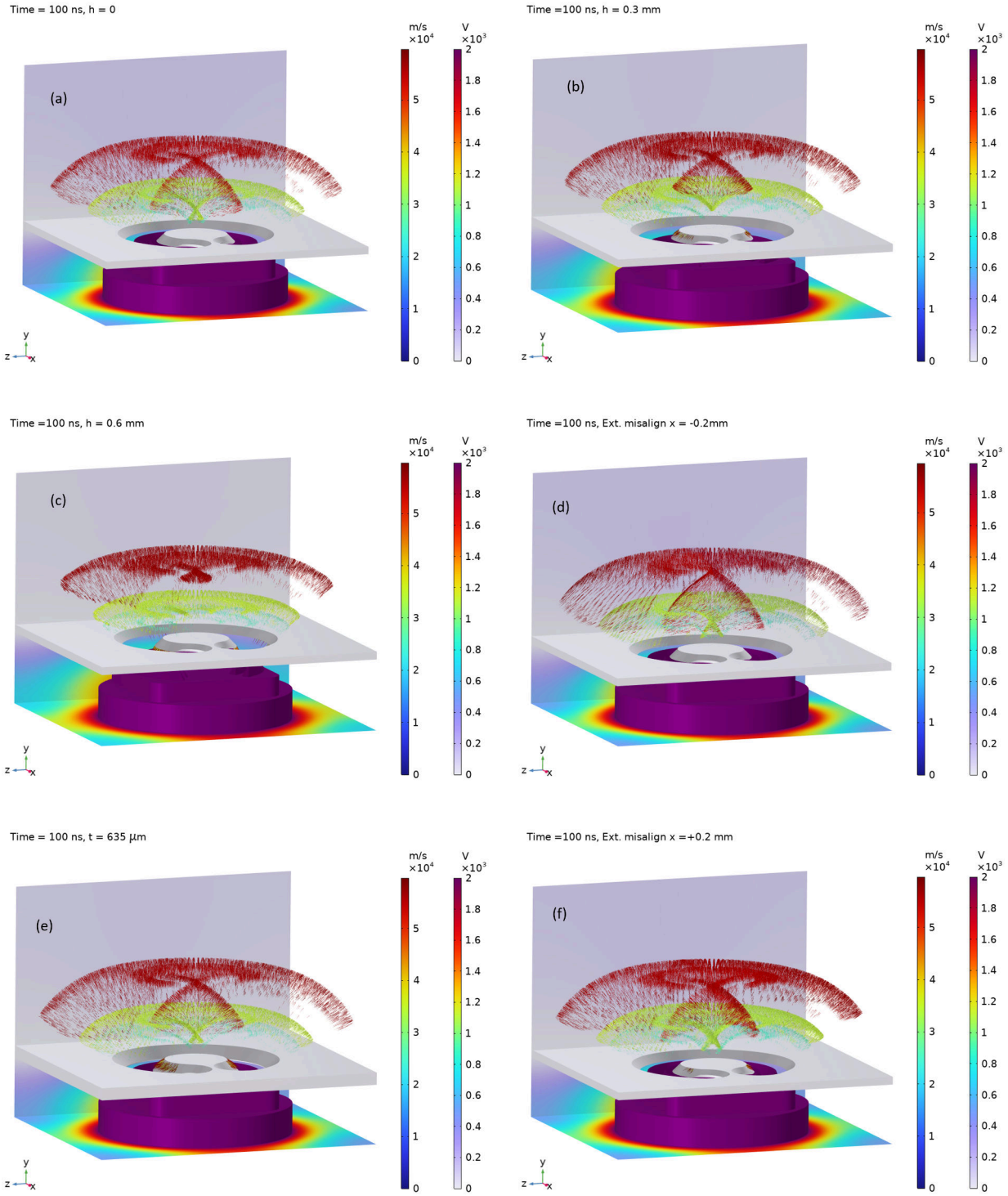

Figure 3.18: Comparison of plume shape and impingement at 100 ns for different extractor configurations varying thickness (a) and (d), height (a)-(c), and lateral offset (e) and (f) as per cases outlined in Table 3.2.

on the inner extractor in Figures 3.18b and 3.18e in particular. The fraction of particles that impinge for each configuration are plotted against time in Figure 3.19.

The plume half-angle that contains 100% of the particles at each time step in the simulation is calculated through the dot product cosine relation for the position coordinates of either the maximum x or z positions of the total population of particles. An origin point is defined at the center of the domain, positioned at the emitter wedge base at y = 2.55 mm. Of the two angles calculated for the positions of the maximum x and z vectors, the larger of the two is taken as the maximum plume half-angle relative to the emitter origin.

The plume half-angle exhibits a reduction from 53° to 47° when the emitter height is increased from level with the wedge apex to 0.6 mm above it. As previously discussed in Section 2.9.1, elevating the extractor height demonstrates a decrease in the overall plume half-angle, thereby increasing the useful axial thrust (angular efficiency). However, this also results in a higher degree of particle impingement, which in this case, increases from negligible to approximately 7%.

The plume angle predictions will serve to establish an optimal collector plate distance for experiments. To capture the maximum emitted current, a 29 mm diameter collector plate should be placed 10.5 mm away, corresponding to a 54° plume expansion. However, secondary species emission effects should be kept in mind, as a flat collector plate placed in close proximity to the thruster may reflect a substantial fraction of secondary species to the emitter, potentially introducing measurement error and propellant decomposition [84].

Extractor impingement is shown to be minimized for a 0.4 mm thickness extractor located at the same height as the emitter apex. This configuration will be targeted for fabrication and assembly. The impingement is maximized when the extractor is thicker or when the height is increased. Impingement is not visible from the view presented for the maximized height case in Figure 3.18c, as most of the ions have collided with the downstream surface of the extractor. The thicker extractor electrode experiences a significantly increased fraction of impingement than for one only 200 μm thinner, though this could be mitigated by a shallower chamfer. All values are in-line with experimental impingement current fraction measurements reported in the literature - often 10% or less [72, 76].

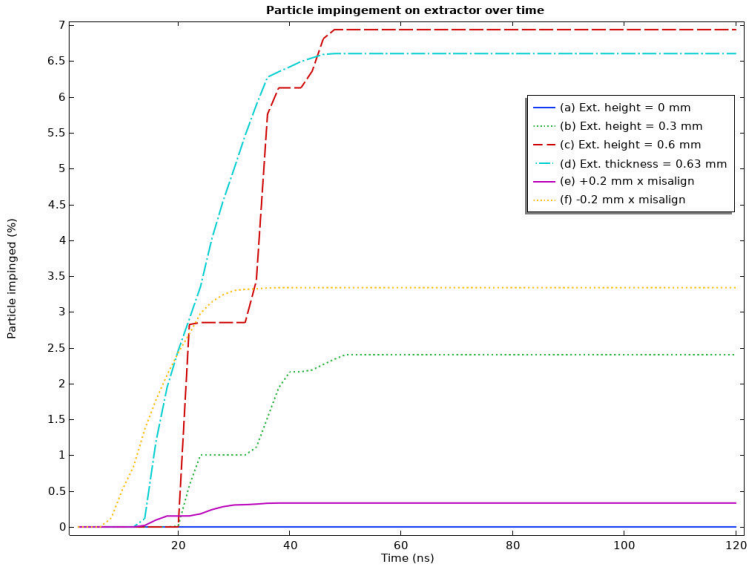

Figure 3.19: The cumulative fraction of particles impinged on various extractor electrode configurations over time for a single particle release.

As would be expected, there is substantially more impingement for a misalignment that brings the inner radius closer (+x) to the inner emitter as opposed to misalignment in the opposite direction (-x). If assembly tolerances are too large to control in the prototyping stage, it would be better to err on the side of the latter and assemble the thruster with a misalignment that tends towards the -x direction, as this would allow for increased thruster robustness. However, this may also affect the emitter's multi-onset voltage capabilities, bringing the onset voltage of the two wedges closer together and possibly blurring the line between thruster operating regimes that are intended to be distinct from one another.

In Figure 3.19, with the exception of cases (d) and (f), stepped increases in impingement can be observed relating to the movement of each ion cloud as it passes through the extractor slot over time, exhibiting the same behaviour seen in time of flight diagnostic results. A fraction representative of the total ion cluster distribution present in the plume is evident in the area under the curve of each step. The absence of a stepped curved possibly shows the capture of a deeper portion of the plume with increased extractor surface area, such as in case (d).

3.7 Concluding Remarks

The prototype design and modelling of a simple linear and multi-onset voltage crescent emitter wedges slotted into the AFET-2 inspired thruster housing architecture has been presented. It is hypothesized that, in operating a porous wedge electrospray thruster with two distinct onset voltages across its wedges, an increased throttling range may be available. Therefore, variable specific impulse operation of larger magnitude than that of throttling a singular onset voltage porous electrospray thruster may be achieved in a way that has not been previously explored in the literature. The emitter and extractor prototype is heavily informed through electrostatic and particle tracing analyses, which determined appropriate operational ranges and maximized thruster lifetime. Additionally, particle tracing studies provided insight into the evolution of the plume emanating from a novel emitter geometry.

The sensitivity of geometric parameters to onset voltage are first investigated using a 2D linear wedge. The results indicated that the extractor radius of curvature, reservoir pore diameter would have the greatest effect, followed by slot width and extractor height. Next, a 2D axisymmetric model was utilized to determine the optimal emitter extractor distances to produce distinct multi-onset voltage operation. A range was targeted for predicted onset voltages of 1750 V and 2100 V for the primary (inner) and secondary (outer) wedges respectively. Finally, 3D symmetric crescent modelling provided a target extractor-emitter assembly for the multi-onset voltage prototype which can mitigate electric field edge effects and plume impingement. Predictions for thruster operation were also obtained to be compared with experimental results.

The next chapter will focus on the fabrication work undertaken to create sharp and uniform emitters out of BSG frits using CNC micromachining practices.

4 Micromilling of Porous Glass Emitters for Electrospray Propulsion

Fabricated emitter apex geometries must be as uniform as possible, given the electrohydrodynamic instabilities associated with electrospray emission and the necessary field strength tolerances for the proposed multi-onset voltage operation. Throughout the literature, successful tests of conventionally machined porous electrospray thrusters have been reported [72, 90, 71], yet the specifics of the emitter manufacturing process are often sparse. While there is mention of CNC models, spindle speeds, and tooling diameter, crucial details that would reduce initial trial and error in manufacturing are missing. There is currently limited applicability of machined porous BSG and as a result, most research into machining strategies is protected behind proprietary commercial processes. However, extensive information on general micromilling as well its application to machining porous metals, thin features and brittle material served as valuable guidance during experimental fabrication tests.

This chapter provides an introduction to micromilling, followed by a presentation of preliminary machining validation results. Subsequent sections detail the machining process and results using a desktop micromilling CNC for optimal emitter fabrication testing. Experimental efforts to improve the uniformity and sharpness of the linear and crescent emitter apexes are presented and discussed alongside the final emitters to be utilized for ESP in the proceeding chapter.

4.1 Introduction to Micromilling

Micromilling is a specialized field of machining in which the use of small rotating cutters are advanced into a workpiece in order to remove material and form micrometric scale components. Many traditional macro-machining techniques do not scale down appropriately and must be considered during the design process. The most significant of which is due to the 'size-effect' wherein the size of the uncut chip thickness, h, and working material grain size become comparable to the cutting edge radius of the tool, r_β, as depicted in Figure 4.1. This results in a drastic increase in the shear flow stress experienced by the working material, where factors such as grain boundaries, defects, and material impurities affect the slip process during plastic deformation [139]. During conventional cutting, the tool is assumed to be perfectly sharp and material can be removed purely through shearing, F_c. However, due to the increasing influence of the size effect in microcutting, the contribution of a 'ploughing' or elastic deformation force, F_p, in which material is pushed around instead of removed, cannot be neglected, resulting in a material specific minimum uncut chip thickness h_{min}. Many key parameters must be accurately controlled during the cutting process relating to the work material, machine, and tooling. See Table 4.1 for a summary of these key aspects [139].

Micromilling machines must have high rotational (i.e. spindle) speeds, micron scale or lower

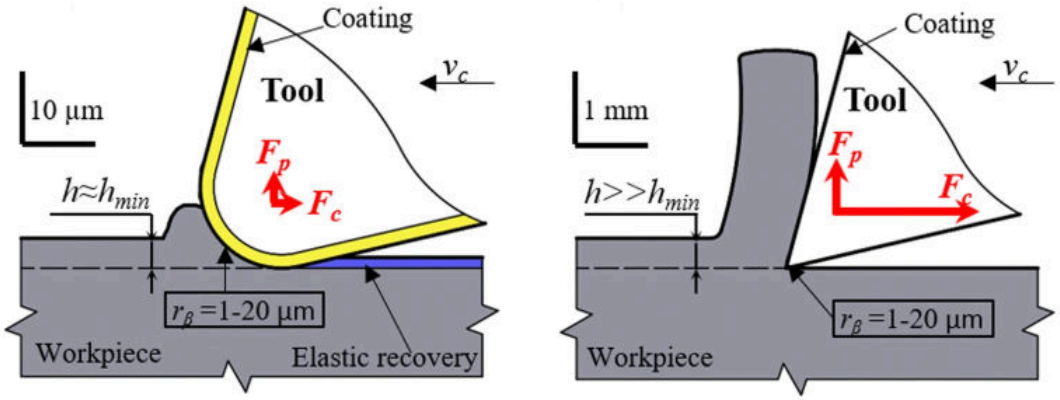

Figure 4.1: Comparison of micro- and macro-scale cutting phenomena, where the ratio of cutting to ploughing forces along the cutter direction, v_c, are significantly different. Sourced from Balazs et al. [140].

motor resolution for accuracy, thermally stable frame, and spindle stiffness to handle error such as tool deflection [139]. Spindle speeds range from 25 up to 200 kRPM on a specialized machine which are required to attain high enough cutting speeds for micromilling applications [141]. Coolant (spindle-fed or externally sprayed) is often used during the machining process to cool, lubricate and facilitate chip transport which works to improve tool life, workpiece accuracy, and final surface finish [142]. Compared to traditional milling, workpiece and tool temperatures may be considerably reduced, though thermal expansion may still result in lower finished component accuracies and must still be considered for some applications. However, due to the high heat resistance of BSG and the relatively short machining times, dissipation of process generated heat was not prioritized during experimental tests.

Tooling material commonly employed is coated tungsten carbide with 1000 down to 25 micron diameter cutter shapes. Typically, tool geometry only utilizes two flutes, although smaller diameter tooling with just one flute (spade type) is also available. While additional flutes can enhance tool durability due to increased rigidity, this comes at a cost of reduced cutting resistance, and an increased likelihood of material clogging [139]. Progressive tool wear must be carefully considered, as blunting increases the tool edge radius and increases the cutting forces experienced by the

Work Material	**Tooling**	**Machine**
Grain size	Cutter material	Spindle speed
Hardness	Sharpness (edge radius)	Spindle runout
Homogeneity	Coating	Coolant use
Defects	Batch consistency	Positioning accuracy
Impurities	Tool diameter	Response time
Elastic recovery		Stiffness
		Damping
		Thermal stability
		Error compensation

Table 4.1: Non-exhaustive list of key machining parameters that must be balanced during the milling process. Adapted from [139].

cutter, leading to less accurate machining and potential tool shaft failure.

Tool coatings, typically thin layers of a specialized metal compound ranging from 2 - 5 μm, are adhered to the tooling through vapour deposition techniques. These aim to enhance the surface properties of the substrate, consequently extending tool life and improving productivity. Common coatings such as TiN, TiAlN, and CrN can augment hardness, wettability, and resistance to corrosion and scratching. However, one must consider the effect a coating on a micromilling tool will have on increasing the edge radius, which can increase the influence of the size effect, depending on the size of the minimum uncut chip thickness for the material in question.

The uncut chip thickness, or 'chip load', is defined by the speed at which one intends to machine and the tool geometry:

$$h = \frac{FR}{RPM}(n_f) \tag{4.1}$$

where FR is the feed rate in inches per minute, RPM is the spindle speed, and n_f is the number of flutes of the tool. The desired feed rate and chip load highly influences parameters such as material removal rate, power requirements, surface finish of the part. Tool specific running parameters for common materials are provided in feeds and speeds tables provided by the tool manufacturer. A machinist may begin with these values and make adjustments based on machine response during cutting or by inspecting the accuracy of the finished part.

The machine resolution and repeatability are dependent on the accumulation of many sources of error that can occur, stemming from within the machine components, and through potential user error [141]. Table flatness in relation to the spindle must be ensured for machining accuracy. Worm screw backlash can introduce position overshoot errors when feed rates are high. User error can result when stock sizes implemented in machine programming does not match the true stock size. The largest sources of error are tool deflection and runout. Tool deflection can be mitigated by using stiff tool materials, more flutes at shorter length of cuts, and minimizing the length that the tool is extended from the collet (stick-out). Runout, the deviation from the true axis of the cutting tool, shank holder or spindle, can be mitigated through the use of high quality tooling, machines and holders.

4.1.1 Milling Techniques of Interest

In conventional or 'up' milling, the cutter rotates against the feed direction, resulting in the gradual increase of chip width from zero, as depicted in Figure 4.2a. The initial contact leads to more tool rubbing, generating additional heat that diffuses into the workpiece. Additionally, rubbing action accelerates tool wear, thereby reducing overall tool lifetime [143]. Chips are also carried forward by the tooth and if not properly evacuated, will cause re-cutting of chips, impacting surface finish. Although this approach is useful in situations where backlash between the lead screw and the nut in the machine table cannot be neglected, such as in manual milling, many modern machines can either compensate in their programming or integrate physical backlash reduction measures. In general, this is not a preferred cutting method as the cutter may lift workpiece which may cause parts to be cut out of tolerance.

Conversely, in climb or 'down' milling, as the cutter rotates with the feed direction, chip width starts with the maximum size and decreases as the flute cuts as depicted in Figure 4.2b. This facilitates heat transfer to the chip and causes less tool rubbing. Chip recutting is reduced as the chips are evacuated behind the cutter. Overall, this form of cutting is more commonly used today as cleaner cuts and surface finishes are achieved, and workholding is made simpler due to downwards forces produced by the process.

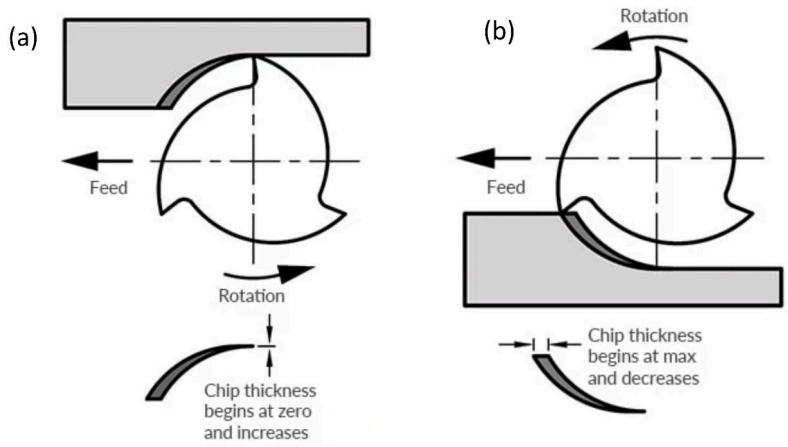

Figure 4.2: A schematic comparison of (a) conventional and (b) climb milling strategies. Sourced from [143].

Popov et al. demonstrate a variety of machining strategies for milling thin walls into brass, which will have general applications for brittle materials [144]. Their recommendations include avoiding sharp corners to prevent stress concentration, minimizing abrupt changes in cutter direction to mitigate machine backlash, and reducing axial cutting forces to minimize tool chatter and subsequent workpiece vibration. Tool chatter can be reduced through the use of conventional milling, as well as through the use of tools with zero corner radius, such as a ballnose cutter. Additionally, the tool path should be generated so that the thin features of interest are supported by the fixture or areas of the workpiece that have yet to be machined.

4.2 Porous Borosilicate Glass Characteristics

Borosilicate glass is a silica and boron trioxide glass commonly used as laboratory glassware due to its low reactivity and high resistance to thermal shock [145]. The porous subgroup is often used as a highly effective filtering substrate and catalyst support. ROBU brand stock is purchased through Adams and Chittenden as 10 mm diameter cylindrical frits with 2.7 mm ($\pm$0.25 mm) thickness. P5 (1.0 - 1.6 μm pore diameter) and P4 (10 - 16 μm) grade porosities were investigated for emitter fabrication while P0 (160 - 250 μm) to P3 (16 - 40 μm) grade porosities were used as reservoirs.

Porous BSG can be manufactured through methods such as phase separation, direct leaching and sintering [145]. ROBU utilizes a sintering process [146] similar to that described in Section 2.8.3, wherein a glass preform is heated to high temperatures over specified time periods and is subsequently treated in an acid bath to remove the soluble filler and reveal the porous silica structure. Differing pore sizes are obtained through varying the annealing conditions such as time and temperature. Although commonly assumed to be homogeneous and isotropic for analysis, the sintering process used to obtain BSG has been shown to exhibit increased anisotropy compared to that of materials such as carbon xerogel [69]. A wide pore size and position distribution may negatively affect fabrication and will make it harder to predict and control the thruster performance. This research seeks to determine optimal machining strategies to mitigate these disadvantages while benefiting from the COTS access to BSG stock.

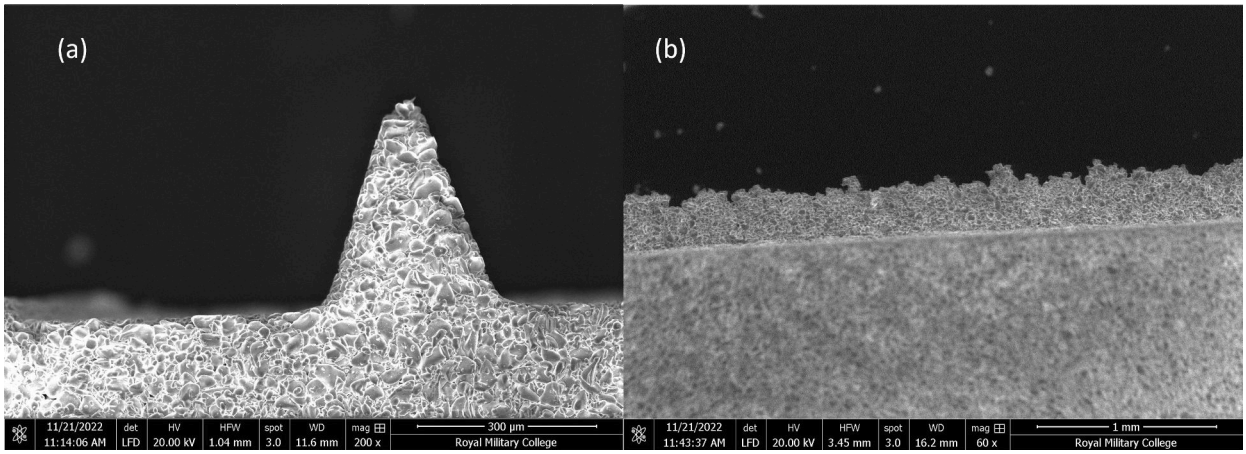

Figure 4.3: Scanning electron microscope image of the (a) front and (b) side view of a P4 grade emitter fabricated using a Haas VF-5 and a 0.015" tapered square endmill. Speed and feed: 15 kRPM, 10 in/min.

4.3 Validation Micromilling Tests: Haas VF-5

Preliminary milling tests of the linear wedge prototype were carried out using a Haas VF-5/40. The VF series machining centers are powerful and intended for production line machining of large, high hardness stock. The smallest possible motor movement was within 5 μm and spindle runout was less than 2.5 μm, however tool runout was often quite large, around 25 μm while using an ER-40 collet. The minimum spindle load was difficult to control for machining of fragile materials with small features.

Roughing work of the distal base was completed with a generic 1/8" square endmill. Prism milling was carried out using a tapered square endmill 0.015" (381 μm) in diameter and a taper of 20 degrees (Harvey Tool - 832815-C6). The maximum spindle speed of the VF-5 is 15 kRPM which was explored with feed rates of 10 and 40 in/min, and full axial depth of cut (DOC). This allowed for a single pass on either side of the prism at their full height of 500 μm for this test. Coolant was employed in initial tests for chip evacuation however it was found to obscure the view of the machining process and there was concern that excess water pressure directed at an angle approaching normal to the wedge wall would break the edge. It was also unknown how effectively the substrate could be cleansed of coolant residue. Fabricated wedges from the validation tests rarely obtained sharpness below 30 μm and had extremely poor uniformity, with heavy spalling observed along the wedge apex. While repeatability was difficult, one P4-grade emitter wedge was produced with approximately 6 μm radius of curvature (ROC) and 350 μm height as shown in Figure 4.3. Variation in wedge uniformity was calculated to be as high at 30%, where spalling as large as 100 μm are observed. However, this sample proved capable of producing stable emission of approximately 60 μA at 2300 V, therefore validating the manufacturing process. Fabrication tests continued with the acquisition of a desktop CNC machine more capable of working on small scale features.

4.4 Desktop Micromilling Tests: Penta Machine PNC V2-50

The Penta Machine Pocket NC (PNC) V2-50CHK is an accurate 5-axis desktop CNC milling machine equipped with an NR-2551 NSK spindle, capable of reaching maximum spindle speeds

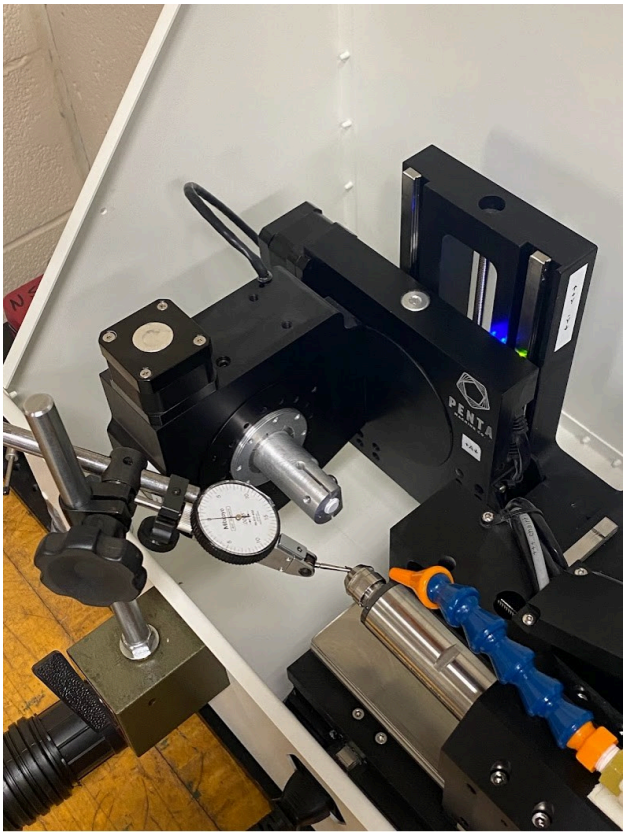

Figure 4.4: PNC V2-50 inside an enclosure mounted to a lab bench with the chip blower and vacuum outlet modifications. Indicator measuring tool runout in between tool changes with a BSG frit mounted in the fixture.

of 50 kRPM. The CHK-type collet allows for increased tool grip strength and rigidity, which maintains an extremely low runout of approximately 2.5 micron. The machine utilizes five NEMA 17 motors to drive three lead screws for XYZ movements and two rotary worm drives for controlling the A and B axis. These motors achieve 6 micron and 0.01 degrees resolution respectively with 12 micron backlash at the tool base in the XYZ axes. The PNC V2-50 model is often purchased for educational use, making it a good candidate for broadening access to academic ESP prototyping research.

During the course of fabrication tests, modifications were made to the machine to improve its performance as depicted in Figure 4.4. An air-fed chip blower was mounted to the top of the spindle, pointing directly down the length of the tool for increased chip clearance. The enclosure was bolted down to a heavy table to reduce the impact of backlash and absorb vibrations produced by the machine. It was observed in early tests that milling of P5-grade BSG produced a fine dust that was suspected to be light enough to be airborne. For user safety, and to ensure as little as possible dust settled upon the moving surfaces, a hole was cut into the enclosure directly below where a majority of chips were expected to fall. A vacuum hose was then connected and running at all times during the machining process.

A fixture inspired by the design introduced by Natisin et al. [72] was fabricated for clamping the BSG frits to be machined without damaging the material as shown in the background of Figure 4.4. A circular 6061 aluminum rod with a 10 mm diameter inset slotted through the middle can apply light radial force with screws. The rod itself is clamped by the V2-50 B table

ER40 collet. An additional benefit of using a circular fixture is the fact that the collet centres the part in the XY plane and part probing operations can be simplified. By modifying the G-Code after post processing, one can instruct the machine to full stop its operation at the intended top face of the fixture and the fixture itself can be inserted through the bottom of the B-table right up to the tool tip, effectively providing the correct coordinate system for four out of five axes (X, Y, Z, and A) to the machine in seconds without the use of probing strategies.

4.4.1 Micromilling Procedure

The general procedure for milling a BSG frit first involves measuring the frit thickness to the hundredth millimeter with calipers. Ten measurements are taken while rotating the frit and the average is input into the stock dimension in the computer aided manufacturing (CAM) software. In this work, Fusion 360 is used to generate tool paths and G-code to be uploaded to the V2-50. There is no filleted apex radius specified in the CAD model inserted into the CAD to aim for the sharpest possible configuration. The Penta simulator is used to verify the G-code generated is correct as well as modify the code to implement the fixture setting process as previously discussed. Tool sharpness is inspected under a microscope by comparing the tool to be used to a new, unused tool. Before each tool is used, the machine automatically probes the tool to determine the tool length offset. Tool runout was periodically measured with an indicator as demonstrated in Figure 4.4 and was always measured to be below the indicator resolution of 0.0005" (13 μm).

The initial frit roughing consists of running a 1/8" square endmill at 50 kRPM with a feed rate 5 in/min. A face mill toolpath removes 25 μm from the frit surface to ensure flatness, followed by milling out the distal base and the roughing of the wedge design to be attempted. For example, roughing the linear wedge would leave behind a 600 μm rectangular prism, to be finished by a smaller tool. During finishing passes with a smaller tool, the machining parameters (i.e. feed rate, spindle speed, depths of cut) are varied over the course of the tests to determine optimal cutting strategies. After milling is completed, the frit is placed in an isopropyl alcohol bath in an ultrasonic cleanser for 10 minutes and the V2-50 is wiped down with special attention paid to the sliding surfaces in order to not damage or degrade them with fine glass particulate waste. A selection of emitter apexes were blunted by hand to investigate the mitigation of electric field effects. Specifically, a pair of tweezers wrapped in a kimwipe were used to scrape away the sharp edge under a microscope.

Emitter images are taken with a scanning electron microscope (SEM) and a standard optical stereo microscope with subsequent extended depth of field and post-processing analysis by the microscope camera software ToupView and ImageJ. The Kappa plugin for ImageJ is used for radius of curvature analysis.

Over the course of the fabrication run, milling parameterization was performed on an ad-hoc basis due to a relatively low supply of BSG. Subsequent tests were modified based on feedback from immediate results rather than through factorial experimentation (e.g. Taguchi orthogonal array [147]) typically found within micromilling research. Future work should look to adapt such testing methods to validate these results.

Multiple emitter heights were attempted over the course of testing, varying from 500 to 800 μm. As results improved, larger wedges were fabricated with the intention of mitigating shielding effects and to correct for smaller than designed wedge heights as a result of machining error.

To complete the finishing passes, several Harvey Tool 832815-C6 tapered square endmills were used for a majority of the testing. This is a 3 flute, AlTiN-coated carbide tool with a 0.015" diameter and a 20 degree square taper. The taper was chosen to produce a steep wedge angle for a modest aspect ratio prism while only requiring to cut directly downwards to the piece. A

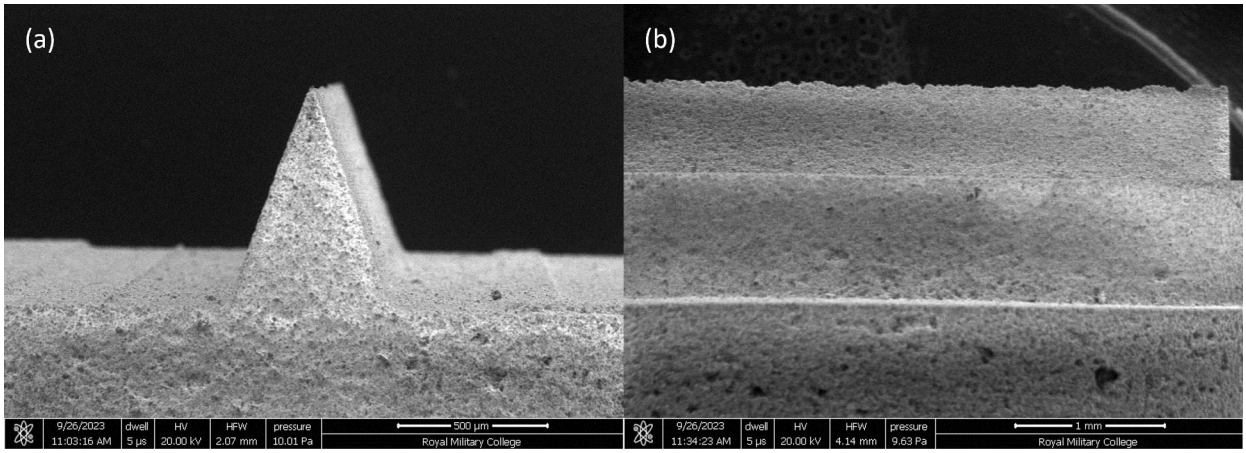

Figure 4.5: SEM image of the (a) front and (b) side view of a P5-grade emitter fabricated using a PNC V2-50 after the addition of a blower system and application of up milling strategies. Tapered 0.015" diameter square endmill. Speed and feed: 50 kRPM, 1 in/min.

coated tool was chosen in an attempt to increase tool life, due to its increased hardness. Using SEM analysis, the typical tool cutting radius was determined to be approximately 0.35 μm.

Spindle speed was directed at a constant 50 kRPM throughout testing, while feed rates of 0.25, 0.5, 1, 5 and 10 in/min were explored. The was varied from full axial depth of cut (500 to 800 μm depending on emitter height chosen), to as low as 75 μm per stepdown. The radial depth of cut (DOC) was kept below 50 μm where possible, but in some cases larger cuts were forced where tool access was constrained. For example, the pitch between the crescent emitter prisms was only 50 μm larger than the diameter of the tool, requiring one large stepover pass for the inside prism, and a regular 50 μm radial DOC for the inner wall of the outer emitter.

4.4.2 Emitter Fabrication Results

Following the installation of a chip blower system to the V2-50, apex uniformity improved remarkably. The blower effectively eliminates any material obstructing the tool path, substantially reducing the risk of chip recutting. Furthermore, the use of up milling strategies, was also determined to reduce the frequency of spalling along the apex of both linear and crescent wedges. It is hypothesized that up milling strategies reduce vibrations through flute rubbing on the material initially through its revolution instead of a jarring, relatively thicker cut. Additionally, this approach directs cutting forces upwards and not into the workpiece, possibly producing less vibration. Flute rubbing is not an issue for borosilicate glass (BSG) as excess radial force is not required for brittle material. The weaknesses of up milling are mitigated through improved chip evacuation and the fact that surface finish of the wedge walls is not a priority. This is exemplified in Figure 4.5, where a P5-grade linear wedge 710 μm height and 1 μm ROC linear wedge has been successfully fabricated. Spalling intensity is demonstrated to have been considerably reduced, as the wedge height never drops below 6% of the maximum height.

In terms of feed rate and cutting depth, it was determined that the optimal results for achieving sharpness in P5-grade emitters were obtained at 1 in/min with full depths of cut. This may be due to subjecting the workpiece to as little vibrations as possible, while maintaining smooth machine tool paths, that do not shock the part. For contrast, directing a 0.25 in/min feed rate and 0.003" axial DOC, extended the machining time of a crescent wedge emitter to longer than one hour while a similar program with 10 in/min feed rate and full depth of cut would have completed the part

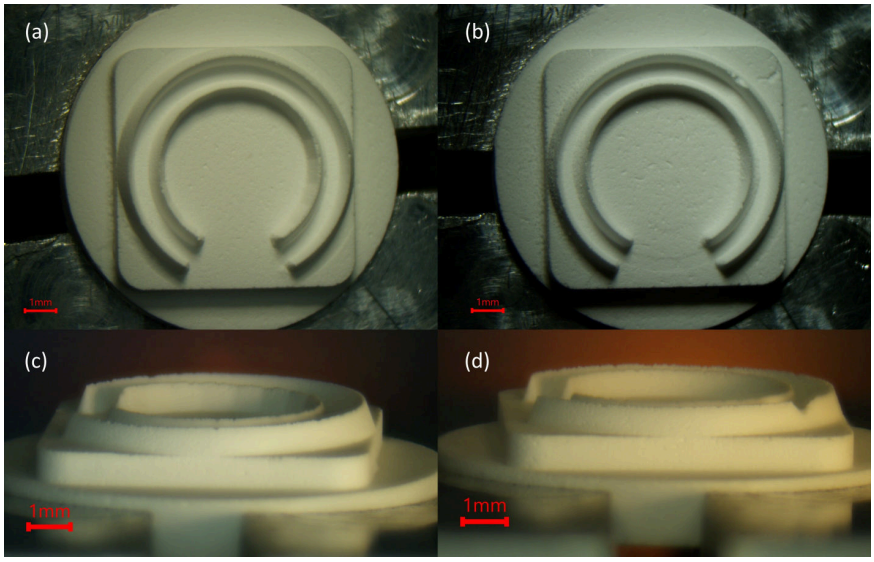

Figure 4.6: Visual comparison using top and side views for two tests with differing axial depths of cut. Test in (a) and (c), used a full axial DOC whereas the test shown in (b) and (d) used 75 μm. Parameters: P5-grade BSG, 50 kRPM, 0.5 in/min, down milling strategy.

in under 5 minutes. A comparison is provided for two P5-grade crescent emitters in Figure 4.6. During extended periods of machining, the part is contacted by the tool for a significant fraction of this period. Consistent vibrational stress may play a role in reducing the bonded strength of sintered particles located across the wedge apex. However, this raises concerns about whether or not such emitters would survive the vibrational stresses associated with launch-to-orbit and requires further investigation.

Interestingly, tool life was observed to be longer than initially expected. It is possible that the AlTiN tool coating contributed to an extended tool life, albeit temporarily, as it was observed to be gradually rubbed away on each flute. Courtney et al. point out that their tool needed to be changed for every emitter milled, or approximately every 27 passes, 7 mm in length for their 9 wedge linear emitter [71]. In this research, two separate tools were used over the course of 20 separate tests, with the majority (13) having been machined by the first tool. In the center of the crescent wedge emitters, a substantial amount of material had to be removed by the tapered square endmill which could not be reached by other tooling. Although the reported tool life differs significantly, there are many other variables that could explain the disparity such as tooling quality, and the machine's power and accuracy. Later in the fabrication tests when the optimal feeds and speeds had been determined, a new tool was used, and the difference in apex quality from a well-used tool was almost negligible.

Measured emitter heights consistently fell short of the programmed dimension, measuring 50 to 100 micron smaller than intended. The exact cause for why this occurred was never determined, though it is hypothesized that the machine motor resolution was not fine enough and could have over-cut during programmed stepovers. Additionally, random massive spalling was found to occur even when a brand new tool was used. This is likely due to substrate inhomogeneity contributing to structural weakness seen clearly in areas such as at the square base where relatively large void spaces are observed. Figure 4.6 provides examples this phenomena, as the top views show void spaces on the distal base much larger than the expected pore sizes for a P5-grade substrate. This presents another possible reason for apex non-uniformity, in addition to the possibility that excess

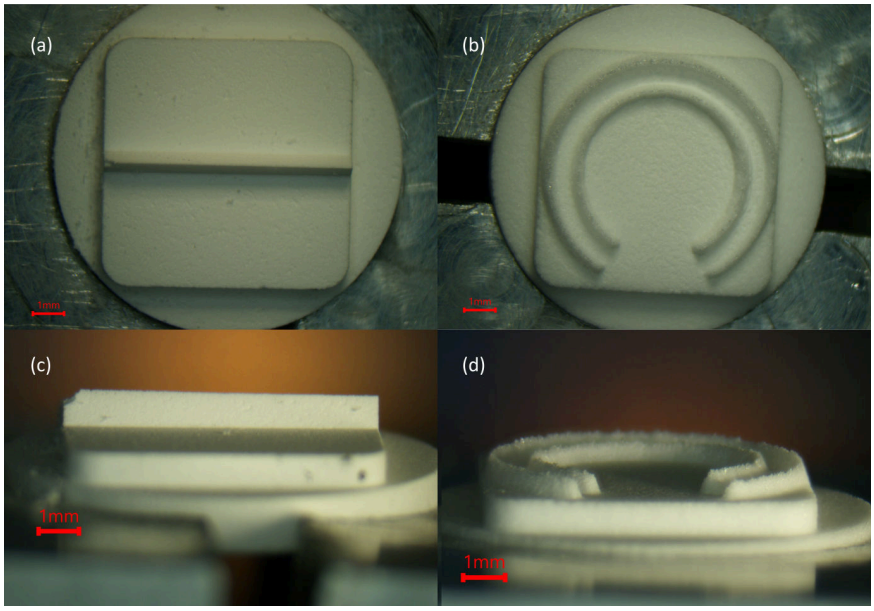

Figure 4.7: Front and side views for P5-grade linear and P4-grade crescent wedge emitters that were selected for testing.

vibrations may be causing the damage.

For more complex emitter shapes such as the crescent wedge, it was determined that specifying toolpaths that make use of arc movements using G2 or G3 machine code, as opposed to using G1 linear interpolation movements, significantly influenced the wedge wall surface finish. During linear interpolation, the toolpath only approximates the crescent with many linear points. This generates a jerky toolpath which results in visual facets along the wedge wall as depicted in Figure 4.6c. Increasing the tolerance, or the number of points generated along the interpolated arc only served to create more facets. In the worst case, data starving can occur, where a significant amount of short line moves can force the processing rate above what the controller can handle resulting in physical machine stutter while it waits for the next servo command. In contrast, specifying a G2 clockwise arc generates a minimal amount of data points, resulting in a smoother tool path that reduces overall workpiece vibrations and succeeded in removing wedge wall facets.

The machining of P4-grade emitters using the same CAD model were not as successful in generating sharp and uniform emitter apexes. Larger particle sizing was more conducive to spalling across the wedge apex. However, the intensity of spalling for final emitters was lower than for those produced using the Haas VF-5, on average only 20% of the maximum height. Edge sharpness is also limited to particle size. Alternative CAD models were developed where a larger apex radius was specified in an attempt to trade off edge sharpness for uniformity. A tilted axis finishing pass was programmed with a Harvey Tool 24610, 0.010" diameter, ballnose uncoated carbide tool with four flutes. However, due to issues related to variable final physical emitter height as previously discussed, the cutter would often end up cutting air where the program expected material.

Scanning electron microscope (SEM) analysis of select emitters showed no evidence of pore closure as a result of the machining process. The radius of curvature of both crescent and linear wedges was measured to be consistently below 5 μm. Optimal wedge uniformity was more difficult to achieve but was observed in some cases such as the linear wedge shown in Figure 4.7 and the crescent wedge shown in Figure 4.6a. These emitters were the first to be tested for emission, followed by less uniform

Targeting sharper emitter wedges than what has been attempted here for both P4 and P5 grade BSG are likely to achieve diminishing returns. Such wedges are likely to be more fragile, and the frequency of spalling will increase as sharpness reduces to the same magnitude as substrate particle size. A larger wedge with lower sharpness similar to that of Ma et al. may be preferable for space rated applications [90]. At the cost of a higher onset voltage, increased apex uniformity is likely easier to achieve when spalling creates holes that are negligible in size to the overall apex. Additionally, a larger wedge is likely to be more resistant to vibrational stresses.

While many of the sharp emitters machined here are expected to be extremely fragile and thus not resistant to vibration stresses induced during a launch event, it is possible that a custom vibration-absorbing mechanism could be integrated into the thruster design to help mitigate these concerns. If the use of BSG as an emitter substrate is to continue, the sourcing of higher quality, homogeneous material produced by alternative means such as phase-separation should be investigated. Production using this method has been shown to have a much smaller pore size distribution and better processability to avoid particle spalling experienced during testing [148]. Finally, it is worth noting that despite the use of a 5-axis machine in this work, only 3-axis milling patterns have been described thus far. This demonstrates that a wider range of CNC machines may be used to mill emitters and suggests possibilities for further optimization of the presented work using 5-axis milling strategies.

4.5 Concluding Remarks

Micromilling and its application to production of porous BSG emitter wedges for electrospray propulsion has been discussed. Machining parameters were varied over the course of testing to determine optimal milling strategies for producing sharp and uniform emitter wedges. It was determined that up-milling strategies, feed rates in the range of 0.5 to 1 in/min and full depths of cut were optimal for cutting P5-grade BSG into sub-mm linear and crescent wedge shapes with approximately 1 μm radius of curvature and apex height uniformity within 6%. In addition, effective chip evacuation and proper consideration of the toolpath generation method aided in achieving greater rates of apex uniformity.

The next chapter will present the experimental preparation, assembly, testing, and results for the linear and crescent wedge emitters manufactured using the milling techniques described in Chapter 4.

5 Results for the Linear and Crescent Wedge Emitter Prototypes

A selection of emitters with characteristics targeting sharpness and uniformity were fabricated, assembled, and tested for electrospray emission at the Royal Military College Advanced Propulsion and Plasma Exploration Laboratory (RAPPEL). While estimates of both linear and crescent wedge emitter performance are contrasted, the purpose of the experimental campaign is to observe evidence of the multi-onset voltage behaviour for the crescent configuration. The vacuum chamber system, thruster mount and diagnostic assembly are described, followed by discussions of the results for the testing of the linear and crescent wedge emitter ESP prototypes.

5.1 Experimental Process and Data Acquisition System

The RAPPEL vacuum chamber used to simulate low pressure levels consists of a Kurt J. Lesker Company (KJLC) Bell jar and an eight port service well. Achieving high vacuum conditions involves a two-stage process utilizing three pumps. The process is summarized in Table 5.1 and on the right-hand side of Figure 5.1.

Inside the the chamber, the thruster is mounted on an aluminum fin with a PEEK spacer to insulate the high voltage feedthrough from the grounded chamber. Aluminum mounting rods serve to secure the fin, as well as the collector plate and its associated components, as depicted in Figure 5.2. To measure the full plume, the stainless steel collector plate is placed 50 mm downstream from the thruster base. From simulation results discussed in Section 3.6.2, this distance will not capture the full beam angle, as an increased distance was required to fit diagnostic components, ensure visual feedback is available during experiments (e.g. glow discharge, sparking, etc.), and mitigate SSE effects [84]. The 29 mm diameter plate is mounted on an insulating PEEK base which is fixed to the mounting rods with set screws.

Upstream of the collector plate, a secondary species emission (SSE) suppression grid biased to -30 V is used to mitigate SSE as discussed in Section 2.9.1. A PEEK frame with screws and

Vacuum condition	Equipment
Medium (∼10 Pa)	Edwards Vacuum XDS10 dry scroll roughing pump, GLD-136A rotary vane oil pump, Superbee CVM201 Pirani pressure gauge (down to 1 Pa)
High (∼5 mPa)	Leybold TURBOVAC 90i, KJLC 354 series hot cathode ionization gauge

Table 5.1: Equipment used to achieve high vacuum conditions for thruster testing.

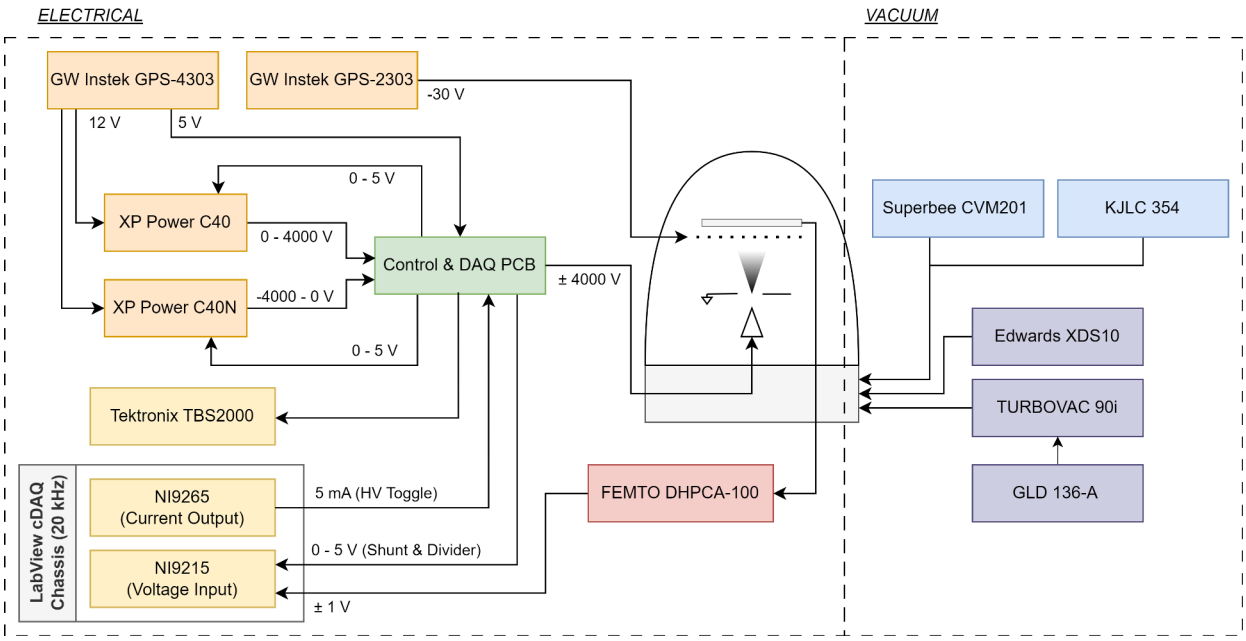

Figure 5.1: A schematic of electrical and vacuum system used to operate and acquire electrospray emission data.

Kapton tape is used to fix an MN8 nickel mesh procured from Precision Eforming. The mesh is 90% transparent with 43 μm thickness wires at 30 lines per inch, allowing for 803 μm gap widths.

To power the thruster and diagnostics, two power supplies (PS) were required for three separate inputs. A GW Instek GPS-4303 provided 5 V to the custom electrospray control and data acquisition (CDAQ) printed circuit board and 12 V to the dual XP Power/EMCO C40/N DC-DC converters. A GW Instek GPS-2303 was used to supply -30 V to the SSE suppression grid.

The XP-Power C40/N DC-DC converters and custom CDAQ circuit board used to directly power and control the thruster are briefly detailed below, while a schematic is provided in the left-hand side of Figure 5.1. The CDAQ hardware design and its associated LabView program are comprehensively discussed in Appendix A. A key requirement for the system was resilience, which needed to encompass a broad voltage range to accommodate the operation of both the linear and crescent wedge emitter prototypes. The HV DC-DC converters output up to 250 μA under full

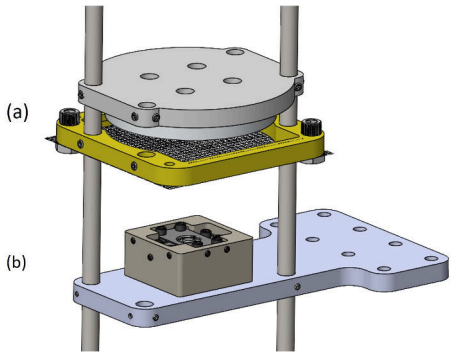

Figure 5.2: Model of test stand to be mounted within the vacuum chamber including (a) the plume collector plate and secondary species suppression grid and (b) the thruster and mounting fin.

load at 0 to 4 kV using a 0 to 5 V command supplied by the LabView program. A constant HV is output to the board connected with coaxial cables using safe for high voltage connections. A set of HVM OPTO-150 photo detector diode optocouplers rated for 15 kV reverse voltage block signal throughput until toggled by LabView. During testing, the optocouplers are be toggled at 0.33 Hz, which applies a square wave ±HV to the thruster to demonstrate bipolar emission.

Before connecting to a high voltage vacuum interface port, a set of shunt and voltage divider resistors measures the current and voltage applied to the thruster. They are appropriately sized to provide a ± 200 mV drop to be measured by a set of AVAGO HCPL-7510 isolation amplifiers. The amplifiers provide optical isolation to protect the DAQ components and output 0 to 5 V to LabView. A FEMTO DHPCA-100 high speed variable gain current amplifier senses the current impinging upon the collector plate and is capable of a gain of 10^3 to 10^8 V/A. LabView samples each of these signals at 20 kHz and displays a decimated data set to the front panel for live control while saving the raw data in the background. A low-pass butterworth filter is applied during post-processing to reduce noise.

5.2 Thruster Preparation Before Experiment

The vacuum chamber and thruster components are first wiped down with isopropyl alcohol to remove any contaminants that may volatilize as the pressure is lowered and slow the pumping process. EMI-BF_4 acquired from Sigma-Aldrich is placed in a 500 mL beaker under medium vacuum for one hour to remove any water and air that may have dissolved in the propellant. The emitter and reservoir is then immersed in the propellant and placed under medium vacuum for another hour to allow for the propellant to fully infiltrate the BSG. Care was taken to slowly decrease pressure, as pulling vacuum down too quickly would cause entrapped air to violently evacuate from the pores and push the emitter. In some cases, the emitter would flip over and bounce in the beaker, possibly causing damage to the wedges.

After the thruster is assembled, any excess propellant is dabbed from the emitter placed in the propellant housing in order to reduce the thickness of the outer liquid film and increase surface transport resistance [91]. After placement within the thruster housing, the extractor is finely aligned in each plane under an OMAX stereomicroscope using each set screw to shift its position. Once contacted on all four sides, the set screws provide a weak fixture and the extractor is subsequently locked into place with fastening screws, one of which entails a wired connection used to ground the extractor electrode to the vacuum chamber. The propellant housing height set screws are adjusted to set the desired emitter-extractor distance.

To determine the approximate volume of propellant absorbed by the reservoir (P0) and emitter (P5), the dry and wet weight of the propellant housing are compared. For the linear wedge emitter, these are 2.826 and 3.039 g respectively, resulting in an estimated absorbed propellant weight of 0.213 g. This corresponds to 0.165 mL of EMI-BF_4 propellant, given a density of 1.294 g/mL at 25 °C. The total thruster dry weight was measured to be 21.40 g.

5.3 Linear Wedge Emitter Results

A P5-grade linear wedge emitter with a P0 reservoir was tested to validate experimental diagnostics and establish a baseline measurement for the crescent emitter prototype. One kilovolt was applied to begin testing and was increased in 10 or 50 V increments every 5 to 10 seconds. Notably, there was considerable variability in the onset voltage and emitted current across tests, even with emitters of similar porosity grades, reflecting differences in emitter quality and overall thruster assembly.

The distance from the emitter tips to the extractor, estimated under a microscope, varied between 100 to 200 μm for each test. The onset voltage in most cases was found to be within $\pm$1700 to 2200 V. For a more consistent comparison of characteristic current-voltage response curves, the applied voltage was non-dimensionalized by the onset voltage:

$$u = \frac{V}{V_0} \tag{5.1}$$

First, the suppression grid was verified as working as intended at -30 V, effectively reducing the exaggerated positive emission current measurement and indicating a shift towards symmetric emitted current magnitudes as discussed in Section 2.9.1. When a stable bipolar operating point was identified at $\pm$2200 V (u = 1.1) for this assembly, a 30 minute emission test was performed to study short term emission stability. The emitted current was measured to be approximately even between both polarities, at +3.9/-4.0 $\pm$0.4 μA, with minimal variation observed over the duration of the test. The time series results of this test are plotted in Figure 5.3a. A closer look at a section of the test which includes the shunt current is magnified in Figure 5.3b. Notably, there are substantial shunt current spikes observed at the beginning of each high voltage toggle which more than double the baseline shunt current. As these spikes do not correlate with collector

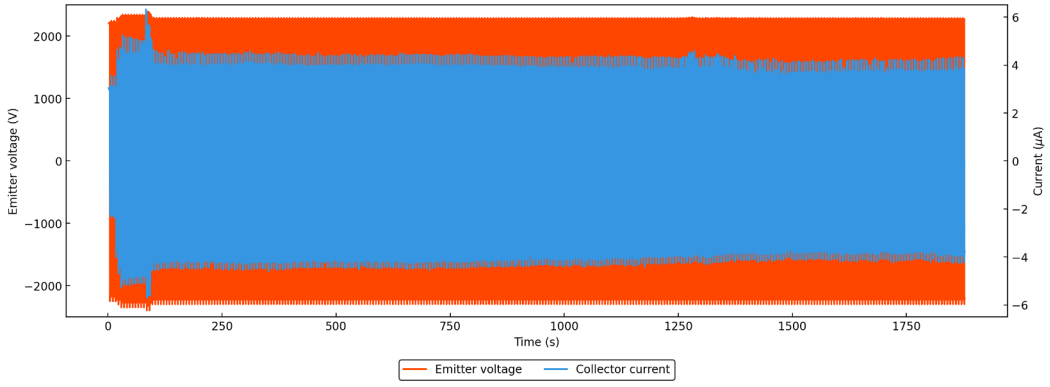

(a) Full 30 minute time series results for the stable bipolar test.

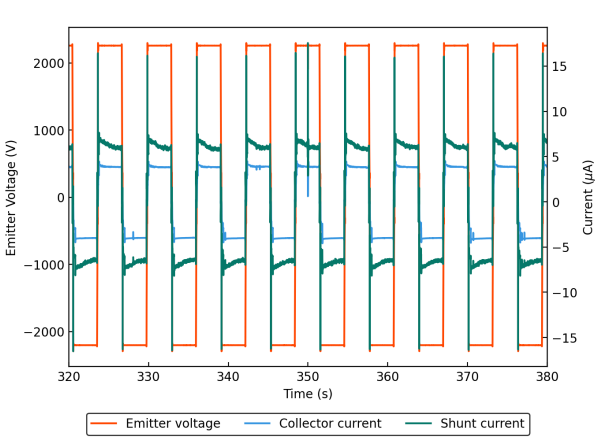

(b) Sixty second section including shunt current measurement.

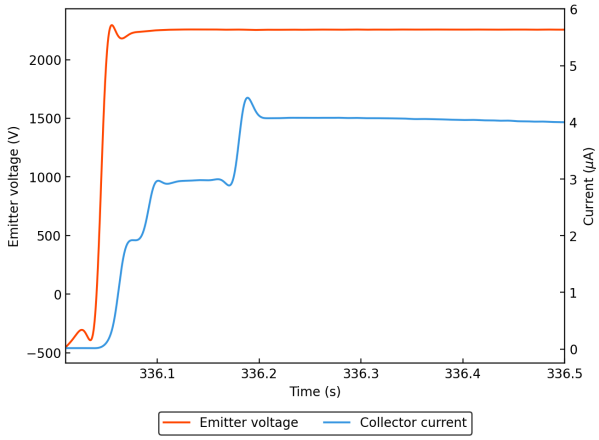

(c) The beginning of a positive emission cycle exhibiting transient current emission over a short time period.

Figure 5.3: Time series results and associated points of interest of a 30 minute stable bipolar test for a P5-grade linear emitter with a P0-grade reservoir.

current variations, they suggest a potential link to capacitance downstream of the control and DAQ PCB that may not have been entirely eliminated. The inrush current spike occurs whenever the HV is toggled from zero or from one polarity to the other, and was not observed to be present when commanding HV increases of 500+ V while operating in the same polarity. The steps taken to investigate and mitigate the capacitance are discussed in Appendix A. Presently, filtering the shunt spikes from the data is necessary for a more accurate estimation of thruster efficiency at low currents.

Transient current effects as discussed in-depth by Wright and Wirz [94] can be observed clearly in each cycle. Figure 5.3c depicts this phenomena in detail as the current initially spikes and settles over 20 ms. Notably, an initial plateau is observed in the current emitted before reaching its full output for the commanded voltage, which has not been observed in their experiments but a similar curve is observed in the work of Huang et al. which is attributed to the onset of two or more emission sites on different timescales, possibly due to tip nonuniformity [87]. The total rise time measured from zero emitted current to its settled state is observed to be approximately 150 ms.

The comparison between the measured shunt current and the collector current provides a rough estimate of the transmission efficiency, η_{tr}. If ideal emission is assumed with no impingement or charge loss due to in-flight molecular interactions, and 100% of the plume impacts the collector plate, the shunt current would match the collector current. In the case of Figure 5.3b, the transmission efficiency is approximately 67%, while also keeping in mind that up to 10% of the plume density may not reach the collector plate due to impingement on the suppression grid mesh.

In subsequent tests, the linear wedge was driven far beyond its onset voltage to characterize the current response to applied voltage. An example of time series results a bipolar test are plotted in Figure 5.4. The emitter's onset voltage was approximately ±2000 V with an emission current of approximately 1.5 and -1.25 μA and was tested as far as ±2650 V ($u = 1.32$). Averaged over each cycle, the corresponding maximum emitted currents were approximately 20.7 (±6.7) and -25.5 (±1.9) μA. At emission onset, the efficiency was 67%, and by test termination, it was 71%. The current-voltage characteristic curve commonly explored in ESP literature is shown in Figure 5.5. Emission from the same P5 grade linear wedge is compared with a P0 and P3 reservoir. For all results, each point is an average of 3 seconds of emission, or the bipolar operation period, with error bars indicating the standard deviation from the calculated mean.

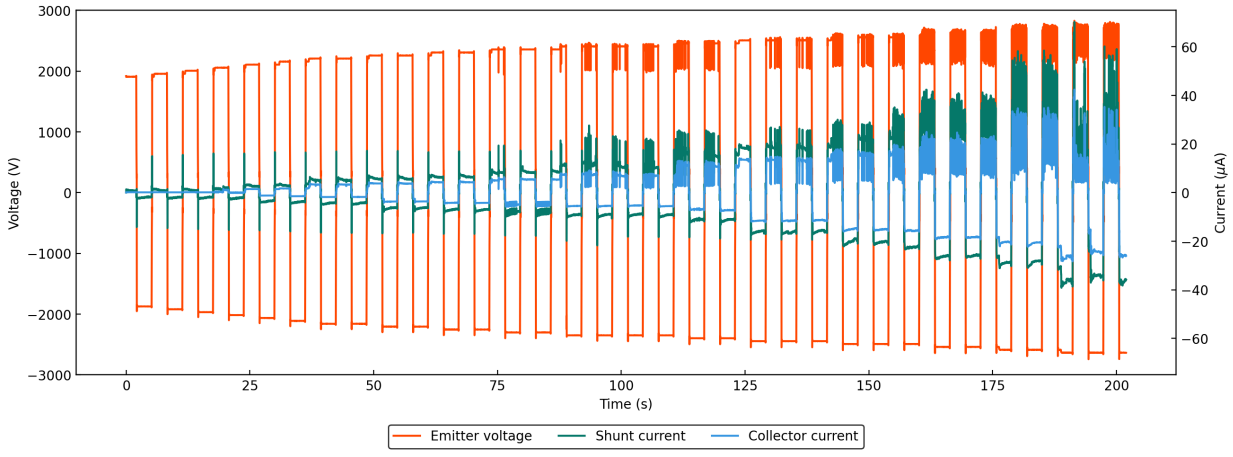

Figure 5.4: Time series results for a P5-grade linear emitter characteristic I-V response test. The reservoir is P0-grade BSG.

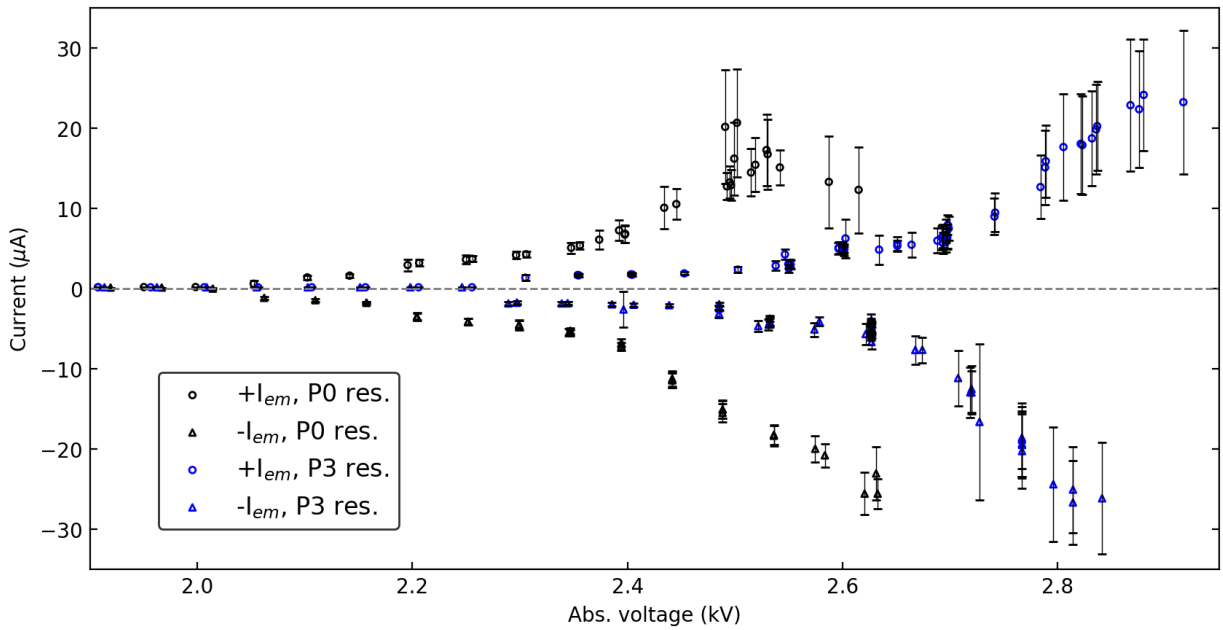

Figure 5.5: Comparison of the characteristic I-V response curve for a P5-grade linear emitter bipolar voltage test with a P0-grade reservoir and a P3-grade reservoir.

As expected, the emission noise and instability increases with voltage, where the emitter shows difficulty maintaining a constant current output. This behaviour is also exhibited clearly in a unipolar test, where negative emission current increases in a stepwise fashion shortly after onset but quickly becomes unstable after approximately -2300 V ($u = 1.21$). The time series plot of a unipolar test is shown in Figure 5.6a. Note the absence of inrush current spiking when testing in this format.

At larger voltage magnitudes, sparking events from the emitter to the extractor electrode became an issue, causing massive voltage drops leading to a temporary loss of emission. The sparking events were visually verified by observing the thruster in operation under vacuum. While sparking events were noted in both positive and negative polarities, they were notably more frequent in the positive polarity, significantly restricting the operational maximum voltage of the thruster. A wide operational range is crucial for demonstrating a multi-onset voltage emitter prototype in the crescent emitter trials. The sparking can be observed in the data as large blocks of noise at the high end of the applied voltage in Figure 5.4 and as short drops before ramping up quickly in a unipolar operation test plotted in Figure 5.6a. While both polarities are tested under voltage ranges that eventually reach instability, emission stability under the negative polarity is maintained for a wider range, up to approximately -2500 V, before the first sparking events are encountered alongside increased emission noise. In contrast, positive polarity sparking events are first encountered at approximately 2100 V which quickly increase in frequency to the point where emission current is masked at 2300 V. A closer look at a sparking event in the negative and positive polarity is given in Figure 5.6b and 5.6c respectively. Note the lag in time between the voltage drop and the corresponding inrush current spike.

In their investigation of emission from nonuniform emitters, Chen et al. discuss issues encountered with emitter sparking, and observed that providing lower flow rates to the emitter wedges resulted in a decrease in sparking events [75]. To validate these findings, the P0-grade reservoir frit was substituted with a P3-grade, resulting in a decrease in the pore size distribution from

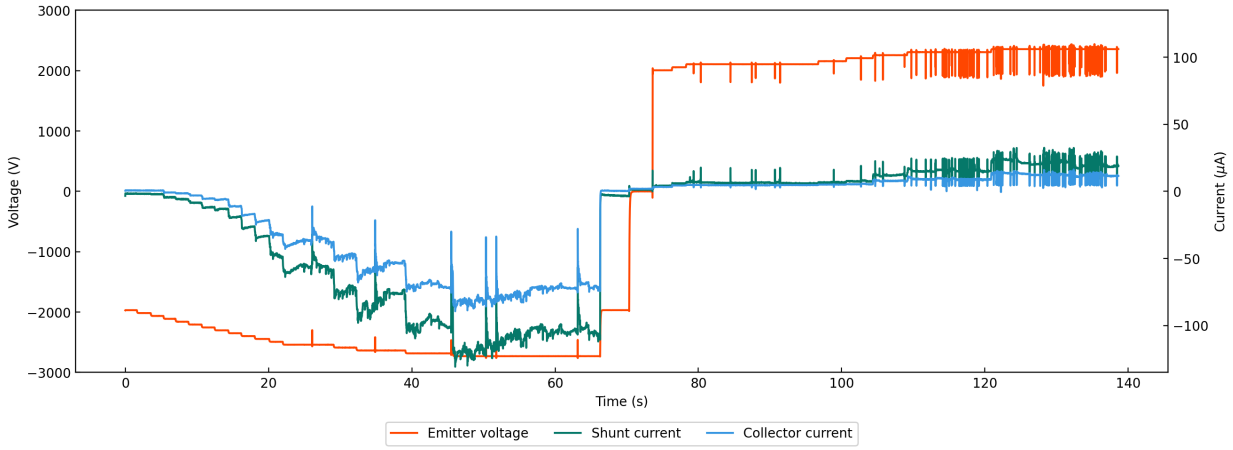

(a) Full time series results for a unipolar test, first testing negative polarity emission followed by the positive.

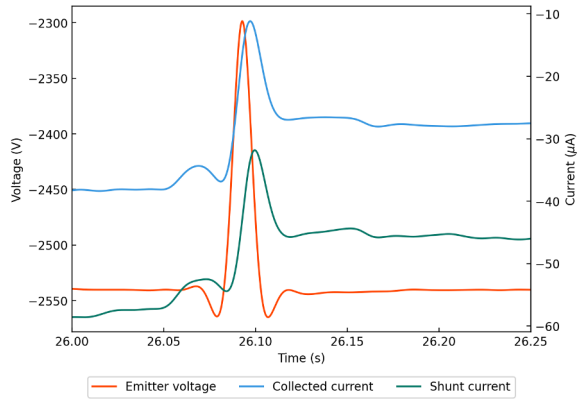

(b) A negative polarity sparking event causing a massive voltage drop and subsequent loss of emission over a short time interval.

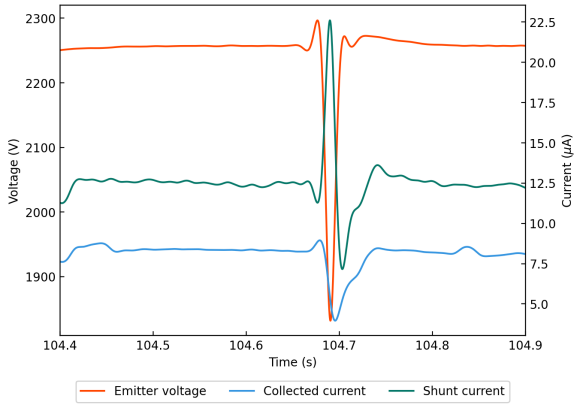

(c) A positive polarity sparking event causing a massive voltage drop and subsequent loss of emission over a short time interval.

Figure 5.6: Time series results for a unipolar test, highlighting emission instability and increased frequency of sparking events at higher voltages.

250 - 500 μm, to 16 - 40 μm. Although the thruster had to be disassembled for the reservoir replacement, efforts were made to maintain assembly similarity by preserving emitter height and by comparing the lateral alignment with microscope photography. As discussed in Section 2.6, smaller pore sizes lead to increased back-pressure, resulting in lower propellant flow rates to the emitter apex. Subsequent test results indicated a relatively increased onset voltage, even when accounting for variability between thruster assembly over multiple tests. These findings align with demonstrations by Courtney and Shea [93]. The I-V characteristic curve for this configuration is also plotted in Figure 5.5 for comparison with previous bipolar testing of the same linear emitter assembly using a P0 reservoir. Overall, the frequency of sparking events was not observed to markedly decrease. For this reason, subsequent I-V response tests were performed exclusively in the negative polarity with a P0 reservoir to explore a wider range of operation.

A final set of negative polarity P5 and P4-grade linear emitter tests sought to observe emission magnitudes over the widest achievable range by increasing the applied voltage until an electrical short occurred or when the power supply reached its maximum output current of 250 μA. Often,

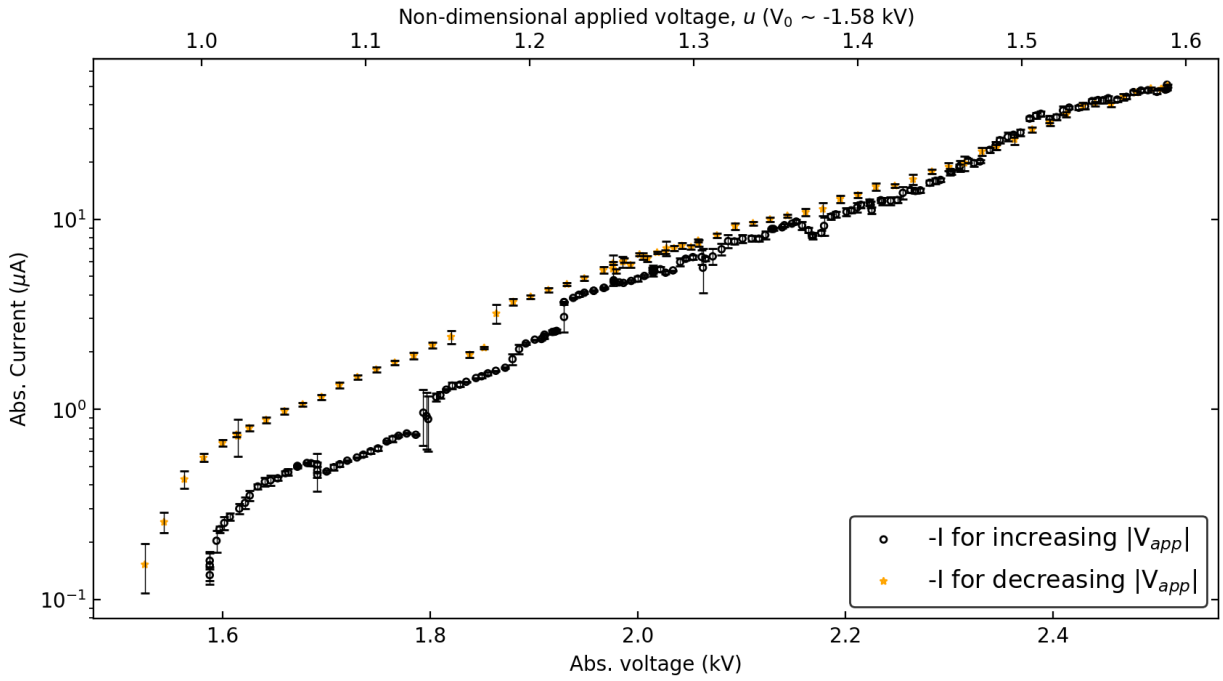

Figure 5.7: A logI-V characteristic curve for a P5-grade linear wedge with a P0 reservoir. Increasing the voltage magnitude to a maximum ($u = V/V_0 = 1.58$) followed by a decrease back to onset exhibits hysteresis.

the latter was far more likely to occur when operating solely in the negative polarity. A P5-grade emitter test is plotted in Figure 5.7 and shows emission magnitude measured as low as -0.13 ($\pm$0.01) μA at -1580 V. Note the use of a log scale and absolute emission to better represent operational ranges. A maximum current magnitude of -50.10 $\pm$0.81 μA with a transmission efficiency of 65% was reached at -2510 V ($u = 1.58$). Additionally, hysteresis was observed when the emitter voltage magnitude was increased to its maximum and then gradually reduced as illustrated in Figure 5.7.

For the P4-grade emitter test, stable emission was initially measured at -1.15 ($\pm$0.06) μA at approximately -1860 V, while the maximum collector current was measured to be -149.45 ($\pm$2.55) μA at -2340 V. The logI-V characteristic curve for the collected and shunt current is plotted in Figure 5.8. These tests often maxed out the power supply current limit early compared to the P5-grade emitters, resulting in minimum transmission efficiency of 59%. The results for both linear wedge emitter grade tests are displayed in Table 5.2.

BSG Grade	**Operation**	**Collected** [μA]	**Shunt** [μA]	η_{tr} [%]
P5	Stable onset ($u = 1.00$)	-0.13 ($\pm$0.01)	-0.97 ($\pm$0.04)	14
	Maximum ($u = 1.58$)	-50.10 ($\pm$0.81)	-76.71 ($\pm$1.28)	65
P4	Stable onset ($u = 1.00$)	-1.15 ($\pm$0.06)	-2.35 ($\pm$0.15)	49
	Maximum ($u = 1.28$)	-149.45 ($\pm$2.55)	-251.90 ($\pm$1.04)	59

Table 5.2: Extended throttle test results for the P5 and P4 linear wedge emitters, where $u = V/V_0$.

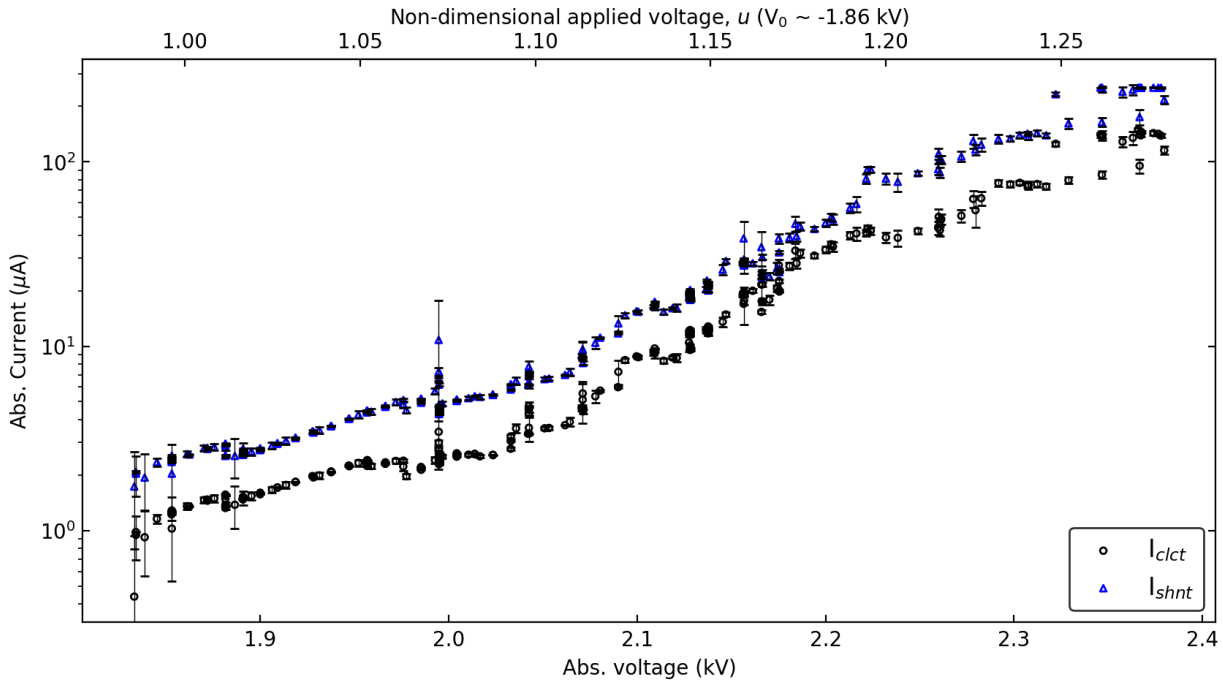

Figure 5.8: A logI-V characteristic curve for the collected and shunt current of a P4-grade linear wedge with a P0 reservoir ($u = V/V_0$).

5.3.1 Linear Wedge Emitter Results Discussion

The P5-grade linear wedge emitter test trials successfully provided baseline data to compare to the crescent emitter prototype. To calculate the thrust and specific impulse of the linear wedge, assumptions about the plume composition are made with assistance from experimental results in the literature. The beam is assumed to have no loss of energy ($V_{emitter} = V_{plume}$) and only the transmission efficiency is accounted for. Courtney and Shea provide time of flight results to determine the average specific charge of the plume for a P5-grade linear wedge emitter with a P0 reservoir using EMI-BF4 propellant [93]. For this configuration operating in the negative polarity, the average specific charge was 6.26×10^5 C/kg. For a P4-grade emitter, the corresponding specific charge is assumed to be the same average specific charge based on previous research of P3-grade emitter results performed at RAPPEL. Using Equation 2.9 and 2.10, the corresponding thrust and specific impulse for the final negative polarity trial is shown in Table 5.3 for stable and maximum applied voltage operation.

The anticipated performance results are contingent on the assumption of average specific

BSG Grade	**Operation**	**Thrust** [μN]	**Specific Impulse** [s]
P5	Stable onset ($u = 1.00$)	0.01 ($\pm$0.01)	3967 ($\pm$1)
	Maximum ($u = 1.58$)	6.01 ($\pm$0.2)	4399 ($\pm$5)
P4	Stable onset ($u = 1.00$)	0.09 ($\pm$0.005)	4820 ($\pm$4)
	Maximum ($u = 1.28$)	13.2 ($\pm$0.2)	5458 ($\pm$10)

Table 5.3: Predicted stable and maximum (non-dimensionalized as $u = V/V_0$) thrust and specific impulse values for both P5 and P4-grade linear wedge emitters operating in the negative polarity and assuming 100% thruster efficiency.

charge. Some evidence suggests that specific charge stays relatively consistent despite increasing voltage magnitudes [71], though, this was only tested for a small range. Additionally, increased rates of ion fragmentation upstream of the extractor electrode, induced by larger external fields, may cause charge neutralization and provide uncertainty on the high end of the voltage ranges tested.

Unfortunately, there is a lack of experimental data available concerning P4-grade emitter designs. In their TOF studies, Ma provide a comparison between P5 and P4-grade 100-tip emitter arrays with P0 reservoirs [90]. Their P4-grade results indicated a relatively monodisperse plume population comprised of monomer ions whereas their P5-grade results showed an increased proportion of dimer ions in the plume. This observation is counter-intuitive, as conventional expectations would assume that higher flow rates due to larger pore sizes would yield polydisperse populations of heavier ions and droplets with lower specific charge. Furthermore, these results are highly ionic when compared to other P5-grade emitter TOF results in the literature that utilize even smaller pore size reservoirs (P3 and P4-grade) [72, 71]. Ma attributes these disparities to the physical dimensions of the emitters, suggesting that a much thicker base and greater emitter height contribute to increased fluidic impedance [90]. However, this still does not explain the discrepancy between their P5 and P4-grade emitter results.

The specific charge assumption for the P4-grade emitter is thus derived from TOF results of prior droplet-mode P3-grade emitter experiments at RAPPEL that were provided to the author. The multimodal thruster model as outlined in Mallalieu and Jugroot [67] has a similar emitter design and incorporates a stainless steel disc of the same porosity grade as the emitter, serving as both a distal electrode and a reservoir. Given their plume measurements containing monomer, dimer and droplet fractions of 44, 39, and 17% respectively, the average specific charge of the P3 emitter was calculated to be 6.06×10^5. This magnitude is similar enough to results for the P5-grade emitter tip presented by Courtney and Shea that it was assumed to be the same for ease of computation. Notably, the plume population distribution presented by Mallalieu also closely matches that of the results for P5-grade emitter tips in experiments completed by Courtney and Shea [93]. However, the droplet masses for the droplet-mode experiments are estimated to be an order of magnitude larger than the latter, at 2.3×10^5 amu compared to 1×10^4 amu respectively. Finally, it should be noted that the although the droplet populations are assumed to be singly charged for this analysis, they can potentially contain tens to hundreds of elementary charges, approaching the Rayleigh limit [149]. This limit represents the maximum charge a droplet can carry before undergoing Coulomb fission.

Both emitter porosity grades exhibit an exponential increase in current with voltage over the entire tested range. Notably, there were almost no sub-μA currents measured for the P4-grade emitter. Compared to the P5-grade emitter, the P4-grade emitter was observed to be immediately stable at a relatively high current upon emission onset. This could indicate a large number of Taylor cones developing at the same time under a uniform electric field. However, this contradicts post-fabrication observations of higher rates of spalling along the wedge apex for P4-grade substrates. It could be that with higher flow to the wedge apex, the Taylor cone radius spans a larger group of pores, resulting in higher emission rates.

In the presented test cases, the transmission efficiency increases with applied voltage magnitude. It was expected that increased voltage would encourage higher rates of unstable off-axis emission and increased plume expansion, thus increasing the amount of impingement on the extractor and ions that clear the collector plate [150]. To clarify these findings, future work will implement a method to measure impinged extractor current. This will develop a better understanding of what fraction of the plume has impinged versus what has expanded beyond the collector plate.

The transmission efficiency range for the P5-grade emitter as shown in Table 5.2, appears

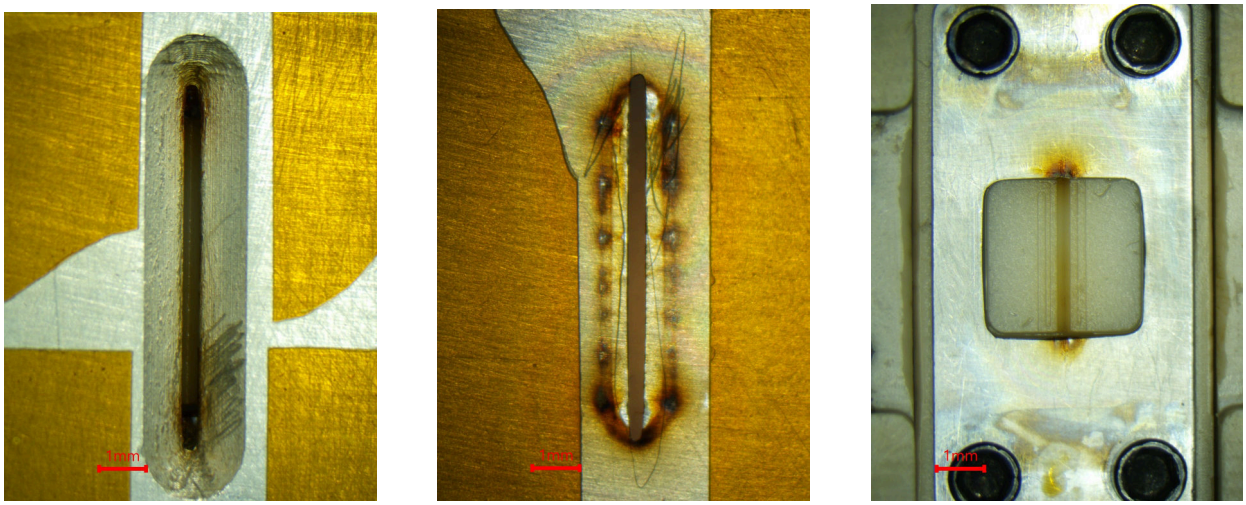

(a) Propellant collected on extractor slot chamfer.

(b) Extractor underside marked by wide axis firing and possibly sparking.

(c) Emitter and propellant housing surface.

Figure 5.9: Propellant decomposition throughout the thruster. Varied degrees of decomposition are qualitatively separated by: rainbow sheen, discoloured emitter, and brown residue.

to begin at an extremely low level. In contrast, the P4-grade emitter demonstrates a start at a much higher efficiency, before increasing to a similar maximum. This phenomenon could be linked to the isoamplifiers, which might be incapable of measuring at substantially lower currents compared to the variable gain amplifier. Modifying the isoamplifier resolution would necessitate either replacing the current shunt resistor or utilizing higher-quality components with a broader voltage input range.

When compared to modelling predictions developed in Chapter 3, these results are higher than those calculated in the onset voltage sweep study, around 1100 to 1500 V (Figure 3.6). The main source of variability between tests was through thruster assembly which proved difficult mitigate, especially when complete disassembly of the propellant housing was required to switch out emitters and reservoirs.

A solely negative emission approach has been previously taken in the literature for I-V characterization [75], and to explore alternative spacecraft neutralization methods during propulsion [151]. However, future work will seek to determine the direct cause of the sparking and further mitigation steps as the research regarding these topics are sparse. Future testing should be performed in as low vacuum as possible to stay under the Paschen curve, preventing possible low pressure arc discharges [152]. The roughness of the extractor slot could also be creating areas of concentrated electric field strength, wherein sharp points facilitate arc pathways to ground.

Close inspection of the thruster showed propellant in various stages of decomposition on the extractor chamfer slot and underside in Figures 5.9a and 5.9b, as well as on the emitter and distal electrode in Figure 5.9c. The yellow discolouration of the emitter and brown residue on the distal and extractor electrodes are consistent with post-test results found in the literature [90, 153].

Based on experiments by Terhune et al. [154], it could be that the yellow discolouration may be caused by high energy secondary species backstreaming towards the emitter tip. In their experiments with an externally wetted tungsten tip with both field emission (FE-SEM) and transmission electron microscopes (TEM), they conclude that the high energy electron environment of the TEM cause damage to the molecular structure of the IL which lead to solidification or gelling

into dendritic structures during emission. These structures persisted even after the electric field was removed. A similar phenomena may be occurring in the RAPPEL test chamber, where high energy secondary species produced through propellant impingement with the extractor electrode or collector plate are caused to backstream back towards the emitter tip. In the case of solely negative polarity emission, these backstreaming species may be positive metal ions that have been sputtered from the aforementioned surfaces.

A small number of tests were terminated due to an electrical short created between the emitter and the extractor. Inspection of the emitter showed evidence of propellant climbing the PEEK material at the point where the propellant housing and the thruster housing contact. From here, the propellant made an electrical connection to the point where the extractor is sitting on the thruster housing, leaving a clear path of brown decomposed propellant residue. To mitigate this, Kapton tape was wrapped around the extractor at points that contact the thruster housing (seen in Figure 5.9b) which deterred future short circuiting.

The observation of emission hysteresis is commonly described in literature by the relative sharpness of active Taylor cone tips compared to the emitter sharpness [75]. A lower critical electric field strength is required for maintaining emission concerning geometries with smaller radius of curvature. This introduces interesting power optimization scenarios during on-orbit operation - the thruster should be commanded to fire above the target and subsequently lowered to the thrust set-point so that the same emission current may be achieved at lower voltages.

The wide range of voltages tested here are not of interest for spacecraft propulsion due to excessive impingement and efficiency losses, but are important for comparison with a low tolerance multi-onset emitter prototype. If not assembled optimally, which may well be the case when assembling by visual inspection, the difference between the primary and secondary onset voltages may be too large and thus secondary onset may be unreachable.

5.4 Crescent Wedge Emitter Results

Crescent emitters fabricated from P5 and P4-grade BSG were tested with the same P0 reservoir to verify multi-onset voltage operation. The resultant thruster lateral and vertical alignment are shown in Figure 5.10a and 5.10b respectively.

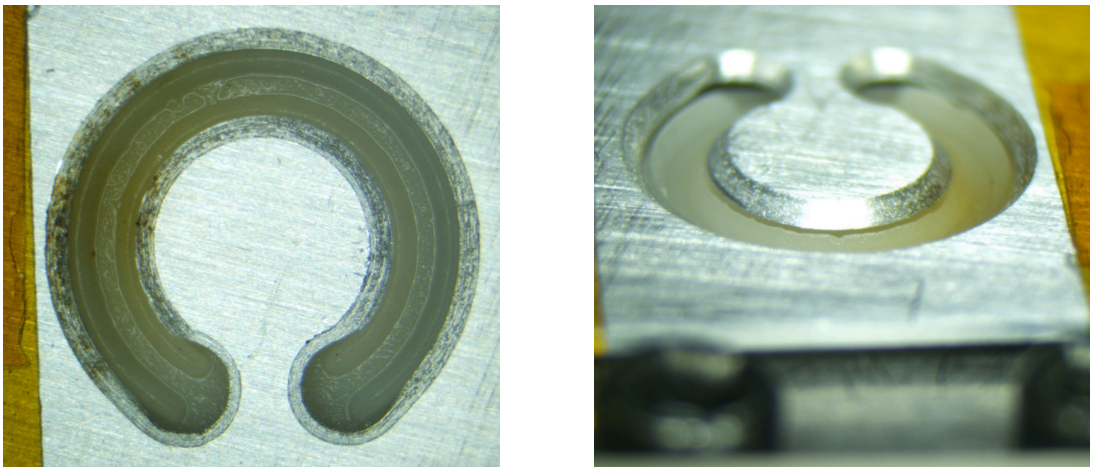

(a) Top down view of assembly.

(b) Angled-side view for height alignment estimate.

Figure 5.10: Typical views used for extractor alignment procedures performed between each test.

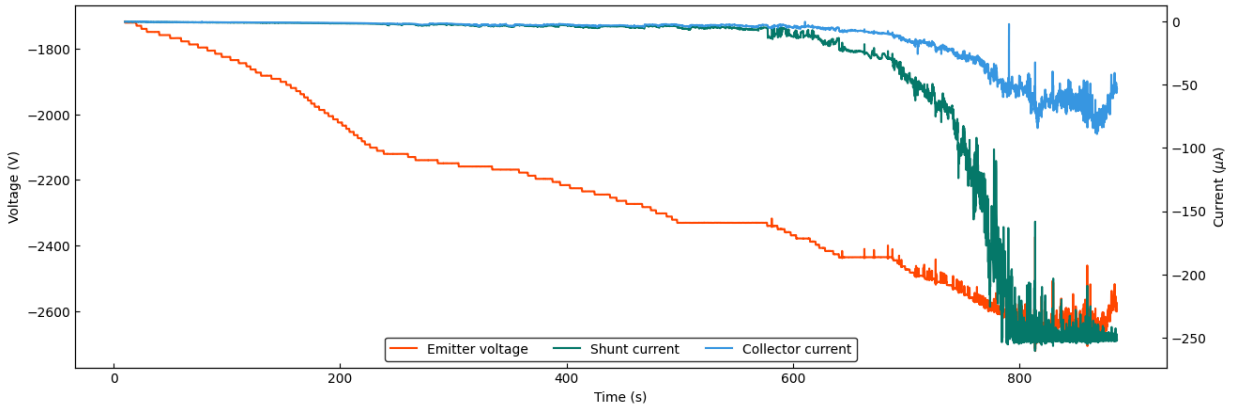

Figure 5.11: Time series results for negative polarity test of a P4-grade crescent emitter.

An example of the time series results of a P4-grade crescent emitter operating in the negative polarity are plotted in Figure 5.11. Characteristic current-voltage response testing was typically performed up to non-dimensionalized applied voltage values of greater than 1.6 before test termination due to reaching the power supply current output limit as measured by the shunt resistor. Similar to linear wedge testing, increased frequency of sparking events in the positive polarity prevented obtaining useful bipolar operation test results.

The logI-V characterization for the same test shown in Figure 5.11 is plotted in Figure 5.12. Emission onset is measured as -0.30 (±0.04) μA at -1750 V. The primary emission range is from $u = 1.00$ to approximately 1.32 before transitioning to a relatively rapid current increase. The maximum current collected from this test is -81.20 (±4.59) μA at -2660 V ($u = 1.52$). In the next

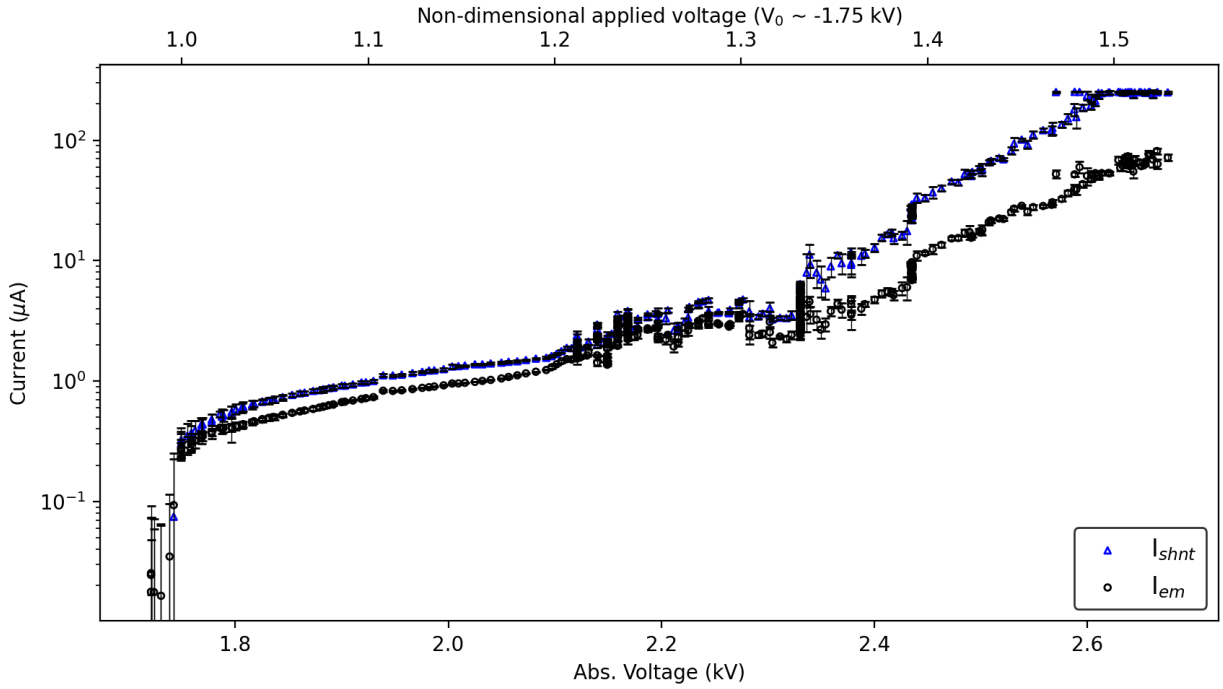

Figure 5.12: LogI-V characterization showing the shunt and collected current of a low quality P4-grade crescent emitter with a P0 reservoir.

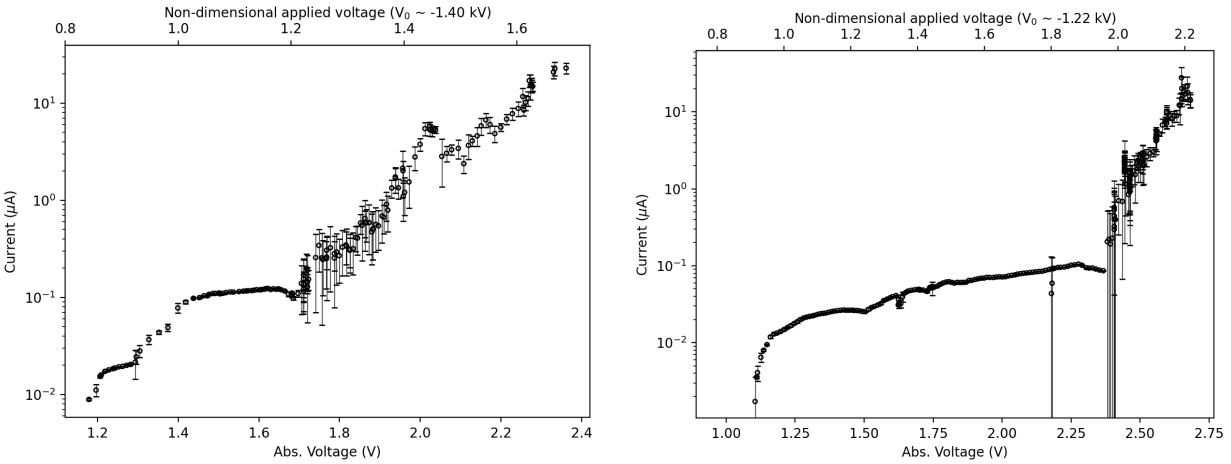

(a) Crescent emitter T1.

(b) Crescent emitter T2.

Figure 5.13: LogI-V characterizations for two crescent emitters of the same design from differing fabrication runs. Only collected current shown for clarity. Averaging of intermittent square pulsation in emission transition regions results in significant deviations from the mean, as evidenced by some error bars extending below the axis.

tests, two different P5-grade crescent emitter prototypes of the same porosity grade (hereafter referred to as T1 and T2 respectively) results are compared for repeatability. The emitters have the same design but were produced in separate fabrication runs. A sample of logI-V responses for each tested P5 grade crescent emitters are plotted in Figure 5.13, while primary and secondary stage emission results are displayed in Table 5.4. Onset voltages were observed to be -1400 and -1220 V for emitter T1 and T2 respectively. For both tests, an initial small current increase indicating emission onset is measured at low currents, similar to that of the linear emitter testing. As the voltage is continually increased, a period of large magnitude intermittent emission is observed, followed by steadier emission almost two orders of magnitude larger than after initial onset of emission was measured. An example of intermittent emission for emitter T2 is highlighted in Figure 5.14. Fluctuations in collected current during these periods were observed to be as large as 5 μA.

5.4.1 Crescent Wedge Emitter Results Discussion

After reaching a critical point at the high end of the primary emission region, the emitter undergoes square pulsation, for a short voltage range. This pulsation is similar in shape to that measured in experiments performed by Huang et al. [87]. When averaging over the square pulsation, a

Emitter	**Operation**	$u = V/V_0$	**Collected Current Range [μA]**	η_{tr} [%]
P5-T1	Primary	1.00 - 1.22	-0.09 ($\pm$0.01) to -0.11 ($\pm$0.01)	88 - 36
	Secondary	1.29 - 1.69	-0.34 ($\pm$0.13) to -22.92 ($\pm$3.02)	16 - 13
P5-T2	Primary	1.00 - 1.84	-0.01 ($\pm$0.01) to -0.10 ($\pm$0.01)	46 - 28
	Secondary	2.04 - 2.17	-2.37 ($\pm$0.55) to -27.81 ($\pm$9.81)	29 - 26
P4	Primary	1.00 - 1.39	-0.30 ($\pm$0.04) to -7.84 ($\pm$0.34)	86 - 32
	Secondary	1.39 - 1.52	-8.52 ($\pm$0.18) to -81.20 ($\pm$4.59)	31 - 32

Table 5.4: Primary and secondary emission results for P5-grade crescent emitters T1 and T2.

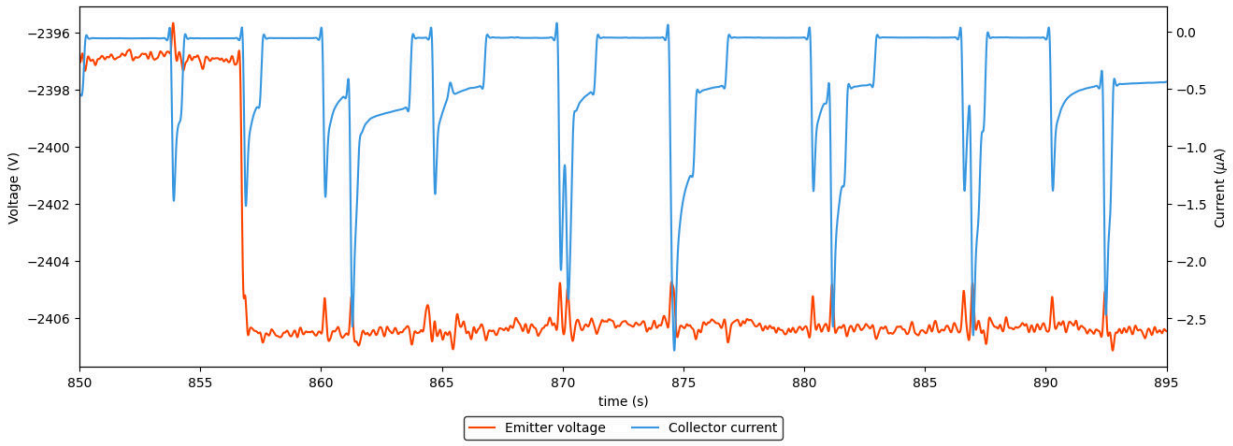

Figure 5.14: Observation of large magnitude intermittent emission for emitter T2 ($u = 1.96$).

significant deviation from the mean is calculated, which explains the exceedingly large error bars in the emission transition region. A direct explanation of the mechanisms behind square pulsation is not provided. However, inferring from the experimental work of Chen et al., square pulsation behaviour could possibly be the result of the flow rate to the wedge apex closely matching that of the flow rate consumed by electrospraying [75]. This results in 'intermediate zones', where emission is observed to repeatedly appear and disappear as propellant is consumed slightly faster than it can be supplied. This could also be attributed to the secondary wedge nearing emission onset.

As the voltage magnitude is further increased, shot pulsation appears to settle, as evidenced by a reduced error, and the emission increases at a faster rate, somewhat similar to the slope of the linear wedge. A distinct increase in rate of emission with voltage has not yet been observed in linear wedge testing. However, a glaring difference between the two P5-grade prototypes is the fact that the current magnitude for the crescent wedge is much smaller overall than that of the linear emitter. It was expected for a primary wedge length of 14.5 mm, that the low-end output of the crescent wedge would exceed that of the 7 mm linear wedge. Note that the high-end transmission efficiency is much lower than the linear wedge. It is possible that the plume is diverging at a larger angle than predicted by the particle tracing model. If the shunt current is assumed to represent the entire current output of the emitter, the exceedingly large measurements in comparison to those measured at collector plate (as depicted in the time series results in Figure 5.12) support evidence of multi-onset voltage behaviour. Additionally, the alignment process for the crescent wedge prototype was found to be much more difficult than for the linear wedge. It is possible that crescent extractor misalignment reduced the effective emitting area for both wedges, resulting in an overall lower current output.

Presently, the only evidence of multi-onset emission is through the change in emission rate behaviour as discussed previously. However, diagnostic tools such as a motorized wire probe [77] or computed tomography current mapping [155], could spatially resolve the beam distribution across the wedges, confirming the presence of disparate emission sites at voltages related to the primary and secondary emission regimes. In addition, a larger collector plate area and extractor current measurement capabilities would assist in confirming both of these hypotheses by providing a higher resolution transmission efficiency estimate.

In the P5-grade crescent wedge data, emission onset is first observed at sub-μA ranges of currents and slowly increases with voltage until a critical point. For comparison, a linear least squares regression analysis of each characteristic log-current voltage response is presented in Figure 5.15,

with a schematic summary of the predicted primary and secondary emission regimes overlaid in Figure 5.15c. The relative slope of the P5-grade crescent wedge increase corresponds to $m = 4.7$ ($R^2 = 0.84$) and 1.7 ($R^2 = 0.94$) for wedge T1 and T2 respectively. In many tests, emission was measured above the stated onset voltage (for u less than one) at current levels of close to an order of magnitude less. This is assumed to be the result of edge effects and misalignment causing early emission onset. Compared to the more easily aligned linear emitter, slow emission onset was measured across a much wider range of applied voltages. The sudden increase in current to μA levels is indicative of a large number of emission sites forming along the wedge all at once and is therefore taken to be the characteristic onset voltage of the emitter-extractor assembly. This rapid ramping to initial onset also contributed to a weaker R^2 value for many of the crescent wedge test primary emission region slopes.

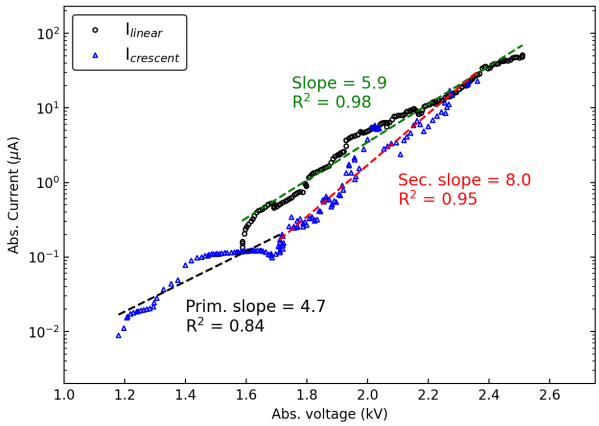

(a) P5-grade wedges: crescent-T1 compared to linear baseline.

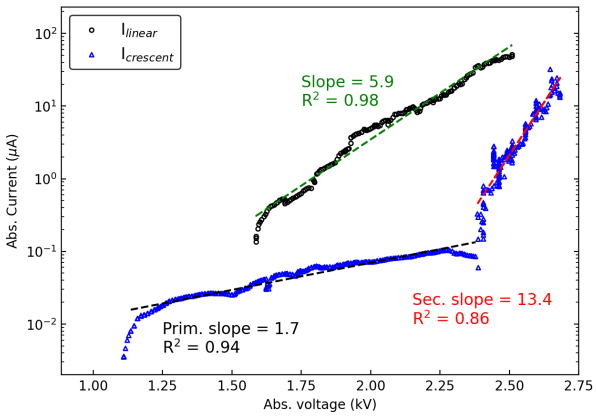

(b) P5-grade wedges: crescent-T2 compared to linear baseline.

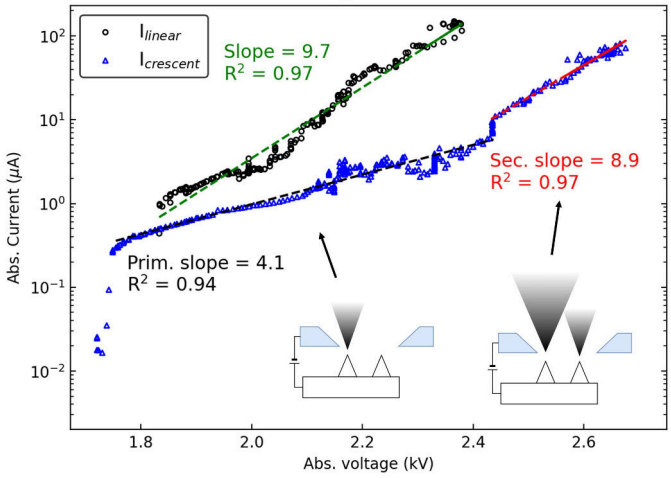

(c) P5-grade wedges: crescent-T2 compared to linear baseline.

Figure 5.15: Least squares linear regression analysis results for the log-current voltage response of the linear and crescent emitter wedges tested for each porosity grade. Collected current results only. Shunt and error bars removed for clarity. Note the difference in x-axis scale between the two emitter grades.

For the P5-grade test results presented, the difference between the primary and secondary onset voltage for emitter T2 is observed to be much larger than that of T1 and general onset voltage predictions from Section 3.5.2. In fact for many tests, the difference varied widely. This is to be expected, given that the model presented in Section 3.5.2 showed how sensitive the onset voltage would be to extractor outer radius alignment (see Figure 3.8).

The P4-grade crescent emitter results also provide evidence of stable emission for two firing regimes across a wide applied voltage range. The log-current response shows a gradual increase ($m = 4.1$, $R^2 = 0.94$) up until approximately 2300 V, where a transition to a distinctly steeper increase ($m = 8.9$, $R^2 = 0.97$) is observed for larger voltage magnitudes. Notably, there is a much smaller period of instability when transitioning to the secondary emission range compared to the P5-grade crescent emitter. While multi-onset behaviour was not present during the testing of the P4-grade linear wedge as shown in Figure 5.8, it cannot be definitively decided that the linear wedge would not show the same behaviour. This is due to the fact that the linear wedge was only able to be tested up to a maximum nondimensionalized voltage of 1.28 before the power supplies became current limited, whereas the crescent wedge emitter was able to reach approximately $u = 1.48$ before becoming current limited.

Comparing the current-voltage response testing for the P5-grade linear and crescent emitter prototypes provides some evidence of multi-onset emission. The weakly-fit slope of primary emission region for the P5-grade emitters closely match or are slightly lower, depending on if the initial edge effects emission data is considered. In contrast, the slope of the secondary emission region for the P4-grade emitter more closely matches that of the P4-grade linear wedge. The P4-grade crescent emitter results are more indicative of a relative current increase that would be expected from an emitter displaying multi-onset voltage behaviour. However, the tolerances of both emitter grade configurations in their current stage are too large for on-orbit operational use. The thrust and specific impulse is estimated for the crescent wedges using the same methodology from the linear wedge results analysis and are presented in Table 5.5. Notably, the estimated specific impulse of the P5 wedges are somewhat similar to the 3D symmetric wedge model in Section 3.6, which was calculated to be 4550 s. However, it is difficult to compare these values due to the dependence of specific impulse on voltage (Eq. 2.10).

To restate the intended application of the research, the successful demonstration of an electrospray emitter with multi-onset voltage capability enables an increased performance range for the propulsion system. For a single onset voltage emitter, the applied voltage may only be so far above the onset before electrospray instabilities caused increased rates of impingement leading to a shortened thruster lifespan. A smaller difference between primary and secondary onset voltages is warranted to stay within the limits of the electrohydrodynamic stability of the primary wedge. In its current state, the difference between primary and secondary emission seems to indicate that the primary region would be ideal for low thrust, high accuracy impulse bit manoeuvres such

Emitter	**Operation**	**Thrust [μN]**	**Specific Impulse [s]**
P5-T1	Primary (u = 1.00 - 1.22)	0.007 ($\pm$0.001) - 0.01 ($\pm$0.001)	3390 - 3692 ($\pm$6)
	Secondary (u = 1.29 - 1.69)	0.03 ($\pm$0.001) - 2.52 ($\pm$0.33)	3836 - 4374 ($\pm$22)
P5-T2	Primary (u = 1.00 - 1.84)	0.001 ($\pm$0.001) - 0.003 ($\pm$0.001)	3148 - 3356 ($\pm$5)
	Secondary (u = 2.04 - 2.17)	0.29 ($\pm$0.06) - 3.72 ($\pm$1.39)	4511 - 4631 ($\pm$17)
P4	Primary (u = 1.00 - 1.39)	0.02 ($\pm$0.004) - 0.6 ($\pm$0.03)	4768 - 5530 ($\pm$2)
	Secondary (u = 1.39 - 1.52)	0.7 ($\pm$0.01) - 7.6 ($\pm$0.4)	5537 - 5793 ($\pm$4)

Table 5.5: Primary onset and maximum ($u = V/V_0$) thrust and specific impulse estimations for the tested crescent emitters.

as attitude control and pointing over a wide range of voltages. Meanwhile, the relatively higher thrust, low resolution, secondary emission region at higher voltages could be used for manoeuvres such as collision avoidance.

At maximum applied voltages, the glow discharge resulting from secondary species emission is apparent for both the linear and crescent wedge configurations as depicted in Figure 5.16a and 5.16b respectively. The glow discharge was too faint to capture at emission levels just above onset which would have been useful for capturing visual evidence via glow discharge of the primary wedge firing followed by both wedges firing once the applied voltage had been sufficiently raised. Note the difference in colour between the two prototypes resulting from radiation from different SSE pathways. The plasma of the linear wedge glow discharge takes on a purple hue whereas the crescent wedge glow discharge is much bluer in colour. The difference between these two glows could be due to a differing fraction of any number of direct and indirect photon emission mechanisms as described by Uchizono et al. [84]: directly through sputtering and molecular dissociation or indirectly through secondary species backstreaming to the electrospray source. The most luminous point of the crescent emitter glow corresponds to its apex. This occurrence is probably due to positively charged species that backstream toward the apex Taylor cones with enhanced negative electric fields, where they interact with the outgoing primary propellant ions or droplet clusters [156].

Although the suppression grid is biased to -30 V, the effect of SSE is still quite obvious and is likely impacting the real current measurements. Backstreaming secondary species has been found to increase measurement uncertainty considerably through out-sized extractor impingement readings, as well as emitter heating leading to propellant decomposition [84, 57]. Additionally, given the transition to solely negative polarity testing over the course of the test campaign, the role of the negatively biased suppression grid should have been more deeply considered. While secondary electron backstreaming from the collector plate would indeed have been reduced, incoming negative ions emitted from the thruster as well as positively charged secondary species (i.e. sputtered ions) may have been disproportionately affected by the intermediary electric field.

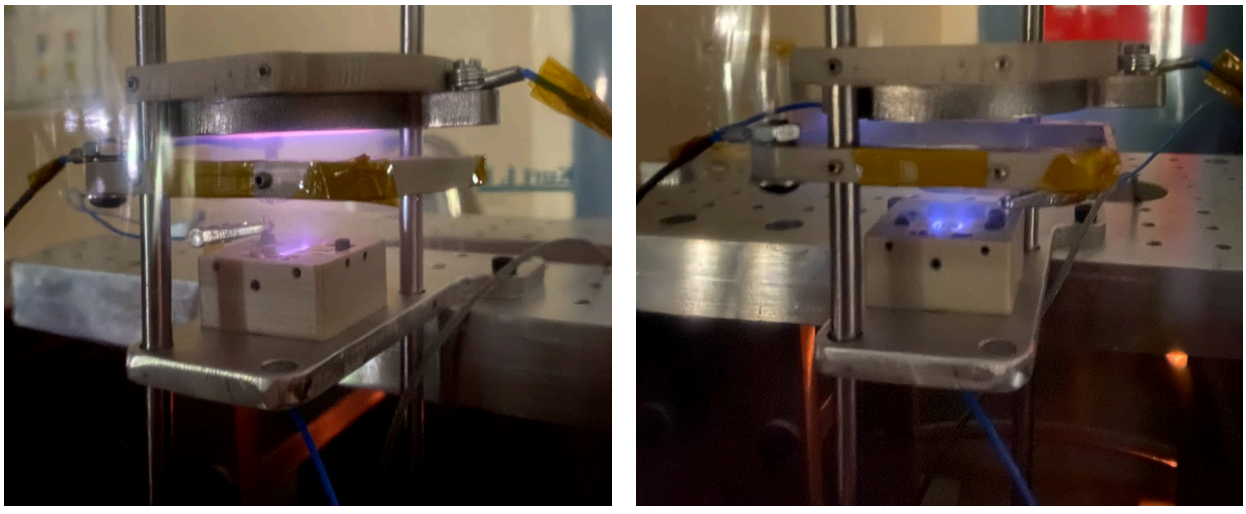

(a) Linear wedge emitter purple glow discharge. (b) Crescent wedge emitter T2 blue glow discharge.

Figure 5.16: Long term exposures (10 s) of the glow discharges for a linear emitter (-2500 V, $u = 1.58$) and a crescent emitter (-2480 V, $u = 2.03$). The orange glow below the test stand is due to hot cathode ion gauge operation.

5.5 Concluding Remarks

The experimental setup at RAPPEL and the results for the P5-grade and P4-grade BSG linear and crescent wedge ESP emitter prototypes have been presented. The linear wedge emitter provided baseline data as well as validation of the new control and data acquisition PCB; its associated LabView program; and the collector plate and SSE suppression grid test stand assembly. A semi-log current-voltage response test was successfully completed over a wide voltage range (up to $u = 1.58$) in the negative polarity for the P5-grade linear wedge emitter. In contrast, the results for the P4-grade emitter were current-limited soon after onset at approximately $u = 1.28$. The respective slopes for logI-V characterization were 5.9 and 9.7.

The semi-log current-voltage response test for the crescent wedge emitter measured a much lower overall current magnitude, though evidence of multi-onset voltage behaviour was still observed. The gradual increase in current transitioning to a relatively rapid rise corresponds to behaviour expected of emission transitioning from one to two wedges simultaneously. The P5-grade crescent wedge showed an average logarithmic increase in emission with voltage corresponding to a relative slope of 3.2 before transitioning to a slope of 10.7 at 600 V beyond emission onset. The P4-grade crescent wedge showed a similar behaviour, increasing from 4.1 to 8.9 at 600 V beyond emission onset. Validation of this phenomena necessitates improved component tolerance and alignment procedures, as well as advanced diagnostics tools.

6 Summary, Concluding Remarks and Recommendations

Electrospray propulsion is a low-thrust, high efficiency form of satellite micropropulsion uniquely known for its small form-factor, high thrust accuracy, and exceptional scalability. The porous variant of electrospray propulsion further improves system capabilities by significantly reducing flow rates, thus encouraging efficient operation in the pure ionic regime, as well as taking advantage of passive capillary flow to simplify propellant transport mechanisms. A mature form of the technology allowing for extended mission lifetimes and greater thrust control shows promise in substantially expanding the nanosatellite mission design space. The latter is investigated in this thesis as an electrospray emitter that exhibits multi-onset voltage capability which has the opportunity to provide the spacecraft with an wider range of thrust set points to choose from during its mission.

Conventional CNC fabrication processes provide a cost-effective platform for exploring new ideas through rapid prototyping and increased access to scientific and engineering research. There are many instances where porous emitters have been manufactured through conventional CNC milling means and have performed extremely well in experimental settings. However, details on how such emitters are fabricated are sparse, regardless of the stock material used. A preliminary investigation into optimal machining strategies is warranted to build a foundation for the manufacturing of high quality emitters.

6.1 Summary and Key Results

The thruster designed in this thesis is adapted from the Air Force Electrospray Thruster [72] architecture and was presented as a platform to test linear and crescent wedge emitter prototypes. Simplified 2D onset voltage studies used geometric parameter sweeps to quantify how design variables such as emitter radius of curvature and slot width are sensitive to changes in electric field strength and should be given priority during fabrication. A 3D electrostatic simulation provided insight into building electric field edge effect mitigation practice into extractor design. The implementation of an underside chamfer and blunted apex ends was observed to reduce the overall field spiking so that early onset of emission would be less likely to occur. Finally, charged particle tracing simulations completed for the linear and crescent wedge assemblies compare phenomena of interest such as dissimilar molecular velocities, ion impingement and plume expansion. The results indicated optimal crescent extractor configurations and maximum predicted plume angle and impingement of 54 degrees and 7% respectively.

The micromilling of porous borosilicate glass into emitter prototypes was explored. Milling strategies conducive to the high quality wedges, measured in terms of sharpness and uniformity, were determined to be as a primarily a result of using up-milling cutting and effective chip evacuation. Full axial depths of cut with small radial stepover and a feed rate of 0.5 to 1 in/min also

BSG Grade	Operation	Current (μA)	Avg. Slope (μA/kV)	Norm. V Range, u
P5	Linear	-0.1 to -50.1	5.9	1.00 to 1.58
	Primary	-0.01 to -0.1	3.2	1.00 to 1.84
	Secondary	-0.3 to -27.8	10.7	1.29 to 2.17
P4	Linear	-1.15 to -149.5	9.7	1.00 to 1.28
	Primary	-0.3 to -7.8	4.1	1.00 to 1.32
	Secondary	-8.5 to -81.2	8.9	1.32 to 1.52

Table 6.1: Summarized results for multi-onset voltage extended throttle testing of the linear and crescent wedge configurations. The results headings cover the measured current range, average current-voltage response slope, and normalized voltage range (u), respectively.

benefitted tip quality.

An analysis was provided for the experimental results of the highest quality P5 and P4-grade linear and crescent wedge emitters that were fabricated. The linear emitters demonstrated stable, logarithmic current emission across a broad range of negative voltages, providing baseline data to compare to the crescent wedge emitters. Frequent sparking events in the positive polarity that could not be reduced at lower propellant flow rates prevented characterization to the same extent.

The crescent wedge emitter design exhibited a distinct characteristic current-voltage curve compared to that of the linear wedge, showing initial increases followed by periods of instability, and finally, dramatic increases in current magnitude. This is indicative of two separate operating modes involving a primary wedge firing alone, followed by the primary and secondary wedges firing simultaneously once the voltage had increased past a critical threshold. The results are summarized in Table 6.1. However, issues with alignment and plume expansion persisted (which has also been well documented in literature), as the collected current remained lower when compared the linear wedge, despite having a much smaller active emission area overall.

In conclusion, the research carried out in this thesis offers several contributions to the field of electrospray propulsion. For instance, the fabrication of two wedge emitter geometries using widely available conventional machining methods has been presented, with initial efforts to determine strategies to optimize wedge quality for stable electrospray emission. A robust custom control and data acquisition circuit hardware and software suite has been developed to perform emission testing over a wide range of voltages. A multi-onset voltage emitter prototype has been proposed, supported by electrostatic and particle tracing modelling as well as extensive high voltage characterization. In demonstrating two distinct rates of current change with voltage, the prototype introduces a novel emission behavior not previously documented in the literature. In summary, this research contributes to the ongoing improvement of electrospray thruster capabilities, which will increase the viability of electrospray propulsion for future small spacecraft missions. More broadly, this seeks to expand the nanosatellite mission design space through the allowance of longer duration and higher functionality missions.

6.2 Recommendations for Future Work

Future work should seek to improve the desktop CNC machine and its tooling to increase accuracy and repeatability. The machine's vibration frequency should be quantified. Additionally, the impact of reducing its vibration by mounting it on a vibration-absorbing table, similar to many professional micromilling machines, should be assessed for its effect on emitter quality. High quality diamond burr tooling in combination with 5-axis milling techniques may also provide some improvement to edge quality. Such tooling and techniques such as milling at angles off-normal

to the workpiece surface have been successfully used to cut brittle materials such as non-porous glasses which may have some application to porous borosilicate glass [157].

Wedges featuring larger apex radii of curvature may be beneficial for increasing the quality of emitter uniformity by deterring the spalling of pieces approximately same size as the sintered particles. However, care would need to be taken to avoid curvatures of excessive size, as this would significantly increase the characteristic onset voltage and promote the production of Taylor cones that may fire off-axis.

The machining of other porous materials should also be considered. For example, the use of ceramics seems to be growing in the electrospray research [158, 105] and although they are mutually exclusive topics at the time of writing, there is a vast amount of literature to draw from related to the micromilling (e.g. medical, aerospace, etc.) and electrospraying of porous tungsten. Electrospray research concerning ceramics has demonstrated that high quality molds can be created through machining or 3D printing requiring only a small finishing pass to improve tip quality with a smaller impact on tool life [95].

The next iteration of the multi-onset emitter format should take advantage of MEMS fabrication techniques to improve emitter uniformity and alignment tolerances. A uniform emitter with a dramatically reduced onset voltage difference of 100 V or less between the primary and secondary wedges is envisioned where instabilities of the primary wedge are minimized when operation of both wedges is commanded. Furthermore, the stacking of additional components that can provide system tuning in complimentary ways such as an accelerator grid [110], or an actively fed propellant system [159] can expand the propulsion system's performance range to a greater extent.

The extractor alignment procedure should be re-developed to improve alignment tolerance during test campaigns. The number of set screws required should be reduced, if used at all. For example, there was no knowledge of the protruding length of each height adjustment set screw when assembling the thruster. Unintended asymmetric adjustment of each set screw often led to a plane tilt for the propellant housing, requiring tedious adjustment of the height under the microscope until all sides of an emitter were estimated to be at the same distance to the extractor. An alternative setup could take advantage of locking set screws with just one borehole for adjustment using a micrometer screw such as those commonly used for photonics research.

While the control and data acquisition board and associated electronics infrastructure was successful in maintaining emission over intended voltage ranges up to ± 3500 V and operated for extended periods of time, there are many measurement errors such as inrush current and power supply ringing that need to be resolved in the next iteration. The power supplies must be upgraded in order to ensure they do not limit the current drawn from the emitter. As the control and data acquisition board is intended for experimental use only, it is not limited to CubeSat sized space restrictions allowing for a more robust choice of supply. A solution for measuring the current on the shunt and the extractor electrode over a range of several magnitudes must be implemented that is resistant to transient sparking events.

Lastly, future diagnostics improvement should seek to implement secondary species emission mitigation recommendations [84], such as non-flat plate geometries that are biased to a sufficient degree; adequate thruster to collector plate distances; moving away from intermediary suppression grids that can clog towards 'electron cage' electrodes that frame the collector plate; and finally, the use of facility materials with low sputtering and secondary electron yields. The addition of a vacuum safe long exposure camera would likely provide valuable feedback in the early emission stages, as well as during transient sparking events. A wire probe would assist in understanding how the crescent emitter plume shape differs from that of the linear. The use of time of flight mass spectrometry may also provide a more detailed performance estimate and insight into the operating modes of the primary and secondary wedges over a range of voltages.

References

[1] Kirk Woellert, Pascale Ehrenfreund, Antonio J Ricco, and Henry Hertzfeld. Cubesats: Cost-effective science and technology platforms for emerging and developing nations. *Advances in space Research*, 47(4):663–684, 2011.

[2] Federal Aviation Administration. The annual compendium of commercial space transportation: 2018. `https://www.faa.gov/sites/faa.gov/files/space/additional_information/2018_AST_Compendium.pdf`, Accessed: 2023-07-21.

[3] Thomas Roberts. Space launch to low earth orbit: How much does it cost? `https://aerospace.csis.org/data/space-launch-to-low-earth-orbit-how-much-does-it-cost/`, Accessed: 2023-07-21.

[4] Brad Cotton, Ian Bennett, and Robert Zee. On-orbit results from the canx-7 drag sail deorbit mission. In *Proceedings of the Small Satellite Conference*, 2017.

[5] Mark A Skinner, Michael Coletti, Matthew C Voss, Tomas Svitek, John C Lee, Kerstyn Auman, Hemanshu Patel, and Eamonn J Moyer. Mitigating cubesat confusion: Results of in-flight technical demonstrations of candidate tracking and identification technologies. *Journal of Space Safety Engineering*, 9(3):403–409, 2022.

[6] Tory Bruno. How to fix the pollution of orbital debris. `https://medium.com/@ToryBrunoULA/how-to-fix-the-pollution-of-orbital-debris-d4a766c563ee`, Accessed: 2023-07-21.

[7] Thyrso Villela, Cesar A Costa, Alessandra M Brandão, Fernando T Bueno, Rodrigo Leonardi, et al. Towards the thousandth cubesat: A statistical overview. *International Journal of Aerospace Engineering*, 2019, 2019.

[8] Erik Kulu. Nanosatellite launch forecasts-track record and latest prediction. *Small Satellite Conference*, 2022.

[9] David Krejci and Paulo Lozano. Space propulsion technology for small spacecraft. *Proceedings of the IEEE*, 106(3):362–378, 2018.

[10] Joseph N Pelton and Scott Madry. *Handbook of Small Satellites; Technology, Design, Manufacture, Applications, Economics and Regulation*. Springer, 2020.

[11] Grant Bonin, Jesse Hiemstra, Thomas Sears, and Robert Zee. The canx-7 drag sail demonstration mission: enabling environmental stewardship for nano-and microsatellites. *27th Annual Conference on Small Satellites, 2013*, 2013.

[12] Federal Communications Commission. Mitigation of orbital debris in the new space age. `https://docs.fcc.gov/public/attachments/DOC-363486A1.pdf`, Accessed: 23-07-23.

[13] Yu-hui Chiu and Rainer A Dressler. Ionic liquids for space propulsion. In *ACS Symposium Series 975: Ionic Liquids IV*. ACS Publications, 2007.

[14] George P Sutton and Oscar Biblarz. *Rocket propulsion elements*. John Wiley & Sons, 2016.

[15] Dan M Goebel and Ira Katz. *Fundamentals of electric propulsion: ion and Hall thrusters*. John Wiley & Sons, 2008.

[16] Bryan Little and Manish Jugroot. Development of a microthrust balance and ion beam measurement system: Characterizing a dual-mode thruster for spacecraft. *Vacuum*, 164:367–380, 2019.

[17] Benjamin D Prince, Bruce A Fritz, and Yu-Hui Chiu. Ionic liquids in electrospray propulsion systems. In *Ionic Liquids: Science and Applications*, pages 27–49. ACS Publications, 2012.

[18] Chengyu Ma and Charles N Ryan. The design and characterization of a porous-emitter electrospray thruster (pet-100) for interplanetary cubesats. In *Proceedings of the 7th Interplanetary Cubesat Workshop, Paris, France*, pages 29–30, 2018.

[19] David Krejci and Alexander Reissner. The first 100 feep propulsion systems in space: A statistical view and lessons learnt of 4 years of enpulsion. In *37th International Electric Propulsion Conference*, 2022.

[20] Ivanhoe Vasiljevich, Martin Tajmar, Walter Grienauer, Florin Plesescu, Nembo Buldrini, Jose Gonzalez del Amo, Bernardo Carnicero Domunguez, and Maurizio Betto. Development of an indium mn-feep thruster. In *44th AIAA/ASME/SAE/ASEE Joint Propulsion Conference & Exhibit*, page 4534, 2008.

[21] James Richard Wertz, David F Everett, and Jeffery John Puschell. *Space mission engineering: the new SMAD*. Space Technology Library, 2011.

[22] Patrick Gavigan. Estimation of minimum required thrust for spacecraft collision avoidance, tm 2013-113. Technical report, Defence Research and Development Canada, 2013.

[23] Oliver Jia-Richards, Paulo C Lozano, David C Sternberg, Daniel Grebow, and Swati Mohan. Feasibility of a deep-space cubesat mission with a stage-based electrospray propulsion system. In *2020 IEEE Aerospace Conference*, pages 1–10. IEEE, 2020.

[24] Pau Amaro-Seoane, Heather Audley, Stanislav Babak, John Baker, Enrico Barausse, Peter Bender, Emanuele Berti, Pierre Binetruy, Michael Born, Daniele Bortoluzzi, et al. Laser interferometer space antenna. *ESA PUBLICATIONS ESTEC*, 2017.

[25] John Ziemer, Colleen Marrese-Reading, Curt Cutler, Charles Dunn, Andrew Romero-Wolf, Shahram Javidnia, Thanh Le, Irena Li, Phil Barela, Nathaniel Demmons, et al. In-flight verification and validation of colloid microthruster performance. In *2018 AIAA Propulsion and Energy Forum, Cincinnati, Ohio*, 2018.

[26] European Space Agency. Esa creates quietest place in space. `https://sci.esa.int/web/lisa-pathfinder/-/59961-esa-creates-quietest-place-in-space`, Accessed: 23-07-25.

[27] Nathaniel R Demmons, Zack Wood, and Nereo Alvarez. Characterization of a high thrust, pressure-fed electrospray thruster for precision attitude control applications. In *AIAA Propulsion and Energy 2019 Forum*, page 3817, 2019.

[28] Fernando Mier-Hicks and Paulo C Lozano. Electrospray thrusters as precise attitude control actuators for small satellites. *Journal of Guidance, Control, and Dynamics*, 40(3):642–649, 2017.

[29] David Krejci, Fernando Mier-Hicks, Corey Fucetola, Paulo Lozano, Andrea Hsu Schouten, and Francois Martel. Design and characterization of a scalable ion electrospray propulsion

system. In *Joint Conference of 30th International Symposium on Space Technology and Science, 34th International Electric Propulsion Conference and 6th Nano-satellite Symposium*, 2015.

[30] Lord Rayleigh. Xx. on the equilibrium of liquid conducting masses charged with electricity. *The London, Edinburgh, and Dublin Philosophical Magazine and Journal of Science*, 14(87):184–186, 1882.

[31] John Zeleny. The electrical discharge from liquid points, and a hydrostatic method of measuring the electric intensity at their surfaces. *Physical Review*, 3(2):69, 1914.

[32] Victor E Krohn Jr. Glycerol droplets for electrostatic propulsion. *Progress in Astronautics and Aeronautics*, 9, 1963.

[33] M Gamero-Castano and V Hruby. Electrospray as a source of nanoparticles for efficient colloid thrusters. *Journal of Propulsion and Power*, 17(5):977–987, 2001.

[34] Renato Krpoun and Herbert R Shea. A method to determine the onset voltage of single and arrays of electrospray emitters. *Journal of Applied Physics*, 104(6), 2008.

[35] Geoffrey Ingram Taylor. Disintegration of water drops in an electric field. *Proceedings of the Royal Society of London. Series A. Mathematical and Physical Sciences*, 280(1382):383–397, 1964.

[36] Juan Fernández de La Mora. The fluid dynamics of taylor cones. *Annu. Rev. Fluid Mech.*, 39:217–243, 2007.

[37] JR Melcher and GI Taylor. Electrohydrodynamics: a review of the role of interfacial shear stresses. *Annual review of fluid mechanics*, 1(1):111–146, 1969.

[38] DA Saville. Electrohydrodynamics: the taylor-melcher leaky dielectric model. *Annual review of fluid mechanics*, 29(1):27–64, 1997.

[39] John B Fenn, Matthias Mann, Chin Kai Meng, Shek Fu Wong, and Craig M Whitehouse. Electrospray ionization for mass spectrometry of large biomolecules. *Science*, 246(4926):64–71, 1989.

[40] J Fernández De La Mora and Ignacio González Loscertales. The current emitted by highly conducting taylor cones. *Journal of Fluid Mechanics*, 260:155–184, 1994.

[41] Michel Cloupeau and Bernard Prunet-Foch. Electrohydrodynamic spraying functioning modes: a critical review. *Journal of Aerosol Science*, 25(6):1021–1036, 1994.

[42] Ignacio Romero-Sanz, Rodrigo Bocanegra, J Fernandez De La Mora, and Manuel Gamero-Castaño. Source of heavy molecular ions based on taylor cones of ionic liquids operating in the pure ion evaporation regime. *Journal of Applied Physics*, 94(5):3599–3605, 2003.

[43] John Ziemer, Thomas Randolph, Garth Franklin, Vlad Hruby, Douglas Spence, Nathaniel Demmons, Thomas Roy, Eric Ehrbar, Jurg Zwahlen, Roy Martin, et al. Delivery of colloid micro-newton thrusters for the space technology 7 mission. In *44th AIAA/ASME/SAE/ASEE Joint Propulsion Conference & Exhibit*, page 4826, 2008.

[44] Chase Spenser Coffman. *Electrically-assisted evaporation of charged fluids: Fundamental modeling and studies on ionic liquids*. PhD thesis, Massachusetts Institute of Technology, 2016.

[45] W Balachandran, P Miao, and P Xiao. Electrospray of fine droplets of ceramic suspensions for thin-film preparation. *Journal of Electrostatics*, 50(4):249–263, 2001.

[46] Quynh P Pham, Upma Sharma, and Antonios G Mikos. Electrospinning of polymeric nanofibers for tissue engineering applications: a review. *Tissue engineering*, 12(5):1197–1211, 2006.

[47] A Jaworek, W Balachandran, M Lackowski, J Kulon, and A Krupa. Multi-nozzle electrospray system for gas cleaning processes. *Journal of Electrostatics*, 64(3-4):194–202, 2006.

[48] Paulo C Lozano, Manuel Martínez-Sánchez, and Vlad Hruby. Electrospray propulsion. *Encyclopedia of Aerospace Engineering*, 2010.

[49] Alfonso M Ganán-Calvo, José M López-Herrera, Miguel A Herrada, Antonio Ramos, and José M Montanero. Review on the physics of electrospray: From electrokinetics to the operating conditions of single and coaxial taylor cone-jets, and ac electrospray. *Journal of Aerosol Science*, 125:32–56, 2018.

[50] Chengjin Huang, Jianling Li, Mu Li, Ting Si, Cha Xiong, and Wei Fan. Emission performance of ionic liquid electrospray thruster for micropropulsion. *Journal of Propulsion and Power*, 38(2):212–220, 2022.

[51] Ioan Marginean, Ryan T Kelly, Jason S Page, Keqi Tang, and Richard D Smith. Electrospray characteristic curves: In pursuit of improved performance in the nanoflow regime. *Analytical chemistry*, 79(21):8030–8036, 2007.

[52] Daniel G Courtney, Hanqing Q Li, and Paulo Lozano. Emission measurements from planar arrays of porous ionic liquid ion sources. *Journal of Physics D: Applied Physics*, 45(48):485203, 2012.

[53] M Martinez-Sanchez. Mit course 16.522, space propulsion notes, lecture 20: Electrospray propulsion.

[54] Peter L Wright and Richard E Wirz. Multiplexed electrospray emission on a porous wedge. *Physics of Fluids*, 33(1), 2021.

[55] Peter Wright, Anirudh Thuppul, and Richard E. Wirz. Life-limiting emission modes for electrospray thrusters. *AIAA 2018 Joint Propulsion Conference*, 2018.

[56] M Gamero-Castaño and J Fernandez De La Mora. Direct measurement of ion evaporation kinetics from electrified liquid surfaces. *The Journal of Chemical Physics*, 113(2):815–832, 2000.

[57] Michael R Natisin, Henry L Zamora, Zachary A Holley, N Ivan Arnold, Will A McGehee, Michael R Holmes, and Daniel Eckhardt. Efficiency mechanisms in porous-media electrospray thrusters. *Journal of Propulsion and Power*, 37(5):650–659, 2021.

[58] Edmond J Meyer and Lyon B King. Electrospray from an ionic liquid ferrofluid utilizing the rosensweig instability. In *49th AIAA/ASME/SAE/ASEE Joint PropulsionConference*, page 3823, 2013.

[59] Weiguo He, Xiaoming Kang, Bo Yu, Xinyu Liu, Guanrong Hang, and Wansheng Zhao. Effect of electric field on droplets extraction in ultrasonic electric propulsion system. *Acta Astronautica*, 160:36–45, 2019.

[60] Naoki Inoue, Masayoshi Nagao, Katsuhisa Murakami, Sommawan Khumpuang, Shiro Hara, and Yoshinori Takao. Fabrication of a high-density emitter array for electrospray thrusters using field emitter array process. *Japanese Journal of Applied Physics*, 58(SE):SEEG04, 2019.

[61] Renato Krpoun, Katharine Lucy Smith, John PW Stark, and Herbert R Shea. Tailoring the hydraulic impedance of out-of-plane micromachined electrospray sources with integrated electrodes. *Applied Physics Letters*, 94(16), 2009.

[62] Enric Grustan-Gutierrez and Manuel Gamero-Castaño. Microfabricated electrospray thruster array with high hydraulic resistance channels. *Journal of Propulsion and Power*, 33(4):984–991, 2017.

[63] Yu-Hui Chiu, Geraldine Gaeta, Thomas Heine, Rainer Dressler, and Dale Levandier. Analysis of the electrospray plume from the emi-im propellant externally wetted on a tungsten needle. In *42nd AIAA/ASME/SAE/ASEE Joint Propulsion Conference & Exhibit*, page 5010, 2006.

[64] Jonathan MacArthur, Bjarni O Kristinsson, Dakota Freeman, Elaine Petro, Hanqing Li, and Paulo C Lozano. Microfluidic and extractor electrode update in the ion-electrospray propulsion system. In *36th International Electric Propulsion Conference*, 2019.

[65] Frances Ann Hill, Eric Vincent Heubel, Philip Ponce de Leon, and Luis Fernando Velásquez-García. High-throughput ionic liquid ion sources using arrays of microfabricated electrospray emitters with integrated extractor grid and carbon nanotube flow control structures. *Journal of Microelectromechanical Systems*, 23(5):1237–1248, 2014.

[66] Senwen Xue, Li Duan, and Qi Kang. Fabrication of externally wetted emitter for ionic liquid electrospray thruster by low-speed wire cutting combined with electrochemical etching. *AIP Advances*, 11(11), 2021.

[67] Peter Mallalieu and Manish Jugroot. Investigation of droplet mode electrospray emitters for use in multimodal systems for spacecraft. In *AIAA Propulsion and Energy 2021 Forum*, page 3438, 2021.

[68] Natalya Brikner and Paulo C Lozano. The role of upstream distal electrodes in mitigating electrochemical degradation of ionic liquid ion sources. *Applied Physics Letters*, 101(19), 2012.

[69] Steven Mark Arestie. *Porous material and process development for electrospray propulsion applications*. PhD thesis, Massachusetts Institute of Technology, 2014.

[70] Paulo Lozano and Manuel Martínez-Sánchez. Ionic liquid ion sources: suppression of electrochemical reactions using voltage alternation. *Journal of colloid and interface science*, 280(1):149–154, 2004.

[71] Daniel G Courtney, Simon Dandavino, and Herbert Shea. Comparing direct and indirect thrust measurements from passively fed ionic electrospray thrusters. *Journal of Propulsion and Power*, 32(2):392–407, 2016.

[72] MR Natisin, HL Zamora, WA McGehee, NI Arnold, ZA Holley, MR Holmes, and D Eckhardt. Fabrication and characterization of a fully conventionally machined, high-performance porous-media electrospray thruster. *Journal of Micromechanics and Microengineering*, 30(11):115021, 2020.

[73] Jimmy Rojas-Herrera, Iulia Jivanescu, Dakota Freeman, David Krejci, Corey Fucetola, and Paulo Lozano. Porous materials for ion-electrospray spacecraft microengines. *Journal of Nanomechanics and Micromechanics*, 7(3):04017006, 2017.

[74] Peter L Wright, Nolan M Uchizono, Adam L Collins, and Richard E Wirz. Characterization of a porous tungsten electrospray emitter. In *37th International Electric Propulsion Conference*, page 232, 2022.

[75] Chong Chen, Maolin Chen, Wei Fan, and Haohao Zhou. Effects of non-uniform operation of emission sites on characteristics of a porous electrospray thruster. *Acta Astronautica*, 178:192–202, 2021.

[76] David Krejci, Fernando Mier-Hicks, Robert Thomas, Thomas Haag, and Paulo Lozano. Emission characteristics of passively fed electrospray microthrusters with propellant reservoirs. *Journal of Spacecraft and Rockets*, 54(2):447–458, 2017.

[77] Peter Lloyd Wright. *Porous Electrospray Fluid Mechanics*. PhD thesis, University of California, Los Angeles, 2022.

[78] NM Uchizono, PL Wright, AL Collins, and RE Wirz. Emission spectra of glows produced by ionic liquid ion sources. *Applied Physics Letters*, 121(15), 2022.

[79] Fernando Mier Hicks. *Spacecraft charging and attitude control characterization of electrospray thrusters on a magnetically levitated testbed*. PhD thesis, Massachusetts Institute of Technology, 2017.

[80] Christopher T Lyne, Miron F Liu, and Joshua Rovey. A brief review of diagnostics for electrospray propulsion. In *AIAA SCITECH 2023 Forum*, page 0263, 2023.

[81] P Mallalieu and M Jugroot. Development of a time-of-flight diagnostic system for electrospray thrusters. In *37th International Electric Propulsion Conference*, 2022.

[82] Christopher T Lyne, Miron F Liu, and Joshua L Rovey. A low-cost linear time-of-flight mass spectrometer for electrospray propulsion diagnostics. In *International Electric Propulsion Conference 2022*, 2022.

[83] C Miller and P Lozano. Measurement of the fragmentation rates of solvated ions in ion electrospray thrusters. In *52nd AIAA/SAE/ASEE Joint Propulsion Conference*, 2016.

[84] NM Uchizono, AL Collins, C Marrese-Reading, SM Arestie, JK Ziemer, and RE Wirz. The role of secondary species emission in vacuum facility effects for electrospray thrusters. *Journal of Applied Physics*, 130(14), 2021.

[85] Pejman Naderi, Mehrzad Shams, and Hojat Ghassemi. Investigation on the onset voltage and stability island of electrospray in the cone-jet mode using curved counter electrode. *Journal of Electrostatics*, 98:1–10, 2019.

[86] Kai Zhang, Shuangyang Kuang, Xiaochen Suo, Xiaobo Huang, Zixue Li, Dian Wang, Hongyu Jia, Liangcheng Tu, and Peiyi Song. Analysis of beam currents under an oscillating cone-jet mode for developing high-precision electrospray thrusters. *Journal of Applied Physics*, 131(9), 2022.

[87] Chengjin Huang, Jianling Li, Mu Li, Ting Si, Cha Xiong, and Wei Fan. Experimental investigation on current modes of ionic liquid electrospray from a coned porous emitter. *Acta Astronautica*, 183:286–299, 2021.

[88] Daniel G Courtney, Nereo Alvarez, and Nathaniel R Demmons. Electrospray thrusters for small spacecraft control: Pulsed and steady state operation. In *2018 Joint Propulsion Conference*, page 4654, 2018.

[89] JR Harris, KL Jensen, DA Shiffler, and JJ Petillo. Shielding in ungated field emitter arrays. *Applied Physics Letters*, 106(20), 2015.

[90] Chengyu Ma. *Design and characterisation of electrospray thrusters with high emission density*. PhD thesis, University of Southampton, 2020.

[91] Lipeng Su, Zhaopu Yao, Jiankun Zhuo, Hao Liu, Hao Yan, and Shuiqing Li. Multiplexed electrospray emission of green energetic ionic liquids from wedge-shaped porous emitters. *Energy & Fuels*, 2023.

[92] CHEN Chong, CHEN Maolin, and ZHOU Haohao. Characterization of an ionic liquid electrospray thruster with a porous ceramic emitter. *Plasma Science and Technology*, 22(9):094009, 2020.

[93] Daniel G Courtney and Herbert Shea. Influences of porous reservoir laplace pressure on emissions from passively fed ionic liquid electrospray sources. *Applied Physics Letters*, 107(10), 2015.

[94] Peter Wright and Richard E Wirz. Transient flow in porous electrospray emitters. In *Aiaa propulsion and energy 2021 forum*, page 3437, 2021.

[95] Suhail Chamieh, Elaine Petro, and Sadaf Sobhani. Additive manufacturing and characterization of porous ceramic electrospray emitters. In *AIAA SCITECH 2023 Forum*, page 0261, 2023.

[96] Rainer A Dressler, Benjamin St. Peter, Yu-Hui Chiu, and Timothy Fedkiw. Multiple emission sites on porous glass electrospray propulsion emitters using dielectric propellants. *Journal of Propulsion and Power*, 38(5):809–821, 2022.

[97] G Anderson, John Anderson, M Anderson, G Aveni, D Bame, P Barela, K Blackman, A Carmain, Lingzhen Chen, M Cherng, et al. Experimental results from the st7 mission on lisa pathfinder. *Physical Review D*, 98(10):102005, 2018.

[98] Suojiang Zhang, Xingmei Lu, Qing Zhou, Xiaohua Li, Xiangping Zhang, and Shucai Li. *Ionic liquids: physicochemical properties*. Elsevier, 2009.

[99] Fernando Mier-Hicks and Paulo C Lozano. Spacecraft-charging characteristics induced by the operation of electrospray thrusters. *Journal of Propulsion and Power*, 33(2):456–467, 2017.

[100] M Martinez-Sanchez. Mit course 16.522, space propulsion notes, lecture 24: Ion emission and the pure ionic regime.

[101] Paul Nancarrow and Hanin Mohammed. Ionic liquids in space technology–current and future trends. *ChemBioEng Reviews*, 4(2):106–119, 2017.

[102] Joshua L Rovey, Christopher T Lyne, Alex J Mundahl, Nicolas Rasmont, Matthew S Glascock, Mitchell J Wainwright, and Steven P Berg. Review of multimode space propulsion. *Progress in Aerospace Sciences*, 118:100627, 2020.

[103] Brian R Donius and Joshua L Rovey. Ionic liquid dual-mode spacecraft propulsion assessment. *Journal of Spacecraft and Rockets*, 48(1):110–123, 2011.

[104] Steven P Berg and Joshua L Rovey. Assessment of imidazole-based ionic liquids as dual-mode spacecraft propellants. *Journal of Propulsion and Power*, 29(2):339–351, 2013.

[105] Arsad Quraishi, Szymon Dworski, Chengyu Ma, Charles N Ryan, Alessandro Ferreri, Guillaume Vincent, Hugo Larsen, Emmanuelle Rosati Azevedo, Emily Dingle, Alberto Garbayo, et al. Designing and commercialization of porous emitter electrospray thruster for space applications. In *AIAA SCITECH 2023 Forum*, page 0262, 2023.

[106] Robert S Legge Jr and Paulo C Lozano. Electrospray propulsion based on emitters microfabricated in porous metals. *Journal of Propulsion and Power*, 27(2):485–495, 2011.

[107] Daniel George Courtney. *Ionic liquid ion source emitter arrays fabricated on bulk porous substrates for spacecraft propulsion.* PhD thesis, Massachusetts Institute of Technology, 2011.

[108] B Gassend, LF Velásquez-García, AI Akinwande, and M Martínez-Sánchez. Fabrication of a fully integrated electrospray array with applications to space propulsion. In *2008 IEEE 21st International Conference on Micro Electro Mechanical Systems*, pages 976–979. IEEE, 2008.

[109] Paulo Lozano. Densification of ionic liquid electrospray thrusters using silicon-based mems fabrication. In *37th International Electric Propulsion Conference, 2022*, 2022.

[110] Simon Dandavino, Caglar Ataman, CN Ryan, Subha Chakraborty, Daniel Courtney, JPW Stark, and Herbert Shea. Microfabricated electrospray emitter arrays with integrated extractor and accelerator electrodes for the propulsion of small spacecraft. *Journal of Micromechanics and Microengineering*, 24(7):075011, 2014.

[111] Matthew S Alexander, John Stark, Katharine L Smith, Bob Stevens, and Barry Kent. Electrospray performance of microfabricated colloid thruster arrays. *Journal of Propulsion and Power*, 22(3):620–627, 2006.

[112] Bryan Little and Manish Jugroot. Bimodal propulsion system for small spacecraft: Design, fabrication, and performance characterization. *Journal of Spacecraft and Rockets*, 57(4):707–719, 2020.

[113] Chase S Coffman and Paulo C Lozano. On the manufacturing and emission characteristics of dielectric electrospray sources. In *49th AIAA/ASME/SAE/ASEE Joint PropulsionConference*, page 4035, 2013.

[114] Andrea G Hsu, Brian B Brady, Myriam P Easton, Aura C Labatete-Goeppinger, Thomas J Curtiss, David Krejci, and Paulo Lozano. Laboratory testing of a modular 8-thruster scalable ion electrospray propulsion system. In *Proceedings of the 36th International Electric Propulsion Conference, Vienna, Austria, Sept. 15–20*, 2019.

[115] Bjarni Örn Kristinsson. *On the design of electrospray emitters and their microfluidic behavior.* PhD thesis, Massachusetts Institute of Technology, 2019.

[116] Peter Mallalieu and Manish Jugroot. Journal paper submitted, 2023.

[117] I Vasiljevich, N Buldrini, F Plesescu, M Tajmar, M Betto, and J Gonzalez Del Amo. Porous tungsten crown multiemitter testing programme using three different grain sizes and sintering procedures. In *The 32nd International Electric Propulsion Conference*, 2011.

[118] Joamín González-Gutiérrez, Gustavo Beulke Stringari, and Igor Emri. Powder injection molding of metal and ceramic parts. *Some critical issues for injection molding*, pages 65–88, 2012.

[119] Arsad Quraishi, Szymon Dworski, Chengyu Ma, Charles Ryan, Alessandro Ferreri, Guillaume Vincent, Hugo Larsen, Emmanuelle Rosati Azevedo, Emily Dingle, Alberto Garbayo, et al. Development of porous emitter electrospray thruster using advanced manufacturing processes. In *37th International Electric Propulsion Conference*, 2022.

[120] Anthony C Adduci, Joshua L Rovey, Christopher T Lyne, Zachary R Putnam, Michael F Lembeck, Chengyu Ma, Charles N Ryan, and Steven P Berg. Characterization of ionic liquid multimode propellant operating in a porous glass electrospray thruster. *International Electric Propulsion Conference*, 2022.

[121] Collin B Whittaker, Henry A Sodano, and Benjamin A Jorns. A resilient extractor for electrospray arrays. In *37th International Electric Propulsion Conference*, 2022.

[122] Robert J Antypas and Joseph J Wang. Pure ionic electrospray extractor design optimization. In *International electric propulsion conference*, page 372, 2019.

[123] Brandon Lojewski, Weiwei Yang, Hongxu Duan, Chengying Xu, and Weiwei Deng. Design, fabrication, and characterization of linear multiplexed electrospray atomizers micromachined from metal and polymers. *Aerosol Science and Technology*, 47(2):146–152, 2013.

[124] Anirudh Thuppul, Peter L Wright, Adam L Collins, John K Ziemer, and Richard E Wirz. Lifetime considerations for electrospray thrusters. *Aerospace*, 7(8):108, 2020.

[125] Peter Wright, Anirudh Thuppul, and Richard E Wirz. Life-limiting emission modes for electrospray thrusters. In *AIAA 2018 Joint Propulsion Conference*, page 4726, 2018.

[126] Richard E Wirz. Electrospray thruster performance and lifetime investigation for the lisa mission. In *AIAA Propulsion and Energy 2019 Forum*, page 3816, 2019.

[127] Jared M Magnusson, Adam L Collins, and Richard E Wirz. Polyatomic ion-induced electron emission (IIEE) in electrospray thrusters. *Aerospace*, 7(11):153, 2020.

[128] Chengyu Ma and Charles Ryan. Plume characterization of a porous electrospray thruster. In *Proceedings of the 36th International Electric Propulsion Conference, Vienna, Austria, Sept. 15–20*, 2019.

[129] John Ziemer, Colleen Marrese-Reading, Charley Dunn, Andrew Romero-Wolf, Curt Cutler, Shahram Javidnia, Thanh Li, Irena Li, Garth Franklin, Phil Barela, et al. Colloid microthruster flight performance results from space technology 7 disturbance reduction system. In *International Electric Propulsion Conference (IEPC)*, 2017.

[130] Christopher T Lyne, Joshua Rovey, and Steven P Berg. Monopropellant-electrospray multimode thruster testing results: Electrospray mode. In *AIAA Propulsion and Energy 2021 Forum*, page 3439, 2021.

[131] Peter L Wright, Henry Huh, Nolan M Uchizono, Anirudh Thuppul, and Richard E Wirz. A novel variable mode emitter for electrospray thrusters. In *International Electric Propulsion Conference (IEPC)*, 2019.

[132] Chase Spenser Coffman. *Considerations for a multi-modal electrospray propulsion system*. PhD thesis, Massachusetts Institute of Technology, 2012.

[133] Quirin Koch, Tony Schönherr, David Krejci, Nina Mühlich, and Bernhard Seifert. Verification of the thrust vectoring capability of a feep thruster using spatial plasma plume diagnostic measurements. In *37th International Electric Propulsion Conference*, 2022.

[134] Ivan Savytskyy and Manish Jugroot. Development and characterization of a vectored electrospray thruster. *SSC23-WI-06, 37th Annual Small Satellite Conference*, 2023.

[135] COMSOL AB. COMSOL Multiphysics®, v. 6.1, 2023.

[136] Bhanu Prashant Baddipadiga, Scott Strathman, Mehdi Ferdowsi, and Jonathan W Kimball. A high-voltage-gain dc-dc converter for powering a multi-mode monopropellant-electrospray propulsion system in satellites. In *2018 IEEE Applied Power Electronics Conference and Exposition (APEC)*, pages 1561–1565. IEEE, 2018.

[137] J Fernández De La Mora. The effect of charge emission from electrified liquid cones. *Journal of Fluid Mechanics*, 243:561–574, 1992.

[138] Manuel Gamero-Castaño and Marc Galobardes-Esteban. Electrospray propulsion: Modeling of the beams of droplets and ions of highly conducting propellants. *Journal of Applied Physics*, 131(1), 2022.

[139] MA Câmara, JC Campos Rubio, AM Abrão, and JP Davim. State of the art on micromilling of materials, a review. *Journal of Materials Science & Technology*, 28(8):673–685, 2012.

[140] Barnabás Zoltán Balázs, Norbert Geier, Márton Takács, and J Paulo Davim. A review on micro-milling: recent advances and future trends. *The International Journal of Advanced Manufacturing Technology*, 112:655–684, 2021.

[141] Dehong Huo. *Micro-cutting: fundamentals and applications*. John Wiley & Sons, 2013.

[142] Kuan-Ming Li and Shih-Yen Chou. Experimental evaluation of minimum quantity lubrication in near micro-milling. *Journal of materials processing technology*, 210(15):2163–2170, 2010.

[143] Harvey Performance. Climb milling vs. conventional milling - in the loupe. `https://www.harveyperformance.com/in-the-loupe/conventional-vs-climb-milling/`, Published: 2017-05-24, Accessed: 2023-09-07.

[144] K Popov, S Dimov, Duc Truong Pham, and Atanas Ivanov. Micromilling strategies for machining thin features. *Proceedings of the Institution of Mechanical Engineers, Part C: Journal of Mechanical Engineering Science*, 220(11):1677–1684, 2006.

[145] Benbi Zhu, Zhijian Zhang, Wang Zhang, Yu Wu, Jianzhong Zhang, Zada Imran, and Di Zhang. Synthesis and applications of porous glass. *Journal of Shanghai Jiaotong University (Science)*, 24:681–698, 2019.

[146] Technical data - ROBU® Glasfilter. `https://www.robuglas.com/en/service/technical-data.html`, Accessed: 2023-08-23.

[147] Iñigo Llanos, Amaia Agirre, Harkaitz Urreta, Thanongsak Thepsonthi, and Tuğrul Özel. Micromilling high aspect ratio features using tungsten carbide tools. *Proceedings of the Institution of Mechanical Engineers, Part B: Journal of Engineering Manufacture*, 228(11):1350–1358, 2014.

[148] Yuntian Yang, Dawei Guo, Xiaokang Li, Leimin Deng, Bixuan Che, and Mousen Cheng. Development and characterization of a novel porous-media borosilicate glass ion sources for electrospray thruster. *Aerospace*, 8(10):297, 2021.

[149] Manuel Martinez-Sanchez and Paulo Lozano. Lecture 22-23 notes: Cone-jet electrosprays, or colloid thrusters, 2015. `https://ocw.mit.edu/courses/16-522-space-propulsion-spring-2015/resources/mit16_522s15_lecture22-23/`, Accessed: 2023-09-26.

[150] Nina Sarah Mühlich, Bernhard Seifert, and Friedrich Aumayr. Ifm nano thruster performance studied by experiments and numerical simulations. *Journal of Physics D: Applied Physics*, 54(9):095203, 2020.

[151] Saba Shaik, Oliver Jia-Richards, and Paulo C Lozano. Characterization of a single-polarity electrospray propulsion system. *37th International Electric Propulsion Conference*, 2022.

[152] Yuri P Raizer and John E Allen. *Gas discharge physics*, volume 1. Springer, 1991.

[153] David Krejci and Paulo Lozano. Micro-machined ionic liquid electrospray thrusters for cubesat applications. In *Proceedings of the 35th International Electric Propulsion Conference*, pages 1–14. Electric Rocket Propulsion Soc., 2017.

[154] Kurt J Terhune, Lyon B King, Kai He, and John Cumings. Radiation-induced solidification of ionic liquid under extreme electric field. *Nanotechnology*, 27(37):375701, 2016.

[155] Timothy Fedkiw, Zackary D Wood, and Nathaniel R Demmons. Improved computed tomography current mapping of electrospray thrusters. In *AIAA Propulsion and Energy 2021 Forum*, page 3389, 2021.

[156] NM Uchizono, PL Wright, AL Collins, and RE Wirz. Emission spectra of glows produced by ionic liquid ion sources. *Applied Physics Letters*, 121(15), 2022.

[157] Ali Mamedov. Machining of brittle materials: micro milling of glass. *Journal of Mechanical Science and Technology*, 35(9):4143–4148, 2021.

[158] Jonathan V MacArthur. *Material and fabrication developments in the ion-electrospray propulsion system*. PhD thesis, Massachusetts Institute of Technology, 2020.

[159] Chengyu Ma, Vincenzo Messina, Charles Ryan, Joshua L Rovey, Zachary R Putnam, Michael F Lembeck, and Steven P Berg. Emission characterization of porous electrospray thrusters with actively controlled flow rate. *37th International Electric Propulsion Conference*, 2022.

Appendix

A Electrospray Control and Data Acquisition System

To control and collect electrospray current-voltage characteristic data across the wide range of voltages required for a multi-onset voltage emission demonstration, the RAPPEL electrospray control hardware and software suite required an upgraded hardware and software system for control and data acquisition (CDAQ). New high voltage power supplies were acquired and a printed circuit board was designed alongside a complete redevelopment of the LabView control and data acquisition program.

A.1 Electrospray CDAQ Hardware

A new iteration of a custom printed circuit board (PCB) for electrospray control and diagnostics was designed for experiments conducted in this work. The PCB is a redesign of a previous custom control and data acquisition circuit [16]. The schematic, shown in Figure A.1, was simplified, through consolidation of components, control inputs and DAQ outputs. The design process and changes made to the are detailed in this appendix. The PCB layout, shown in Figure A.2, incorporated more robust design and was commercially manufactured. The fully assembled system is shown in Figure A.3. Note the schematic shown is a version ahead of the PCB layout due to component and connection additions and corrections.

Two high voltage power supplies were used to apply high emitter potentials at low currents. The XP Power C40 and C40N are regulated DC-HVDC converters that output 0 to +4 kV and -4 kV respectively. Powered by +12VDC input, the converters are programmed with a linear, LabView controlled 0 to +5V programming voltage and output 0.25 mA at full load. Mounting kits were purchased alongside the converters that provided extra converter protection, monitoring capabilities and prototyping convenience.

The schematic in Figure A.1 is described from left to right. The high voltage supplies were separated from the board in order to allow use of different models if required. At the high voltage inputs to the board, 150 pF filtering capacitors are included to smooth HV input. Using through hole technology and sockets, these capacitors and many other components on the board were designed to be removable for variable value component testing as experiments proceeded. To protect the power supplies, the high voltage connections are connected to earth through the mounting pads, separate from the 5 V return plane.

A pair of HVM OPTO-150 photo detector diode optocouplers were used in tandem with ST 2N2222A NPN transistors to toggle the high voltage lines. The optocouplers are rated for 15 kV reverse voltage, making it safe to apply a continuous high potential at relatively low rise and fall times of 2 μs each. In order to ensure the optocoupler current transfer ratio does not inhibit the already limited electrospray current draw, a high LED forward current of greater than 200

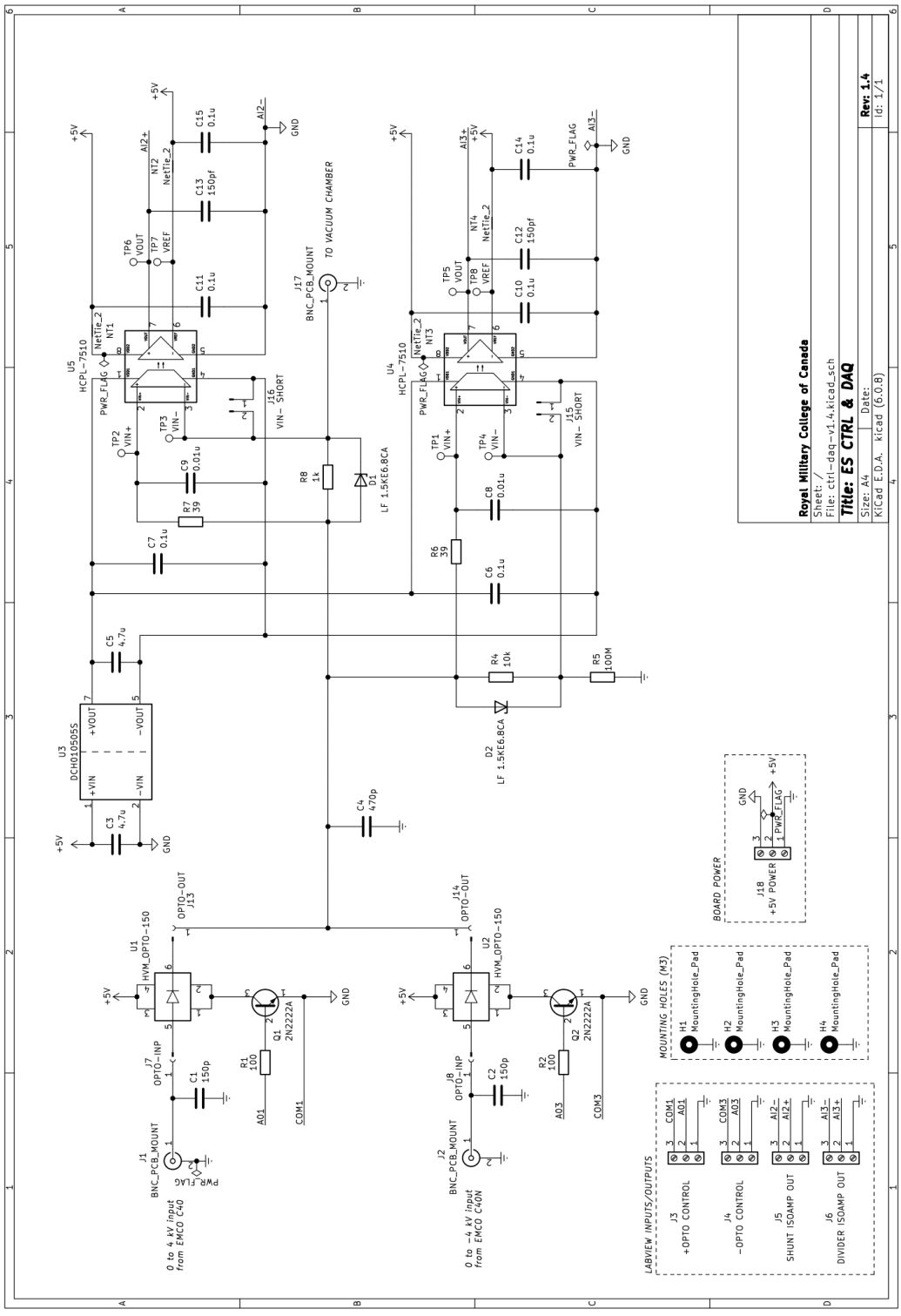

Figure A.1: Electrospray control and DAQ board schematic V1.4. Updated with component and trace corrections/additions.

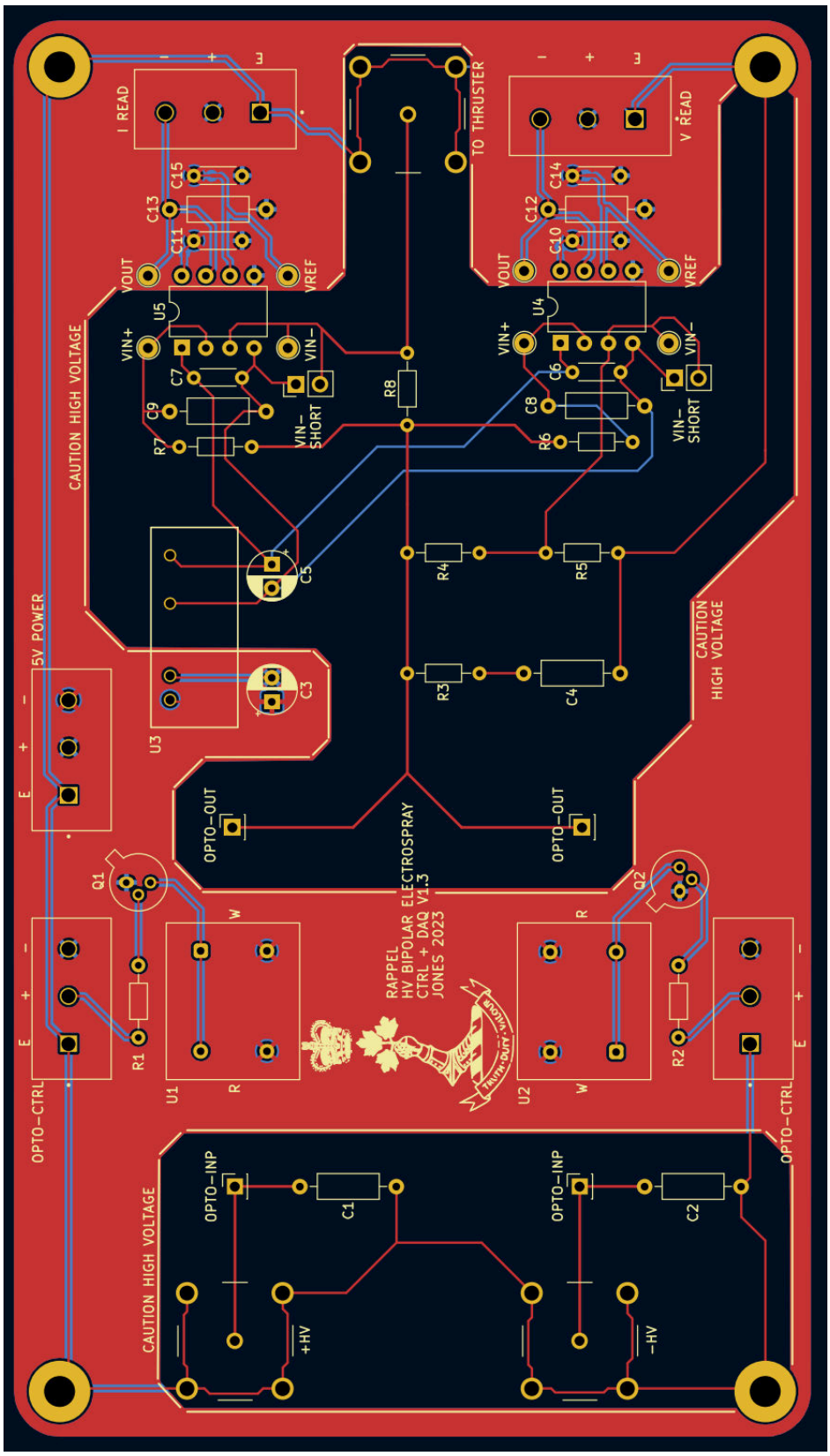

Figure A.2: Front (red) and back (blue) copper masks of control and DAQ PCB V1.3.

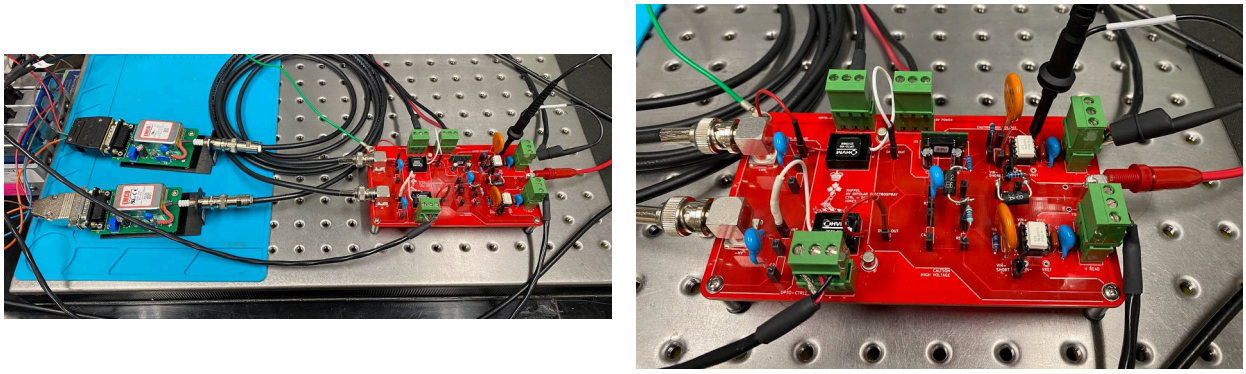

Figure A.3: High voltage supplies connected to control and DAQ PCB V1.3. LabView cDAQ chassis in view off to the left.

mA must be drawn. The LabView control hardware (expanded upon in Appendix A.2) could not provide current outputs of this magnitude and so the optocouplers were powered by a 5 V power supply with 2N2222A transistors in place as high speed switches. A 5 mA base current is applied by a DAQ module, completing the optocoupler connection to ground at sub-100 ns turn on speeds.

High voltage transient suppression was included with 470 pF added capacitance on the HV line with C4. Initially, this sequence also included a 47 ω resistor (R3 in Figure A.2), however, this component was found to arc excessively during testing and was removed.

To obtain emitter diagnostics, a current shunt and voltage divider network are used to read current and voltage just before the signal is sent to the vacuum chamber to be applied to the emitter. In order to protect the DAQ hardware, Avago HCPL-7510 isolation amplifiers protect the LabView DAQ modules from HV transients by transferring the signal across an optical isolation barrier. The shunt and voltage divider were sized according to isoamplifier inputs of +/- 0.2 V for an accurate and linear output voltage of 0 to 5 V to be measured by a DAQ. For the voltage divider design, the 700k input impedance of the isoamplifier was considered. The isoamplifier high side input is powered by a Texas Instruments DCH010505S 3kV isolated DC-DC converter which provides a floating 5 V input to each isoamplifier high side. The low side power input and reference voltage of the isoamplifier is provided by the 5 V PCB plane. Filtering components for the converter and isoamplifiers, including an anti-aliasing filter on each isoamplifier VIN pin were added as per data sheet application specifications. Also specified in the data sheet was an optional short of VIN- pin to ground which was included for PCB testing as a jumper pin. It was found that while the data sheet called for the short to ground, the breadboard testing gave more accurate results when the pin was connected solely to the divider and shunt resistors. Test points were included on each data input and output pin, though the input pins were not used as oscilloscope probes could not read the high voltage lines. The input impedance of a high voltage probe loaded down the input and so the signals were not able to be resolved in this way either.

During initial high voltage testing, the isoamplifiers were often destroyed by high voltage transients that exceeded their input limits. While both the shunt and voltage divider isoamplifier would become unusable, the shunt isoamplifier was destroyed more often than the voltage divider. Two issues are thought to be the cause of transients that destroy the isoamplifiers: inrush current during HV polarity switching due to unwanted capacitance somewhere in the system, and emitter-extractor sparking as discussed in Chapter 5.

The inrush current is thought to be downstream of the PCB control board. The evidence

for inrush current is presented in FigureA.4 as oscilloscope readings from the shunt isoamplifier output. Initially, there was a coax BNC receptacle on the PCB which connected to a coaxial vacuum chamber port. From here the signal was fed through kapton insulated wiring directly to the thruster. When a 2000 V command was toggled on from 0 V, the shunt isoamplifier signal would be observe an initial spike that drops to a baseline voltage as soon as the high voltage had reached its commanded value as observed in Figure A.4a. This capacitance can be estimated with the equation for inrush current:

$$I_{inrush} = C_{load}\frac{dV}{dt} \tag{A.1}$$

A 1 V spike is measured in Figure A.4a. Calculating back from the AVAGO gain, this corresponds to a 100 μA shunt current measurement across a 1000 Ω resistor. Given a voltage increase of 2000 V over 3.2 ms, a capacitance of approximately 160 pF is estimated to be present in the line connecting the CDAQ through the vacuum chamber interface to the thruster.

When the HV output was completely disconnected, there was no inrush current observed when toggling the HV line. When another 3 ft coax cable is added in series to the primary coax cable, the inrush current increases by 50% due to the added capacitance of the coax cable, as observed in Figure A.4b.

The signal increased with commanded HV. Peak signals were observed when the coax cables were connected to the vacuum chamber at 2000 V and commanded voltage was not increased further. Swapping the 470 pF capacitor (C4) for a 2200 pf capacitor decreased the magnitude of the inrush current (Figure A.4c but unfortunately, this also increased the total system fall times to longer than the programmed bipolar switching times, resulting in unintended increased potentials at the beginning of each HV toggle. Removing C4 completely did not seem to reduce inrush current in any measurable way.

The HV output from the PCB was modified first to a coax to banana connector adapter (Figure A.4d) using 5 kV rated wiring, and eventually the BNC receptacle was fully removed as shown on the right-hand side of the board in Figure A.3. While there was a noticeable reduction using the adapter, there was no further change when the BNC receptacle was completely removed. Although the inrush current was reduced, compared to before, there was still a non-negligible amount present in the system, likely due to vacuum chamber connections. Additionally, there was increased instability observed when switching from one polarity to the other as shown in Figure A.4e. All previous tests shown in Figure A.4 occur when toggling +HV on and off again. However, if toggling -HV, off, +HV, or vice-versa, this unstable behaviour is observed, likely due to leftover charge in the system.

A Littelfuse 1.5KE6.8CA zener diode ($V_{breakdown} = 6.45$ V, $V_{clamp} = 10.5$ V) placed in parallel on both the shunt and voltage divider provided enough protection that the isoamplifiers were not destroyed again. However, but the end of testing, these instabilities were not able to be fully resolved. For future work, the sources of high voltage transients should be mitigated as much as possible to ensure a robust circuit that can provide accurate readings of thruster operation. Future work should seek to minimize system capacitance as much as possible to increase the accuracy of shunt current results and increase the robustness of the control board.

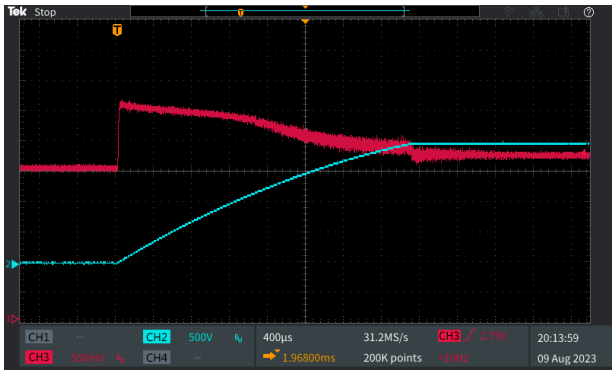

(a) Base inrush current case compared to voltage rise. Single coax connected to chamber. $t_{div} = 0.4$ ms.

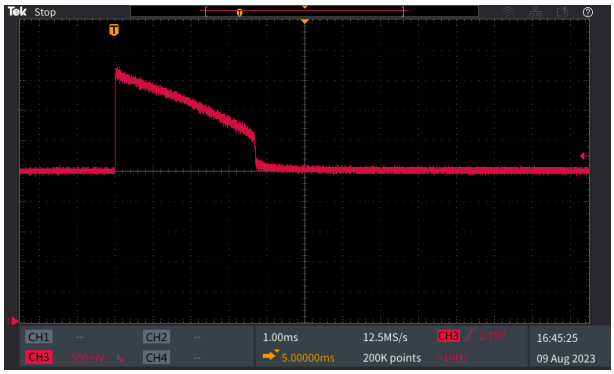

(b) Two coax connected in series to chamber. $t_{div} = 1$ ms.

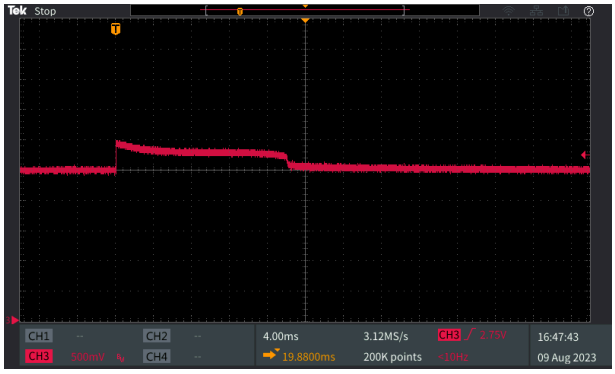

(c) Inrush current decreases, fall time increases with increase in capacitance (2200 pF) on C4. $t_{div} = 4$ ms.

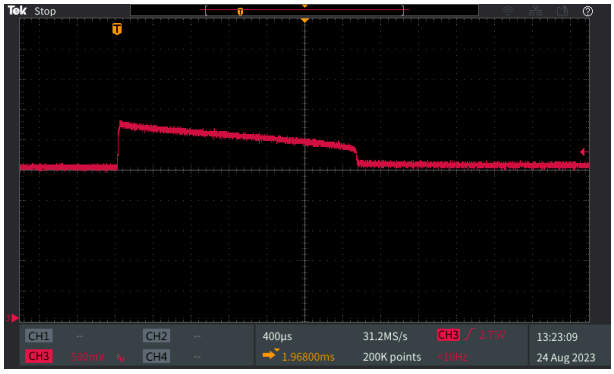

(d) Reduced inrush current with BNC-Banana adapter and insulated wiring instead of full coax connections. $t_{div} = 0.4$ ms.

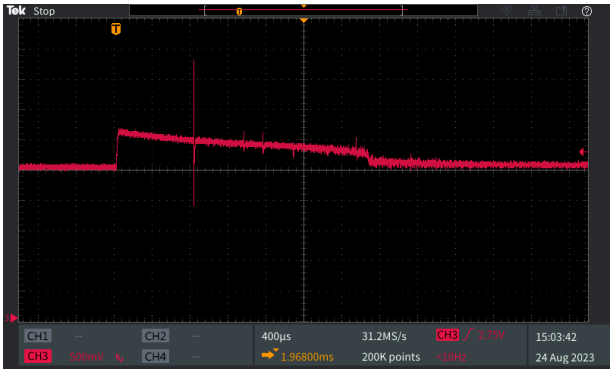

(e) Instabilities present within inrush current when switching from +HV to -HV. 0 to +2000 V command, previous command was 0 to -2000 V. $t_{div} = 0.4$ ms.

Figure A.4: Oscilloscope captures of inrush current occurring under different operating conditions. All commanded HV are 0 to +2000 V. All voltage divisions are 500 mV. Note differing timescale divisions.

A.2 Electospray CDAQ LabView and Python Post-processing

The LabVIEW control and data acquisition program used on the RAPPEL workstation was re-developed in order to provide more robust thruster control and higher resolution data collection through the use of advanced programming structures such as state machines and producer-consumer loops. The software version used in this work is LabVIEW2012. The front panel is shown in Figure A.5 and the block diagram programming is shown in Figure A.6.

Five separate control loops are utilized to provide high voltage control and collect data, running continuously until a stop command is sent from the user. Only the default (program start) states of each case structure are presented for brevity. Each loop is provided virtual tasks corresponding to the physical cDAQ modules (separate from the custom CDAQ pcb) that receive input or output signals depending on the specified tasks. Starting from the top loop shown in Figure A.6, the state machines control/read the EMCO C40 programming voltage, the optocoupler toggle, the internal voltage monitor located on the C40, and finally, all thruster measurements coming from the PCB or the vacuum chamber.

The polarity control state machine first loops through a continuous application of voltage based on user input from the front panel. The HV signal is blocked by the optocouplers, both in an off state, and these can be manually toggled to allow for positive and negative polarity HV application to the thruster. When the square wave enable button is pressed on the front panel, the state machine initiates bipolar operation, looping through a positive HV operation to a transition state (HV relaxation), to a negative HV operation, back to a transition state and the loop repeats until square wave enable is toggled off or the program is terminated. The length of bipolar period and transition stage can be adjusted from the front panel.

A producer-consumer programming structure is used for thruster data collection. This allows for a high rate of sampling to be performed, while computation heavy data transformation is processed downstream. In producer loop, the raw voltage data from the shunt and divider isoamplifiers, and the FEMTO current amplifier are sampled at 20 kHz and streamed to disk in a .tdms file format. In the consumer loop, the same data is processed and displayed to the front panel for

Figure A.5: The LabView front panel allowing thruster control and feedback through decimated data display charts.

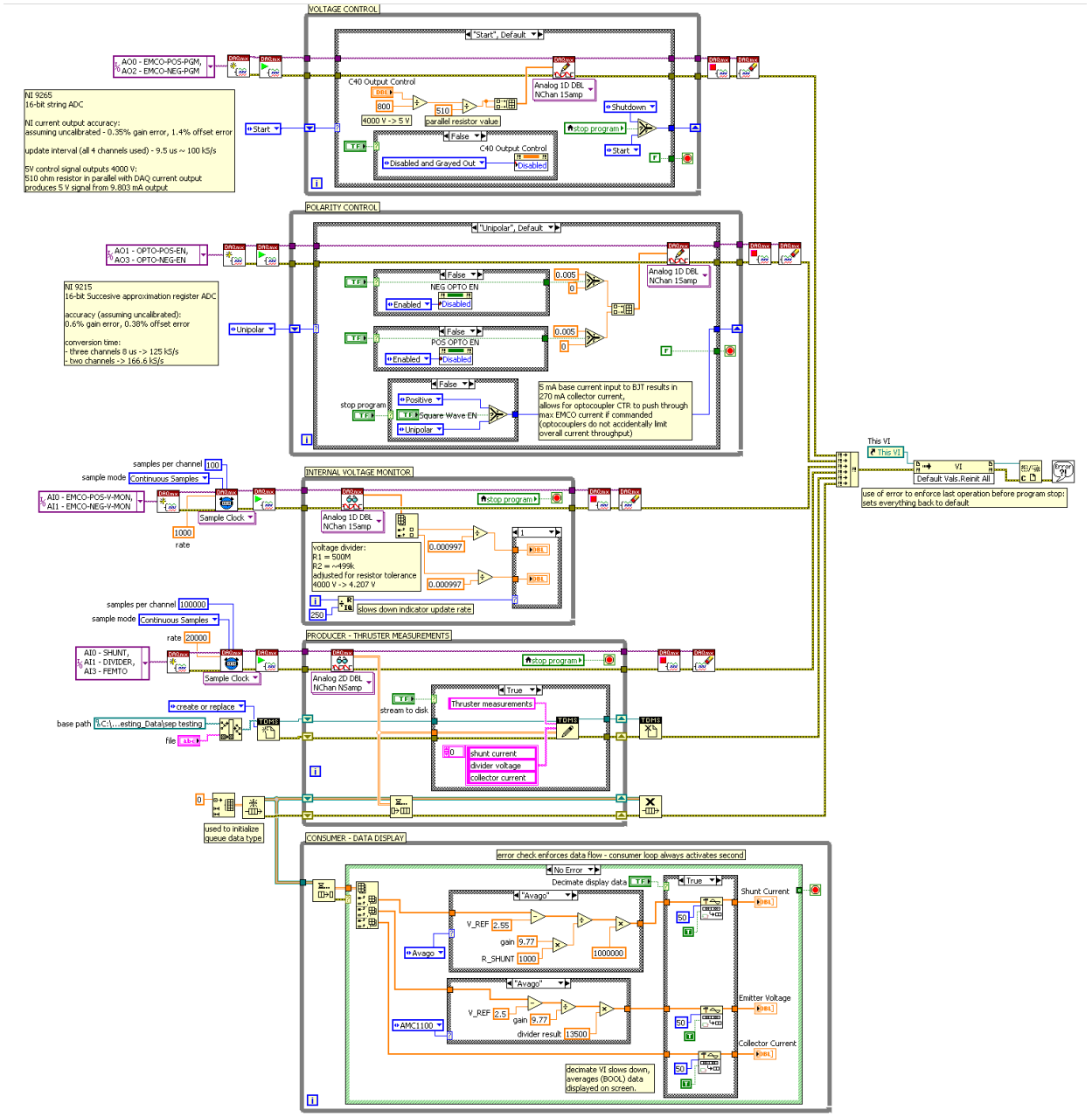

Figure A.6: LabView back panel block diagram programming for electrospray HV control and data acquisition.

live feedback during experiment. Only the raw data is saved to allow for collection at high sample rates. The consumer loop contains case structures to allow the user to change the ouput depending on the model of isoamplifier used or just display the raw data. Before being displayed in chart format, the data is decimated by a factor of 50 and averaged. This acts to smooth and slow down the data to be displayed on the front panel, so the user can parse the thruster behaviour in real time.

All tasks are connected through error clusters to enforce data flow and ensure the program shuts down correctly, setting all controls to default and zeroing command signals to high voltage sources.

Post-processing of testing results was completed using various Python packages. LabView data collection is most efficient when their proprietary technical data management streaming (.tdms) file format is used to log results. The nptdms package, built on numpy, was used to read .tdms data files into numpy arrays. Data manipulation was performed using pandas, and a third-order low pass (cutoff: 50 Hz) butterworth filter was applied to reduce noise using the scipy package.

Royal Military College of Canada, November 2023